Motion in image sequences of living cells

Bergsma, C.B.J.

Publication date
2007
Document Version
Final published version

Motion in Image Sequences of Living Cells

Motion in Image Sequences of Living Cells

ACADEMISCH PROEFSCHRIFT

ter verkrijging van de graad van doctor
aan de Universiteit van Amsterdam
op gezag van de Rector Magnificus
prof. mr. P.F. van der Heijden
ten overstaan van een door het college voor promoties ingestelde
commissie, in het openbaar te verdedigen in de Aula der Universiteit
op woensdag 7 februari 2007, te 10.00 uur

door

CORNELIS BAUKE JAN BERGSMA

geboren te Dordrecht

Promotiecommissie:

Promotor:	prof. dr. ir. A.W.M. Smeulders
Overige leden:	prof. dr. N. Nanninga
	prof. dr. T. Gevers
	dr. E.M.M. Manders
	dr. J.M. Geusebroek

Faculteit der Natuurwetenschappen, Wiskunde en Informatica

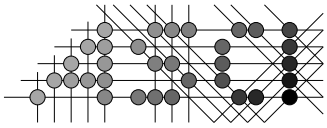

Advanced School for Computing and Imaging

This work was carried out in graduate school ASCI.

cover Afra Dijkstra.

Voor Sigrid, Joris en Niels

Contents

1. Introduction

1.1. Motion in Image Sequences of Living Cells

In this thesis we investigate motion estimation methods in confocal fluorescence microscopy. Imaging living cells at the level of the nucleus or even at a subchromosomal level poses a real challenge because images have a poor signal-to-noise ratio and a low sampling rate combined with objects of interest at the size of the limit of resolution.

In contrast to intrinsic problems the interesting fact of living cells is that they move. They move as a whole, but more interestingly is motion inside a living cell. For our setup cell locomotion is irrelevant. But as cell locomotion will influence the motion estimation results, we have to remove it or compensate it or motion estimation method should incorporate cell locomotion.

The response of motion estimation methods relies on the characteristics of the sequence. As we are operating on the edge of what can be measured, motion information is only useful if one can identify the reliability and the accuracy of a motion estimation method. Therefore, reliability measures are needed to describe how much we are able to trust our estimation results. But what are good reliability measures? Can we predict on what occasions a method will fail?

1.2. Confocal Microscopy

The first compound light microscope is ascribed to Zacharias Jansen in 1595. It took well into the 19th century for further important improvements to the theory and design of microscopes. In the second half of the 20th century confocal microscopy saw its light [29], [151], [113]. The availability of strong light sources such as laser and powerful computing facilities enabled a wide applicability of confocal microscopy. With the introduction of confocal microscopy the images no longer were unknown projections of a complex 3D world. Nowadays confocal fluorescence microscopy is commonly used in the biological and biomedical sciences.

Confocal principle

The principle of confocal microscopy rests on the use of a pinhole to block out sig-

nals which are out of focus. See figure 1 [1] for schematics of the confocal microscope principle. The ability to scan the laser focus in x- and y-direction through the specimen, combined with a scanning table in z-direction, enables the creation of a three dimensional image from the responses primarily originating from the spot of the laser. The logical next step is the evaluation of dynamic processes in a three dimensional environment.

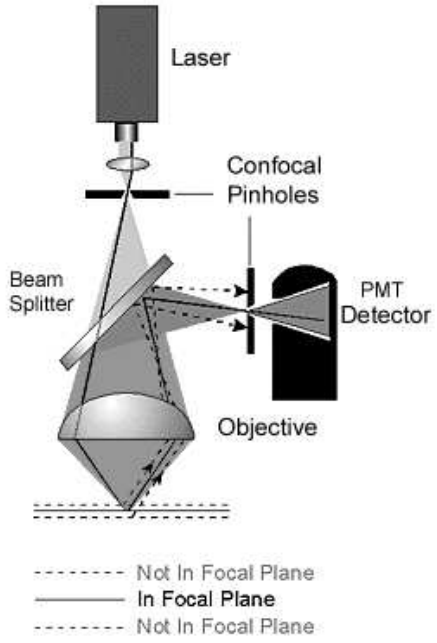

Figure 1.1.: Principle of confocal microscopy. Optical sectioning is provided by the pinholes in front of the laser and the detector element. Hence only the light originating from the focal plane reaches the detector. Light emitted from out of focus planes is largely blocked by the pinhole.

Fluorescence

Fluorescence confocal microscopy relies on the use of fluorophores attached to the biological substrate to be visualized. In the specimen, fluorescent molecules are either natural fluorophores, or fluorophores added by a chemical process referred to as stain-

[1] image obtained from $http://www.hi.helsinki.fi/amu/AMU\%20Cf_tut/cf_tut_part1-4.htm$

ing. The latter process can be done in such a way that the deposition of the fluorophores is specific to certain functional groups in the specimen. [2], [127], [128],

Light production at the focal spot originates from fluorophores. The fluorophores are excitated by the scanning focal spot. When staining and image formation is done right, it may be concluded that the detected light is derived with known specificity from the focal spot. Then the intensity of the fluorescence is sufficiently proportional to the density of the fluorophores.

Bleaching

The density is not the only factor one has to take into account when imaging with fluorescence. An important other characteristic is the bleaching of fluorophores. Fotobleaching is the decline of the numbers of molecules which are able to fluoresce. There is an average number of excitation emission cycles one molecule can endure. The average number of cycles depends on the type of fluorescent molecules. Bleaching in the specimen may be modeled in good approximation by an exponential decay process. The speed of decay is determined by the chemical environment of the fluorescent molecules.

Noise

Any measurement on rare, uncorrelated, discrete events will give rise to hits following Poisson statistics. When measuring N photons, there is a 68% probability that the actual amount of photons lies between $N - \sqrt{N}$ and $N + \sqrt{N}$. The higher the amount of collected photons, the smaller the relative uncertainty will become. The signal-to-noise ratio is proportional to $\sqrt{N}$.

1.3. Living Cells

The introduction of fluorescent proteins has made it possible to look into living cells as they function [157], [141]. The potential applications are abundant. We name just a few: visualizing cancer processes in living animals [78], the evaluation of tumor cell mobility, or even processes inside nuclei of living cells [105], [103], [154], [114], [130].

Keeping cells alive

For visualizing its internal functioning it is essential to keep the cell on the microscope stage alive. The cellular environment should be kept constant, by means of controlling the temperature, humidity and CO_2. Also the sensitivity of a living cell to photodamage forms a real threat. The bleaching fluorophores enhance the damaging effect and appropriate measures have to be taken to counter that effect by keeping the light intensity as low as the signal to noise ratio allows for data collection [157]. Limiting

photodamage is controlled by the light intensity and the duration of the illumination at the expense of high levels of noise in the signal.

Living cells move

Once the cells are successfully kept alive during the scanning the door is opened to study the motion of cells and its internal parts. There are various types of motion and movement in living cells. One is locomotion of a cell or a group of cells [78]. When studying motion inside living cells typically first one has to compensate for the motion of the cell as a whole. We leave locomotion to what it is, although the techniques we develop to investigate motion inside living cells need the locomotion of the cell either to be compensated or removed.

1.4. Motion estimation

In the literature of computer vision several models of motion are identified.

Motion models

Rigid motion If an object shape remains constant during the motion one speaks of a rigid motion. Rigid objects can be tracked by matching the previous appearance if the object on the next frame. This assumes that the correspondence of objects over time is unambiguous. It implies that an object needs to be represented by features which are unique to that object. Example features are object intensity, object shape when fixed, spatial arrangement of objects when stable or even object motility when unique.

This immediately gives rise to the question 'what is a good object feature?' For example, the shape of an object is only a good feature if the shape descriptor is both specific and constant for each individual object. For objects with dimensions at or below the limit of resolution of the microscope, the shape as it appears in the recorded image is dominated by the point spread function of the microscope. Thus in good approximation the shape will be identical for all objects. As a consequence, shape alone cannot be used as a unique identifier of the object to track.

Quasi-rigid motion To permit some object flexibility, we can admit piece-wise rigid bodies where the object can be divided into rigid body parts. These rigid parts are connected by hinges enabling orientation changes of parts. The motion of a human body is usually described by such a model for its motion. The degrees of freedom of each joint determines the possible relative motion of the body parts.

Non-rigid motion An object without any rigidity constraint can freely change its shape. The shape of an object is determined by internal and external forces acting upon it [3].

In confocal microscopy we expect to have objects which motion is determined by a non-rigid motion model. Although object particles are not by definition non-rigid

as well. It depends on the problem statement at hand what kind of motion model is appropriate.

Motion estimation

The choice of a proper model for motion estimation depends on several imaging characteristics. The temporal sampling rate of confocal microscopy sequences influences directly the choice of motion estimation models.

Tracking features Tracking features is a widely used technique to estimate the motion in sequences. The features to track can be points [148], [53], [180] or line segments [52]. In these methods tracking is posed as a 'connect the dots' problem. No additional image knowledge is used.

Region based tracking: Another form of tracking is based on region tracking. In region tracking patches of an image are correlated to patches of a next image in a sequence [129], [86], [81].

Optical flow tracking: A third group of motion estimation methods can be characterized by the use of spatio-temporal derivatives. For example optical flow estimation [79], [185], [100] gives a dense velocity field. This is in contrast to the sparse velocity field of the previous mentioned tracking methods.

1.5. Scope of this thesis

In *chapter 2* we evaluate an optical flow velocity estimation method based on spatial and temporal derivatives. The velocity estimation is applied to study chromatin motion. A reliability measure is incorporated to reduce the uncertainty in the estimation [18].

In *chapter 3* we investigate a tracking method that uses the bleaching of fluorescence as a model of spot intensity. With the method it has been studied if spotmotion is dictated by Brownian motion combined with directed motion. The tracking needs to be capable of tracking spots in noisy sequences and spatially the spots only cover several voxels.

Chapter 4 describes the value of determining divergence and curl from sequences of living cells. The influence of the derivative function to the estimation of divergence and curl has been evaluated.

In *chapter 5* we describe the geometrical arrangement of moving objects or points of interest. It has been studied how the geometrical arrangement described by the divergence and curl of parts of the geometrical arrangement is descriptive for the relative motion of internal markers inside a living cell nucleus. Furthermore it has been studied how different definitions of markers result in motion characterization of shapeless objects and blob patterns.

2. Velocity Estimation of Spots in 3D Confocal Image Sequences of Living Cells

2.1. abstract

The analysis of 3D-motion is becoming of increasing importance in life cell imaging. A simple description of sometimes complex patterns of movement in living cells gives insight in the underlying mechanisms governing these movements.

We evaluate a velocity estimation method based on intensity derivatives in spatial and temporal domain from 3D confocal images of living cells. Cells of the sample contain intense spots throughout the cell nucleus. In simulations we model these spots as Gaussian intensity profiles which are constant in intensity and shape. To quantify the quality of the estimated velocity we introduce a reliability measure.

For constant linear velocity the velocity estimation is unbiased. For accelerated motion paths or when a neighboring spot disturbs the intensity profile the method results are biased. The influence of the point-spread function on the velocity estimation can be compensated for by introducing anisotropic derivative kernels. The insight gained in the simulations is confirmed by the results of the method applied on an image sequence of a living cell with fluorescently labeled chromatin.

With the velocity estimation method a tool for estimating 3D velocity fields is described which is successfully applied to a living cell sequence. With the estimated velocity fields motion patterns can be observed, which are a useful starting point for the analysis of dynamic processes in living cells.

2.2. Introduction

During the last few years new labeling techniques (e.g. GFP techniques and in vitro labeling of DNA with fluorescent nucleotide) and detection techniques (e.g. confocal microscopy, 2-photon excitation) have become available that allow us to observe cellular structures in 3 dimensions in living cells. The large amount of data generated by 4D-imaging (3D + time) contains the information concerning sometimes complex movements of these structures. Therefore determination of 3D motion patterns of spots is of major importance. Velocity estimates of individual spots can provide valuable information in analysis of motion patterns.

Velocity estimation methods can be roughly divided in two groups: feature and model based object tracking methods [148], [194] and image derivative based methods like optical flow [1], [11], [12], [79], [100], [153]. Spot tracking methods rely heavily on accuracy of the segmentation of spots or other uniquely detectable characteristic objects. In general, segmentation methods are sensitive to the high noise levels, which are common in image sequences of living cells. In optical flow methods no segmentation is needed. Consequently motion patterns can be obtained avoiding the disadvantages related to segmentation.

Practical imaging with a confocal system results in blurred images of spots [161]. The blurring is caused by the point-spread function of the system. Especially when the objects are small compared to the point-spread function, the blurring can cause a biased velocity estimation. Usually deconvolution is used to reduce the influence of blurring by the point-spread function. However, deconvolution is noise sensitive [176] and complete reconstruction of the original objects is never accomplished. Therefore we have developed a procedure that allows the compensation for blurring by the point-spread function. This procedure is incorporated in the velocity estimation method without any loss of functionality and computational efficiency of the velocity estimation method.

In this paper we evaluate the applicability of optical flow on 3D image sequences containing moving spots. We show that this method is theoretically unbiased for constant motion of a single spot along a straight trajectory. Furthermore we investigate the velocity estimation for curved trajectories of single spots and linear trajectories with overlapping spots and introduce a reliability measure. A correction procedure was designed to compensate for the influence of the point-spread function. The applicability of the here presented methods are demonstrated in two different image sequences recorded by confocal microscopy: 1) fluorescent beads and 2) fluorescently labeled chromatin in living cells [105].

2.3. Materials and Methods

2.3.1. Optical Flow

The formulation of optical flow is based on the assumption that the total time derivative of the image is zero at all positions through the image sequence. This leads to the optical flow constraint as introduced by Horn and Schunk [79]:

$$\nabla I(\mathbf{x},t) \cdot \mathbf{v}(\mathbf{x},t) + I_t(\mathbf{x},t) = \mathbf{0}, \tag{2.1}$$

with $I(\mathbf{x},t)$ the image intensity function, $\nabla I(\mathbf{x},t) = (\frac{\partial I(\mathbf{x},t)}{\partial x}, \frac{\partial I(\mathbf{x},t)}{\partial y}, \frac{\partial I(\mathbf{x},t)}{\partial z})$ the gradient vector of the image intensity, $I_t(\mathbf{x},t)$ the time derivative of the intensity and position $\mathbf{x}$ is the three dimensional position $\mathbf{x} = (x,y,z)$. Vector $\mathbf{v}(\mathbf{x},t)$ is the optical flow at position and time of computation of derivatives. The optical flow vector corresponds to the three dimensional velocity vector at a certain position in space.

In case the space would be one dimensional, a single optical flow constraint is theoretically sufficient to compute a single velocity vector. The single linear equation (2.1) does not yield sufficient information to resolve the velocity from a sequence of 3D images regarding the three dimensional nature of flow vector $\mathbf{v}(\mathbf{x},t)$; the system is under determined. Several solutions for extra constraints are available: multiple measurements in a single point [12], [185], or an extra global constraint [79], or by using a local motion constraint [100] [153].

Multiple measurements in a single point require multiple independent filters applied to the image. For example application of different orders of derivatives or different orientations of derivative filters is used [185]. The computational load increases with the amount of independent filters and higher order derivatives are more sensitive to noise. Consequently, for the noisy images of living cells first order derivatives are more appropriate.

The global motion constraint assumes small variation in the motion over the total image domain. In a sequence with multiple spots, spots have different individual velocities. Accordingly, estimations using a global motion constraint will be biased in living cell image sequences. Therefore the velocity is calculated using a local motion constraint, following [11], [100], [153]. The assumption in using local constraints is that neighboring voxels within a local region Ω will have the same velocity and should give the same optical flow vector. In computing the flow vector, a number of optical flow constraint equations within a small region around the position of flow estimation are combined. To emphasize information close to the point of estimation a weighting function is used which decays with distance from the central position.

We compute the optical flow following [100] and others ([1], [11], [153]). To find the flow vector we compute a linear least squares estimation of $\mathbf{v}(\mathbf{x},t)$ with a Gaussian

weight function $W(\mathbf{x})$. The weight function is incorporated in a squared error function by a convolution of the squared optical flow constraint with $W(\mathbf{x})$

$$E(\mathbf{v}(\mathbf{x},t)) = W(\mathbf{x}) * [\nabla I(\mathbf{x},t) \cdot \mathbf{v}(\mathbf{x},t) + I_t(\mathbf{x},t)]^2, \tag{2.2}$$

with

$$W(\mathbf{x}) = \frac{1}{\sqrt{2\pi\sigma_w^2}} e^{-(\frac{|\mathbf{x}|^2}{2\sigma_w^2})}. \tag{2.3}$$

Equation (2.2) gives the error function in every position $\mathbf{x}$ in the image sequence. Minimizing the error function (2.2) for $\mathbf{v}$

$$\nabla_{\mathbf{v}} E(\mathbf{v}) = W(\mathbf{x}) * [\nabla I(\mathbf{x},t) \nabla I(\mathbf{x},t)^T \cdot \mathbf{v}(\mathbf{x},t) + \nabla I(\mathbf{x},t) I_t(\mathbf{x},t)] = \mathbf{0}, \tag{2.4}$$

and using the assumption of $\mathbf{v}(\mathbf{x},t)$ constant in $W(\mathbf{x})$ results in an expression for the flow vector $\mathbf{v}(\mathbf{x},t)$:

$$\mathbf{v}(\mathbf{x},t) = -\mathbf{A}(\mathbf{x},t)^{-1} \mathbf{b}(\mathbf{x},t). \tag{2.5}$$

In equation (2.5) matrix $\mathbf{A}(\mathbf{x},t)$ and vector $\mathbf{b}(\mathbf{x},t)$ are defined by:

$$\mathbf{A}(\mathbf{x},t) = W(\mathbf{x}) * [\nabla I(\mathbf{x},t) \nabla I(\mathbf{x},t)^T], \tag{2.6}$$

$$\mathbf{b}(\mathbf{x},t) = W(\mathbf{x}) * [\nabla I(\mathbf{x},t) I_t(\mathbf{x},t)]. \tag{2.7}$$

The derivative images in (2.6) and (2.7) are based on spatiotemporal Gaussian derivatives as also used in [118], [185]:

$$I_i(\mathbf{x},t) = \frac{\partial}{\partial i}(g(\mathbf{x},t;\sigma_s,\sigma_t) * I(\mathbf{x},t)) = g_i(\mathbf{x},t;\sigma_s,\sigma_t) * I(\mathbf{x},t), \tag{2.8}$$

with i the index of differentiation ($i = x, y, z, t$) of arbitrary order. The Gaussian kernel for derivative function (2.8) is then:

$$g(\mathbf{x},t;\sigma_s,\sigma_t) = \frac{1}{(\sqrt{2\pi\sigma_s^2})^3} e^{-(\frac{|\mathbf{x}|^2}{2\sigma_s^2})} \frac{1}{\sqrt{2\pi\sigma_t^2}} e^{-(\frac{t^2}{2\sigma_t^2})}, \tag{2.9}$$

with σ_s spatial width and σ_t temporal width of the Gaussian derivative function. Gaussian derivative functions are utilized to suppress the influence of noise on the derivative estimates. Moreover, Gaussian derivatives provide meaningful derivatives in a discrete image [97].

2.3.2. Single Spot Motion Estimation

Consider an image sequence containing spots moving in a 3D environment. All spot intensity profiles contribute to the image intensity. Here we consider spots to be modeled by a Gaussian intensity profile. For a single moving spot, with width σ, the image sequence intensity function $I(\mathbf{x}, t)$ is:

$$I(\mathbf{x}, t) = \frac{1}{(\sqrt{2\pi\sigma^2})^3} e^{-\frac{|\mathbf{x}-\mathbf{s}(t)|^2}{2\sigma^2}}, \tag{2.10}$$

with the trajectory of the spot described by $\mathbf{s}(t)$.

For a single spot moving along a straight line with constant velocity the estimation will be unbiased. For unbiased results error function (2.2) is equal to zero throughout the image i.e.

$$E(\mathbf{v}) = \mathbf{0}. \tag{2.11}$$

Equation (2.11) is zero if the optical flow constraint (2.1) is met. In a straightforward derivation one can prove that with a Gaussian intensity profile and Gaussian derivatives the latter requirement is fulfilled [17].

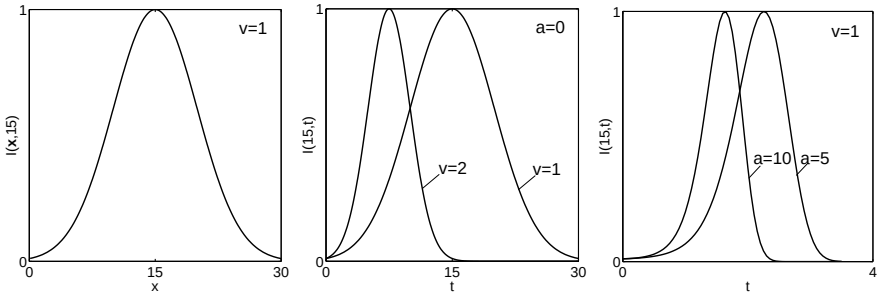

(a) (b) (c)

Figure 2.1.: The intensity profiles in the spatial and the temporal domain for a Gaussian object with $\sigma = 5$. a) A spatial intensity profile ($\mathbf{x} = 15$). b) The temporal intensity profiles of a) for two different velocities $\mathbf{v} = \{1, 2\}$. c) The temporal intensity profiles for two accelerated spots, with acceleration $\mathbf{a} = \{5, 10\}$.

For accelerated motion, the velocity estimation is expected to be biased. To investigate the mechanism which may introduce the bias due to acceleration we look at the temporal intensity profile at a constant position in the image (Fig. 2.1). The position is located on the trajectory of the spot center. When a Gaussian spot is moving along the linear trajectory the intensity in this constant position changes over time. Plotting the observed intensity as a function of time gives a temporal intensity profile as in figure 2.1b. The temporal intensity profile is a symmetric function for a constant velocity along a straight line. The width of the profile is a relation between the width of the spot and the velocity of the spot.

$$\sigma_{temporal} = \frac{\sigma}{|\mathbf{v}|}. \tag{2.12}$$

If we let the Gaussian spot accelerate, the temporal intensity function becomes asymmetric as in figure 2.1c. Since we use symmetric kernels for derivatives and weighting function we expect the asymmetry to be of influence on the bias of the estimation of the spot velocity.

2.3.3. Reliability Measure

The velocity estimation method assumes a constant intensity profile in a local volume Ω. This is true for single spots. When two spots are close to each other the intensity profiles overlap. When intensity profiles overlap the spot intensity profiles are not constant in time anymore. When the intensity of a spot changes over time, bias in the velocity estimation is expected. To detect errors in the velocity field, the smoothness of the local velocity field structure is useful to provide for a reliability measure for the estimated velocity.

The velocity field is called smooth when all vectors in a volume Ω have the same orientation and the same length. This is the case for an unperturbed spot.

A smoothness measure of the velocity field can be calculated by principal components analysis [84] of the relative velocity field in a local volume Ω. A velocity $\mathbf{v_r}(\mathbf{x}, t)$, relative to the average velocity vector $\overline{\mathbf{v}}_\Omega$ in volume Ω is calculated by

$$\mathbf{v_r}(\mathbf{x}, t) = \mathbf{v}(\mathbf{x}, t) - \overline{\mathbf{v}}_\Omega. \tag{2.13}$$

From $\mathbf{v_r}(\mathbf{x}, t)$ we form a scatter matrix

$$S(\mathbf{x}, t) = \overline{\mathbf{v_r}(\mathbf{x}, t)\mathbf{v_r}(\mathbf{x}, t)^T}, \tag{2.14}$$

where the averaging is over all points in Ω. The eigenvalues $\lambda_i(\mathbf{x}, t)$ ($i = 1, 2, 3$) of scatter matrix $S(\mathbf{x}, t)$ represent the smoothness of the velocity field in Ω, since the

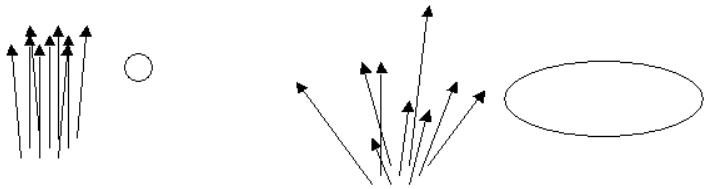

(a) (b)

Figure 2.2.: Two different examples of a 3D velocity field in a local volume Ω. At the left hand side of each figure the velocity field is depicted and at the right hand side the resulting volume spanned by the eigenvectors $\lambda_i(\mathbf{x}, t)$ of the scatter matrix $S(\mathbf{x}, t)$ is schematically given. a) A small deviation from the average velocity vector causes a small volume spanned by the eigenvectors. b) For large deviations of the velocity vectors from the average a large volume is spanned by the eigenvectors.

eigenvalues measure the spread of the vectors $\mathbf{v_r}(\mathbf{x}, t)$ in Ω (see Fig. 2.2). Due to the nature of the relative velocity vector field $\mathbf{v_r}(\mathbf{x}, t)$ a smooth velocity field gives rise to small eigenvalues (see Fig. 2.2a). This is because in a smooth velocity field all velocity vectors have the same length and orientation. With such a field the deviation of the relative velocity from the average velocity in Ω will be zero or at least very small.

Thus a smooth velocity field will yield small eigenvalues λ_i. Therefore we define a reliability measure $R(\mathbf{x}, t)$, which takes the spread of the velocity field in volume Ω relative to the measured average velocity in volume Ω.

$$R(\mathbf{x}, t) = \frac{\overline{\mathbf{v}}(\mathbf{x}, t)}{\overline{\mathbf{v}}(\mathbf{x}, t) + \sqrt{\sum_{i=1}^{3} \lambda_i}}, \tag{2.15}$$

with λ_i the eigenvalues of the scatter matrix $S(\mathbf{x}, t)$ and $\overline{\mathbf{v}}(\mathbf{x}, t)$ the average velocity in a local volume Ω with Ω at location $\mathbf{x}$ and at time point t. The reliability measure is a normalized function, resulting in values between zero and one. A value of one represents a maximal reliability of the velocity estimation. Smaller values of $R(\mathbf{x}, t)$ represent lower reliability.

2.3.4. Anisotropy of the point-spread function

In the previous sections image sequences with isotropic spots and kernels were assumed. However, the actual point-spread function in a confocal microscope is an anisotrope function, which can be approximated by a 3D Gaussian function [178] (in the following denoted by $H(\mathbf{x})$). The size of $H(\mathbf{x})$ in axial direction (σ_H^a) is approximately three times the size in lateral direction (σ_H^l) for a 1.3 NA objective. This anisotropy is expected to cause the estimation to be direction dependent if the size of $H(\mathbf{x})$ is in the order of magnitude of the spots to be observed. Consequently two spots touching in the axial direction experience the same amount of overlap at larger distances, than spots touching in the lateral direction. This influences the determination of the derivatives involved in the velocity estimation. In this section we describe how to overcome this position and orientation dependency of the velocity estimate.

A single spot as imaged by a confocal microscope is the result of a convolution of the original object $f(\mathbf{x},t)$ with the point-spread function $H(\mathbf{x})$,

$$I(\mathbf{x},t) = H(\mathbf{x},t) * f(\mathbf{x},t). \tag{2.16}$$

The Gaussian derivative image of the spot image is a convolution of the spot image $I(\mathbf{x},t)$ with the Gaussian derivative kernel $g_i(\mathbf{x},t)$,

$$I_i(\mathbf{x},t) = \frac{\partial}{\partial i}(g(\mathbf{x},t;\sigma_g^l,\sigma_g^a) * H(\mathbf{x},t;\sigma_H^l,\sigma_H^a)) * f(\mathbf{x},t). \tag{2.17}$$

The convolution of two Gaussian functions, $g(\mathbf{x},t;\sigma_g^l,\sigma_g^a)$ and $H(\mathbf{x},t;\sigma_H^l,\sigma_H^a)$ results in a Gaussian function $G(\mathbf{x},t;\sigma_G^l,\sigma_G^a)$ (see Fig. 2.3), with lateral and axial scales:

$$\sigma_G^l = \sqrt{{\sigma_g^l}^2 + {\sigma_H^l}^2}, \tag{2.18}$$

$$\sigma_G^a = \sqrt{{\sigma_g^a}^2 + {\sigma_H^a}^2}. \tag{2.19}$$

Thus the resulting derivative of the spot is an isotrope function if the Gaussian function $G(\mathbf{x},t;\sigma_G^l,\sigma_G^a)$ is an isotrope function. $G(\mathbf{x},t;\sigma_G^l,\sigma_G^a)$ can be made isotrope if σ_g^l and σ_g^a are chosen as follows:

$$\sigma_G^l = \sigma_G^a = \sigma_G, \tag{2.20}$$

$$\sigma_g^l = \sqrt{{\sigma_G}^2 - {\sigma_H^l}^2}, \tag{2.21}$$

$$\sigma_g^a = \sqrt{{\sigma_G}^2 - {\sigma_H^a}^2}. \tag{2.22}$$

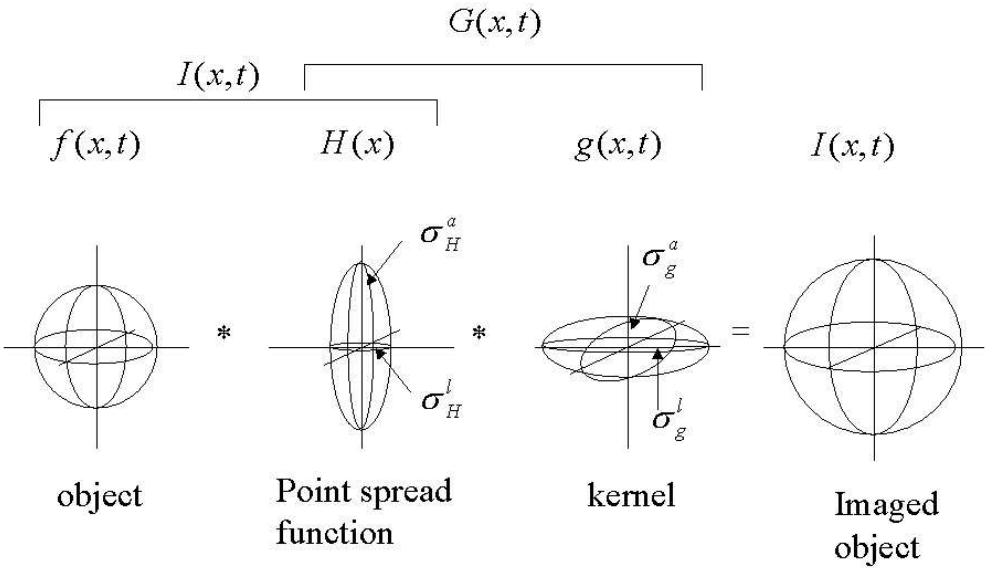

Figure 2.3.: The convolution of an imaged object (left) with the anisotrope cigar shaped point-spread function of the confocal imaging system and an anisotrope oblate ellipsoid kernel of the derivatives leads to an isotrope object image (right). The lateral scale is the scale in x and y direction ($\sigma_{\mathbf{l}} = \sigma_{\mathbf{x}} = \sigma_{\mathbf{y}}$), the axial scale $\sigma_{\mathbf{a}}$ is the scale in the z direction. The scale of the isotrope object image is a function of the original object size and the scales of the point-spread function and the kernels σ_g^l and σ_g^a.

2.3.5. Error Measures

To have an indication of the possible bias of the estimated velocity field, error measures are needed. In the simulations original motion of the spot is known, therefore it is

possible to calculate the difference between the original correct velocity $\mathbf{v}_c$ and the estimated velocity $\mathbf{v}_{est}$. The definitions of the two error measures employed are:

$$\epsilon_v = \frac{|\mathbf{v}_c(\mathbf{x},t)|-|\mathbf{v}_{est}(\mathbf{x},t)|}{|\mathbf{v}_c(\mathbf{x},t)|}, \tag{2.23}$$

$$\epsilon_\theta = \frac{1}{2\pi}\arccos\frac{\mathbf{v}_c(\mathbf{x},t)\cdot\mathbf{v}_{est}(\mathbf{x},t)}{|\mathbf{v}_c(\mathbf{x},t)||\mathbf{v}_{est}(\mathbf{x},t)|}. \tag{2.24}$$

In the experiments ϵ_v is expressed in percentages and ϵ_θ is expressed in degrees.

2.3.6. Sample Preparation

Cell Culture and Preparation

Indian Muntjac cells were cultured in glass-bottom petri-dishes coated with poly-d-lysine (MatTek). Cells were bead-loaded with fluorescein-dUTP (Molecular Probes) as described in [105] and cultured for 5 hours to allow incorporation of fluorescein-12-dUTP into nascent DNA. During imaging the cells were kept at $37°C$ on a heated stage by using an objective heater (Bioptechs, Butler, PA). 3D images were obtained using a Zeiss LSM510 (Carl Zeiss, Jena, Germany) equipped with a Plan-Neofluar 100x/1.3-oil and Ar-ion laser tuned at $488nm$ and less than $500nW$ laser power at the position of the cells, to prevent cell death [105]. 30 3D images each containing 18 optical sections (512x512 pixels) were scanned at a sample frequency of 12 images per hour and a voxel size of $60nm$ lateral and $300nm$ axial. Cells were scanned directly after telophase entering G_1 phase.

Bead Preparation

A fluorescent bead with a diameter of $1\mu m$ is imaged with a Zeiss LSM510 (Carl Zeiss, Jena, Germany) equipped with a Plan-Neofluar 100x/1.3-oil and Ar-ion laser tuned at $488nm$. 15 3D images each containing 64 optical sections (512x512 pixels) were scanned with a voxel size of $20nm$ lateral and $100nm$ axial. Afterwards a linear motion path is constructed by computing images which are translated relative to the original images. For each individual time frame a different image is used. In this way successive frames have uncorrelated noise and imaging imperfections. The bead has a radius R_b in the lateral plane of approximately 25 voxels (see figure 2.4).

2.4. Results

In this section some examples are shown that demonstrate the applicability of the motion estimation on moving spots in 3D. The section consists of a part which shows

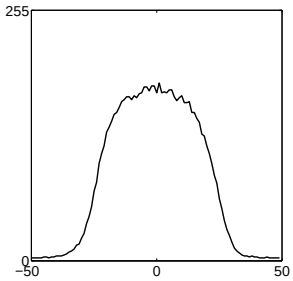

Figure 2.4.: The intensity profile along a line in the xy plane through the center of the recorded bead.

simulations on motion estimation and a part which shows the application of the motion estimation on real 3D image sequences. In the first part a series of simulations is presented, which show the estimation bias in some specific situations such as linear motion, constant and accelerated, and curved motion of a single spot. The estimation bias of close spots with overlapping intensity profiles is examined. A final simulation demonstrates the robustness of the motion estimation method in relation to the constant shape of the intensity profile of the spots.

In the second part the application of the motion estimation is demonstrated on two image sequences recorded with a confocal microscope. The first image sequence is based on a number of 3D images of a fluorescent bead. The second sequence is a time series of 3D images of a living cell recorded during cell division.

2.4.1. Simulations on Motion

In the simulations the average error and the standard deviation of the errors ϵ_v (2.23) and ϵ_θ (2.24) are calculated over a local volume. The local averaging volume is an isotropic volume of the size of the spots. Besides the errors ϵ_v and ϵ_θ also the reliability measure R (2.3.3) is calculated over the same local averaging volume. In this way the reliability measure can be compared to the real estimation bias.

The simulations evaluate the estimation bias of the method in three ways: the influence of the type of motion pattern of the spots, the influence of the point-spread function and the robustness for the shape of the spots.

The different motion patterns under evaluation are linear and curved motion. With linear motion a further classification is made in constant linear motion and accelerated linear motion. In the motion pattern simulations, image sequences are created with the specific motion patterns of a single isotropic Gaussian spot with scale $\sigma = 5$.

Experiments reveal that spatial sampling is not very critical as long as the spatial scale of the derivative kernels (see eq. (2.9)) $\sigma_s \geq 2$ approximately. We choose for σ_s a value of $\sigma_s = 0.4\sigma$ and for spatial scale of local volume $W(\mathbf{x})$ (see eq. (2.2)) a value of $\sigma_w = \sigma$. Since the time sampling is the most critical parameter in the application of the motion estimation the temporal kernel size is varied from $\sigma_t = 2/3$ to $\sigma_t = 2$ in unit time step throughout all simulations.

Linear Motion The estimation bias for the spot moving with constant relative velocity is in the order of $1 \cdot 10^{-3}$ for the temporal filter widths used. The value for the relative velocity $|v|/\sigma$ lies between $|v|/\sigma = 0$ and $|v|/\sigma = 1$. The deviation of the values of R from the perfect situation ($R = 100\%$) are negligible.

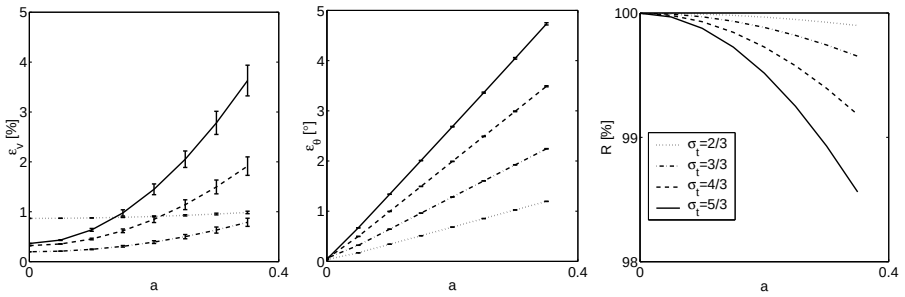

Figure 2.5.: Accelerated linear motion: for a linear moving Gaussian spot the velocity estimation errors ϵ_v and ϵ_θ and the reliability measure R are given as function of the acceleration of the spot.

In figure 2.5 the estimation bias for accelerated motion is shown. As expected, bias is a function of the acceleration a of the spot and of the scale σ_t of the temporal part of the derivative kernels. The acceleration $a \in [0, 0.35]$ which is a realistic choice of parameters considering practical motion situations. The motion is chosen in such a way that the velocity at the time point of motion estimation is the same for all the situations $|\mathbf{v}|/\sigma = 0.5$. The figure shows a relationship between the temporal size of the kernel and the estimation bias. For small kernels the bias is small and the bias increases with increasing kernel size. As can be expected from section 2.3.2 the bias increases with increasing acceleration of the moving spot. The reliability measure R decreases with increasing acceleration and increasing kernel size.

Curved Motion The estimation bias as a function of the radius of a motion curve (r/σ

between $r/\sigma = 0$ and $r/\sigma = 20$) is given in figure 2.6. The tangential velocity of the spot is kept constant during the simulation ($|\mathbf{v}|/\sigma = 0.5$). With decreasing radius of the motion curve the reliability measure R decreases significantly as compared to the linear motion results. Again a larger temporal kernel size gives a larger bias and smaller reliability measure in the motion estimation. For increasing radius, $r \to \infty$, the motion asymptotically reaches a linear motion path. The corresponding bias also asymptotically reach low values for $r \to \infty$.

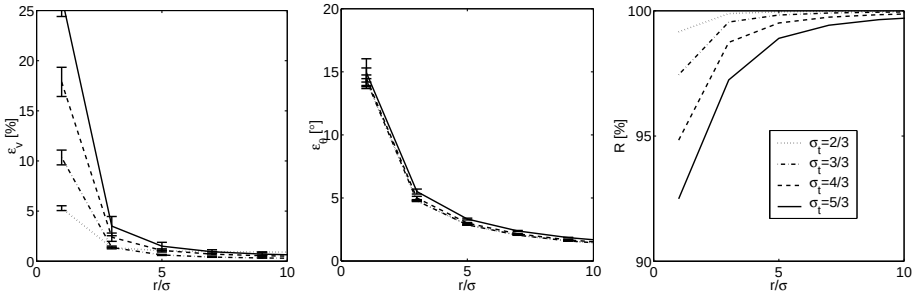

Figure 2.6.: Curved motion with constant velocity: for a moving Gaussian spot along a curved path with radius r the velocity estimation errors ϵ_v and ϵ_θ and the reliability measure R are given as function of the radius r.

Anisotropy Correction The influence of the point-spread function of a microscope is simulated in sequences with anisotropic Gaussian spots. The size in the axial direction differs from the size in the lateral direction ($\sigma^a/\sigma^l = 3$) to simulate the difference in blurring by the microscope in the axial and lateral direction. Due to this blurring of the microscope the intensity profiles of different spots can overlap. The derivative kernel widths are chosen as $\sigma_g^a/\sigma_g^l = 1/\sqrt{57}$ for a $\sigma_G/\sigma^l = 8/\sqrt{7}$ to correct for the anisotropy of the spot. The spot describes a linear motion with constant velocity $|\mathbf{v}| = 0.5\sigma^l$. A second spot is situated at a distance d from the center of the moving spot at the time frame of estimation. Three situations are demonstrated; the second spot is located in the lateral plan ($\phi = 0°$), the second spot is located in the axial plane ($\phi = 90°$) and the second spot is located at $\phi = 30°$ from the lateral plane (see Fig. 2.7). This simulation is repeated with the same anisotropic spots but with isotropic derivative kernels.

The estimation bias for two overlapping Gaussian intensity profiles is given in figure

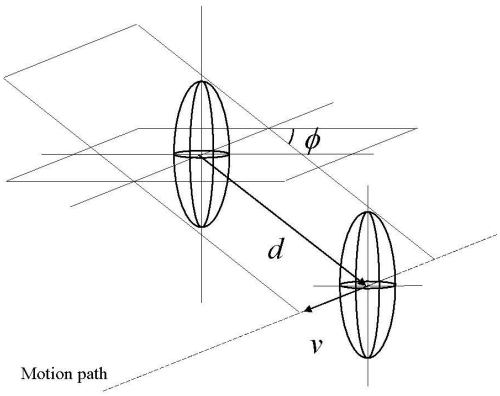

Figure 2.7.: The positioning of two spots for the simulation with two overlapping spots. One spot is fixed in space at the origin. The second spot moves along a straight line with a constant velocity $\mathbf{v}$. The motion path has at a minimum distance d from the origin an angle Φ from the lateral plane.

2.8. The bias is calculated at the time frame where the distance d between the spots is minimal. The estimation bias is a function of d for both situations. The original anisotropic spot with isotropic derivative kernels also shows (Fig. 2.8 top panels) an orientation dependency. In the situation where the anisotropic spot is compensated with anisotropic kernels (Fig. 2.8 bottom panels) the orientation dependency is vanished. The reliability measure R drops below 90% which is small compared to the other simulations described.

Robustness for Intensity Profile Shape Since the estimation method depends on the estimation of intensity derivatives, the shape of a spot is of interest. If the shape of a spot hampers accurate derivative estimation, the result of the estimation method may be biased. Spot shapes encountered in living cells will usually resemble a Gaussian spot shape but also profile shapes that are more accurately described by a parabolic or even a rectangular intensity profile are sometimes present in the images. To examine the bias caused by spot shapes deviating from a Gaussian shape, three spot shapes are used. A Gaussian shaped spot as in the previous simulations, a spot with a parabolic intensity profile and a spot with a rectangular intensity profile. In figure 2.9 the three used intensity profiles are shown. The intensity is given as a function of the distance from the center of the object. In figure 2.10 the estimation bias for the three shapes is given. The bias for the three different shapes is negligible. The reliability measure is

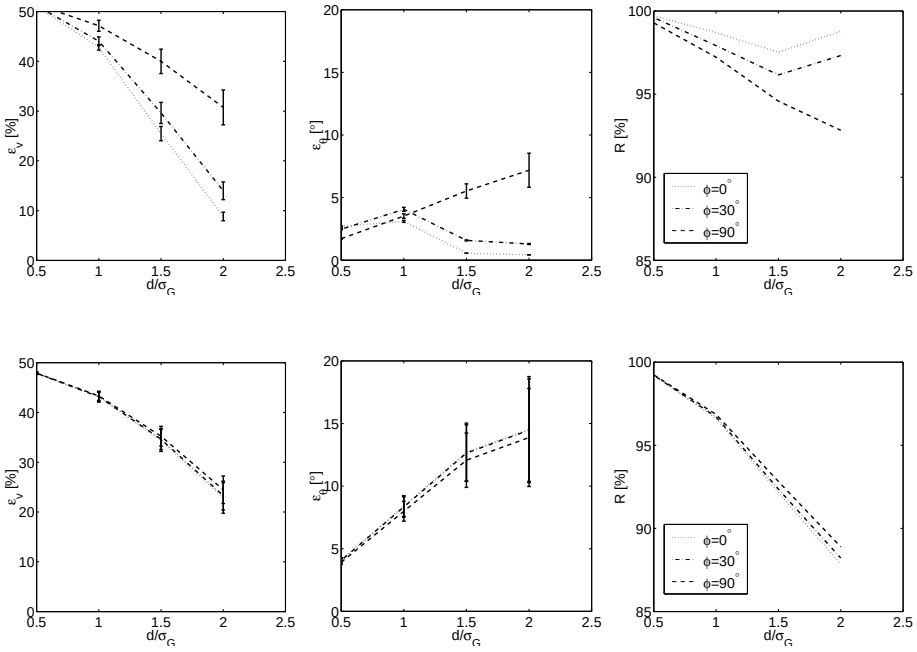

Figure 2.8.: point-spread function influence: an anisotropic spot constantly moving along a straight line with another stationary spot overlapping. The location of the stationary spot at distance d/σ_G is taken for three angles ϕ with the lateral plane. For the top three panels no correction for anisotropy is applied. The bottom three panels show the correction for point-spread function influence.

approximately 100 %.

2.4.2. Application to 3D confocal image sequences

Fluorescent Bead A series of linear motion paths is constructed from the serie of bead images, with velocities $|\mathbf{v}| \in [5, 25]$ in the lateral plane. In figure 2.11 the resulting motion estimation bias is given along with the reliability measure R. The reliability measure R is never lower than 95%.

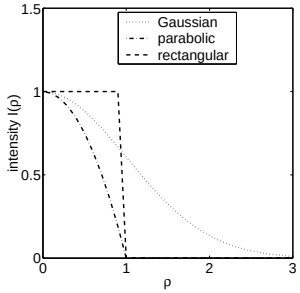

Figure 2.9.: Intensity profiles. A Gaussian shaped intensity profile, a parabolic intensity profile and a rectangular intensity profile. The profiles give the intensity of the objects as function of the radius from the center of the object.

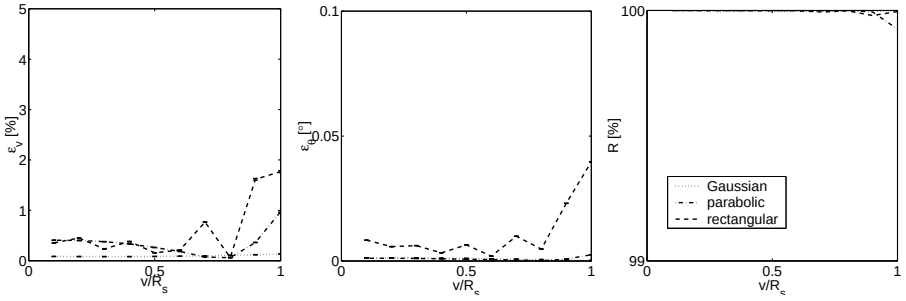

Figure 2.10.: Robustness for shape: the velocity errors ϵ_v and ϵ_θ and the reliability measure R are given for three different shapes, with radius R_s; an object with a Gaussian intensity profile, an object with a parabolic intensity profile and an object with a rectangular intensity profile.

Living Cell The second sequence contains a living cell nucleus labeled with fluorescein-dUTP (Fig. 2.12). Spots formed from labeled DNA move through the nucleus. In the sequence we observe that the cell shows a global motion containing translational and rotational components. Superimposed on this global motion spots show a relative motion. Since we are only interested in the relative motion of the single spots we corrected for nuclear movement. Figure 2.13 (top right panel) shows five time steps of the se-

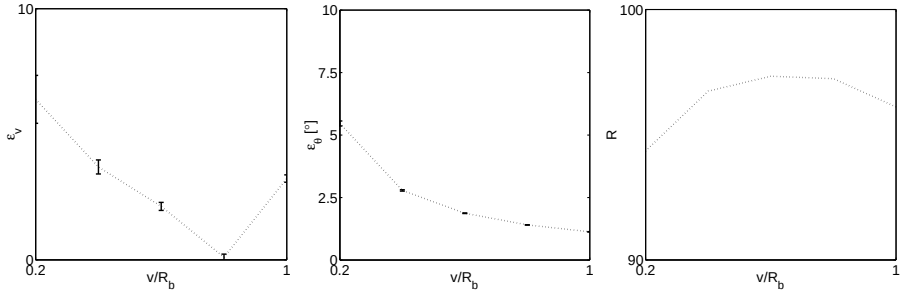

Figure 2.11.: Motion estimation on a single moving fluorescent bead. A bead with radius R_b of approximately 25 [voxel] is artificially moved with a constant velocity $|\mathbf{v}|/R_b$ along a linear trajectory. The velocity estimation errors ϵ_v and ϵ_θ and the reliability measure R are given as function of the bead velocity $|\mathbf{v}|/R_b$.

quence. The time steps are color coded. Each time step is obtained from the sequence by taking a threshold on the maximum intensity projection along the z-axis. This figure gives an impression of the motion paths. The motion paths of spots A and B show an approximately linear path for time steps 2 3 and 4, whereas the motion path of spot C shows a meandering curve.

The velocity of the spots is estimated using kernel sizes $\sigma_s = 5$ and $\sigma_w = 5$ for the spatial scale, and $\sigma_t = 2/3$ for the temporal scale. To represent the estimated velocities the three spots A, B and C from Fig. 2.13 are shown in figure 2.14. For each spot two optical sections are presented. One optical section at a specific z position (x-y plane, left image) and one optical section at a specific x position (z-y plane, right image). In the optical sections two time steps are shown as two colors. The first time step is colored red and the second time step is colored green. To give an idea of the estimated velocities a smooth contour at a constant intensity (isophote) is plotted. The plotted velocity vectors for spots A and B start from the first contour and end near the second contour. The vectors show the direction and the length of the displacement of the spots. The velocity vectors are a projection of the 3D velocity vectors.

Spots A and B (Fig. 2.14 top and middle panels) show a good velocity estimation and spot C (Fig. 2.14 bottom panels) shows an inferior velocity estimation. Both direction and length of the velocity vectors of spot C do not correspond with the displacement of

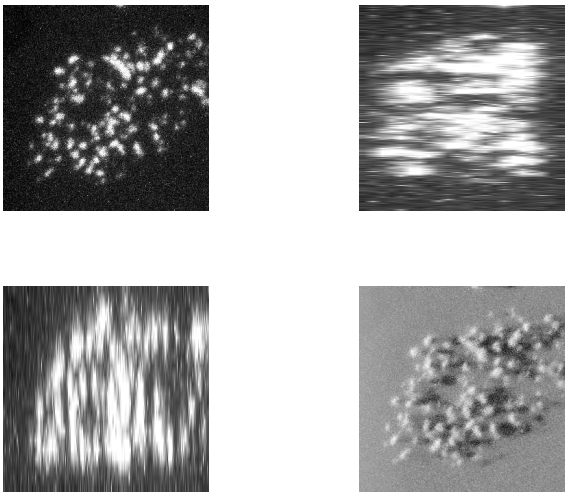

Figure 2.12.: A single frame from the live cell sequence. At the top left, top right and bottom left maximum intensity projections are shown of the recorded volume. The top left image is the xy plane, with the projection along the z-axis, the top right image shows the maximum intensity projection along the x axis and the bottom left image shows the projection along the y axis. The bottom right image shows a 3D impression by means of a Simulated Fluorescence Process (SFP) [175].

the spot due to the meandering of spot C. The values for the reliability measure R for the three spots are measured. Spot A and spot B have a reliability of 99.6 % and 94.0 % respectively. The reliability measure R for spot C is 90.4 %.

2.5. Discussion

In this paper we demonstrated the usefulness of derivative based velocity estimation in 3D confocal image sequences. Within the optical flow framework we investigated the determinants for accuracy in velocity of spots in living cells. The characteristics of the motion patterns turned out to be of major importance for the correctness of the velocity estimation. We have extensively investigated the influence of the motion patterns on the bias of the velocity estimation method in a number of simulations.

The simulations confirm the theoretically derived unbiasness of the velocity estima-

tion for constant linear motion. Therefore constant linear motion is a good starting point for the analysis of other more complex motion patterns. Accelerated motion of spots introduces a bias in the estimated velocities which increases with increasing acceleration and increasing temporal support. Acceleration in the direction of motion introduces a bias due to the shape of the temporal intensity profile. As shown in section 2.3.2 the temporal intensity profile of an accelerated Gaussian spot is asymmetric whereas the temporal derivatives are symmetric functions. This asymmetry of the temporal intensity profile causes a bias in the velocity estimation. For motion with a constant tangential acceleration the motion pattern describes a curve with a specific radius. A curved motion path also deviates from a linear motion path introducing a bias on the velocity estimation. For small values of the radius of the curve and a large width of the temporal support the bias increases significantly compared to linear motion.

The velocity estimation method assumes constant shape of a single spot within the temporal kernel support. When the intensity profile of the spot is severely disturbed by a neighboring spot, large bias occurs in the velocity estimation. Consequently situations where spot intensity profiles are changing rapidly compared to the temporal sampling rate should be avoided.

Apart from the motion pattern of spots the point-spread function introduces a position and orientation dependency of the velocity estimation. For two overlapping spots the influence of the point-spread function was compensated for by introducing anisotrope derivative kernels. In this way the effective spot profiles become isotrope. By compensation the spots take on a larger diameter resulting in a larger bias, however the resulting bias is predictable because the bias is independent of the relative position of two spots. Specifically combined with a possible correction method for the bias, this bias becomes independent of the relative orientation.

To investigate the dependency of the velocity estimation method on the shape of the intensity profile we applied a rectangular, a parabolic and a Gaussian intensity profile. Even in these cases the bias for constant linear spot motion is negligible. Therefore we conclude that the velocity estimation is not significantly dependent on the shape of the intensity profile of the spots as long as the shape is constant in time.

On a real image sequence the motion estimation shows good velocity estimation for spots with a linear motion path as can be expected from theory and simulations. The experiment shows a close correspondence with simulations on linear motion. The bias observed for the fluorescent bead can be attributed to positional and intensity noise. For example spots A and B in the image sequence (Fig. 2.13) of the living cell show an almost linear motion path within the kernel support of the temporal derivative, whereas spot C shows a meandering motion path. Consequently the velocity estimation for spot C shows large errors compared to the velocity estimations for spot A and B. The motion of spot C is highly curved compared to the size of spot C. The order of magnitude in the

bias in both direction and length of the estimated velocity vectors is similar to the bias as found in the simulations (cf. Figs. 2.6 and 2.14 bottom panels). The poor velocity estimation is also reflected in the value of R. In the application R is low for spot C compared to the values of R for spots A and B.

The combination of the temporal kernel size and the temporal sampling is crucial for the velocity estimation. For example the combination in the application is clearly insufficient for spot C, whereas the combination is sufficient for spots A and B. Theoretically, for non linear motion such as for spot C a small temporal kernel is favorable because the influence of changes in the velocity are small for a smaller temporal kernel size. However, a practical lower limit of the temporal kernel size exists due to the discrete nature of time sampling. This limit can be reduced by taking a high as possible temporal sampling rate, the change in velocity is than small for successive frames resulting in a more linear motion path compared to the temporal kernel size.

With the velocity estimation method a tool for estimating 3D velocity fields is presented which is successfully applied to a living cell spot sequence. With the estimated velocity fields motion patterns can be observed.

The bias is dependent on the size of the used kernels, in the simulations of nonlinear motion the bias increases with increasing temporal kernel size. An extension of the work presented could be modeling the existing relation between temporal kernel size and bias for several types of motion (see also [53], [162]). Where the bias in the work of Deriche et.al and Streekstra et.al. is on the position of corners and line structures, the modeling of the bias is analogous in the temporal direction. Modeling the bias as a function of the temporal kernel size enables one to correct for the bias, since the amount of bias that is introduced by the temporal kernel size used can be estimated.

The dependency of the bias on the kernel size is disturbed when spots are overlapping, since the bias becomes direction dependent also. Correcting for this anisotropy eliminates the direction dependency. This again gives the possibility for correcting for the bias, without the influence of the direction of two overlapping spots.

The motion patterns in the velocity field are a starting point for analysis of living cell dynamics during cell division. From the velocity field, motion of the total nucleus is apparent. This nucleus motion is caused by cell migration during image acquisition. Furthermore if several spots form a group with a common motion pattern this is seen in the velocity field. The relative motion of a single spot compared to surrounding spots is also clear from the velocity field. Guided by the estimated velocity field spots can be followed in time creating spot trajectories in a 3D volume. These spot motion patterns and spot trajectories can play a role in analysis of living cell dynamics as is shown in recent work on dynamics in living cells [Manders et. al. manuscript in preparation].

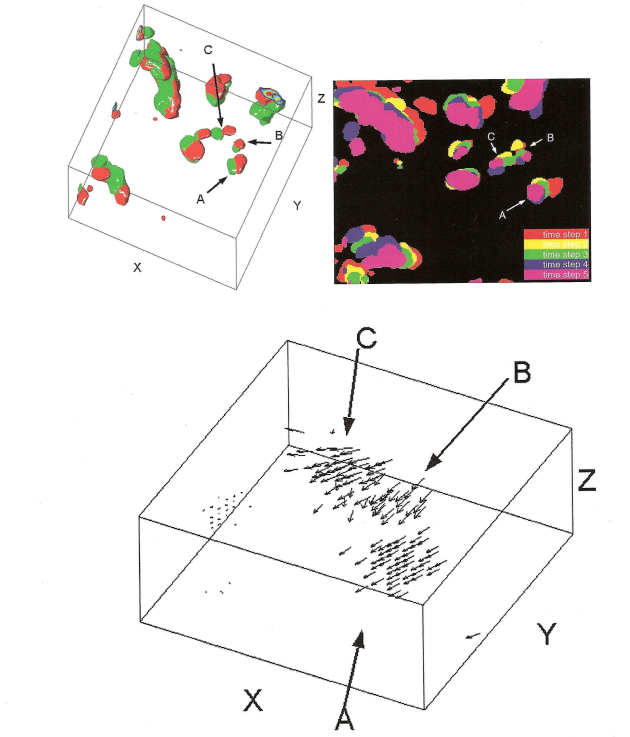

Figure 2.13.: Left panel: two time steps coded red and green respectively in a 3D representation of the living cell, red: first time step, green; second time step. Right panel: A maximum intensity projection of the 3D region. The projection shows a region of the cell at five time steps. Each time step is obtained as a maximum intensity image along the z axis. From this region the velocity vectors are estimated. Bottom panel: A 3D representation of a part of the estimated velocity field around spots A, B and C.

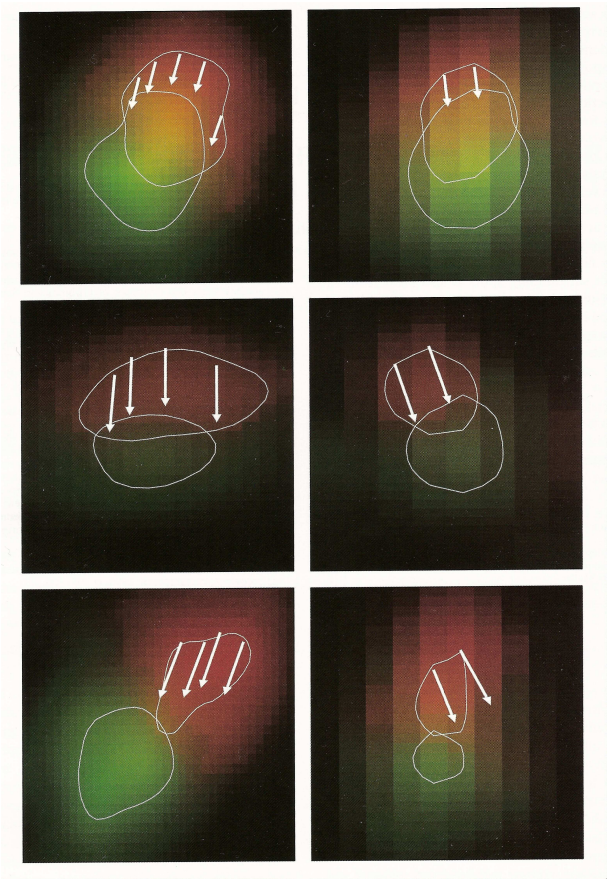

Figure 2.14.: Spot A, B and C at two time steps from top to bottom respectively. Estimated velocity vectors for the spots are projected in th x-y plane and in the z-y plane. The left images show an x-y optical section through the spot with the horizontal axis the x axis and the vertical axis the y axis. The right images show a z-y optical section through the spot with the horizontal axis the z axis and the vertical axis the y axis. The two time steps are color coded, the first time step is colored red the second time step is colored green. For guidance smooth isophote contours are plotted. The velocity vectors originating from isophotes are projected on the optical sections.

3. Spot Tracking in 3D Recordings of Living Cells

3.1. Abstract

Sub-nuclear structures or domains represent morphological or functional entities consisting of DNA, RNA and proteins. These entities can be stained in living cells using fluorescent probes such as green fluorescent protein or fluorescent nucleotides. Analysis of the visual blobs in living cells renders information about the cellular dynamics and the cellular function. In this study, we derive a computational model for tracking of spots in living cells.

We present a spot tracking method for vitally stained cells. The spot tracking method has to deal with Brownian motion and dynamic appearance of the spot intensities due to bleaching of fluorochromes. In addition, the tracking method needs to be capable of handling spot fusions and separations. In fact, both the position and the intensity in the next image are predicted on the basis of past behavior. To this end a intertwined set of linear Kalman filters is used to predict the next instance. The perceived state of the spot is updated by the observations on each new recording by comparing the prediction with the actual measurement.

Object tracking with the proposed method was performed on a 3D time confocal recordings of telomeric DNA. From this recording, several tracks have been reconstructed, including one with spots fusing. Statistical analysis shows that the motion of the spots is a combination of diffusional, Brownian motion and directed motion.

Directional motion is detected in all tracks in spite of the severe Brownian component demonstrating that the method is accurate enough even for vital stain conditions.

3.2. Introduction

In this study we aim at quantifying the 3D structure of cell nuclei from a dynamic perspective. We aim to quantify the three dimensional architecture as a dynamic entity by studying movement and motion of nuclear components in microscopy image sequences.

The architecture has been the topic of research over many years. In almost all studies on three-dimensional motion patterns the extraction of the displacement is done by hand. The research described in [26] focuses on the motion of sub-chromosomal foci. In [105] the chromosome formation is described. The work in [114] addresses protein motion, whereas [130] describes the motion of cajal bodies. This demonstrates a growing interest in the quantitative analysis of cell body dynamics.

In the references, biological systems are all studied in a three-dimensional image sequence. In addition, the target blobs are all bright and small relative to the resolution of the confocal microscope. In this paper we aim at such particles but by automation

of the tracking process we aim to do so more efficiently and more accurately than the results achieved in the above mentioned references by manual tracking. Such a method should be robust against the small movements of Brownian motion in order to detect the underlying directed motion. And, the tracking method should be capable of handling the severe noise conditions which come with imaging living cells.

The targets we want to track are so small that they cover just a few pixels in the scanning grid. Such conditions require that we start building our model from the intrinsic constraints. First, the motion pattern is random but determined by the (thermodynamical) conditions. So once we have set the initial Brownian maximum displacement, we assume such to be constant. Furthermore, in the current method we assume the spot to be approximately constant in size once it has been identified for tracking. In addition we assume the resolution to induce Gaussian-shaped point spread functions and stable noise levels. Thirdly, the bleaching of the fluorescent labels is constant in the sense that it can be modelled as usual by an exponential decay. As a consequence in the tracking method, we cannot assume intensity preservation from one image to another. This puts aside most motion tracking methods in literature starting from an equal intensity constraint. Furthermore we assume the imaging conditions to be sufficiently linear such that in the case of temporal spot-fusion the intensity of the combined spot is predictable from the isolated ones.

The analysis of image sequences for the purpose of estimating camera motion is heavily studied in computer vision. Practical applications are found in 3D scene geometry reconstruction [61], identification of heart wall motion [59], or tracking cars [177] or pedestrians [71]. Each of the aforementioned three methods has its own model for the calculation of the correspondence between points in subsequent frames. This motion correspondence problem is solved by a system of several equations and assumptions or constraints known to be valid for the scene. In the tracking of a car or in the reconstruction of a scene, the common assumption is that the shape is rigid and the intensity varies slowly compared to the time resolution. What remains is an unknown viewing angle and distance to be updated by estimation during the tracking. In the tracking of heart wall motion the rigid body assumption fails, but in that case it is usually assumed that the intensity is proportional to the muscular mass which remains constant. From the constancy a minimum effort solution for the deformation of the heart wall is computed. In the case of pedestrian tracking the constant intensity assumption cannot be made as they may walk into secluded areas. As a consequence, tracking in the reference is done by the prototypical periodical shapes a pedestrian assumes while walking. Here tracking reduces to predicted shape searching. Thus tracking objects requires a few invariant conditions to be estimated in the computational model. Tracking pedestrians in a crowd requires either identification of unique appearance characteristics or accurate prediction of the trajectory and predictable behaviour. For the current

case we may consider either intensity invariance - discarded due to the bleaching -, the shape uniqueness - not applicable as there are many similar shapes or the rigid body assumption - invalid because of the fusion condition. We start building our model from the observation that the intensity decreases predictably, the shape is constant most of the time and the motion behaviour is bounded by the Brownian conditions. None of the existing methods is able to cope with Brownian irregular motion combined with bleaching amidst very similarly appearing objects. We take the commonly used linear Kalman filter as our starting point, see for example [109], but we innovate the method by Kalman tracking the spatial displacement as well as Kalman tracking the intensity of the spot over time.

3.3. Materials and Methods

3.3.1. Preliminaries

In case of Brownian motion, the probability P_d of a specific displacement d is given by the coefficient of diffusion D of the material, and the time t since the start t_0. The direction is a stochastic random variable taken from a uniform distribution:

$$P_d = \frac{1}{2\sqrt{\pi D t}} e^{-d^2/4Dt} \tag{3.1}$$

For stable thermodynamic conditions - that is D is constant - the probability of a given displacement d is a constant as well. This yields a fixed displacement distribution in each direction plus a random direction of displacement. We can only exploit the fact that we know the distribution of the displacement (and not the displacement itself) in contrast to the motion estimation methods cited above.

Spots are detected and characterized by fitting a 3D spot model to the intensity image [120]. In the matching we estimate spot position p, spot intensity I, spatial size σ and local background level b. The spot detection and characterization method behaves well in case of noise. It is capable of detecting and characterizing partially overlapping spots. This method was demonstrated to be useful for the noisy circumstances of vital cell scanning. From the spot detection we copy the estimated intensity and position parameters at subvoxel accuracy in the 3D-grid of the confocal recordings.

In fluorescence microscopy *bleaching* can be modeled by a first order decay as follows:

$$I(t) = I_0 e^{-ct}, \tag{3.2}$$

where c is the decay parameter and I_0 the intensity of a given spot at time t_0. The intensity is monotoneously decreasing. When c is estimated properly and estimating reliably I_0, the spot intensity is sufficiently well characterized over time.

A track is defined as a sequence of measurements assumed to originate from the same object. We propose tracking by combination of spot intensity following and displacement prediction, under the following operational conditions:

1. There is sufficient motion correspondence, that is a spot can be found in the next frame.

2. The mean displacement (see eq. 3.1) is constant over the entire sequence. That is, the thermodynamical conditions are constant.

3. The intensity of a spot decays approximately linear relative to the scale of a time step. This is a weaker assumption than given in eq. 3.2).

4. Measurements are corrupted by *Gaussian white noise*.

Figure 3.1 gives a schematic overview of the spot tracking. We cannot employ the usual smoothness constraint on the shape of the track as the result would be too piece-wise linear to represent a Brownian driven particle. Using the other common constraint in motion estimation, namely selecting a suitable nearest neighbour as the next position on the track would tend to select as the next position of the spot, the spot closest to the current one. From the figure it is clear that such a constraint is not helpful in our case. In the figure (figure 3.1 I, II, and III) the correct spot fulfils probabilistic conditions on displacement and the condition of decaying intensity.

3.3.2. Kalman filter for displacement and intensity

A Kalman filter estimates a process by using feedback control. The filter estimates a process state at time k. It obtains feedback on the validity of its state by performing some input measurements. An intrinsic part of Kalman filtering is that these measurements are noisy. A Kalman filter can thus be divided in two parts: a *time update* and a *measurement update*. The temporal update equations are responsible for projecting the current state and error covariance estimates forward in time obtaining estimates for the next time step. The measurement update equations provide feedback to improve the estimates. Estimation values before *measurement update* are referred to as a priori estimations, while estimations after *measurement update* are called a posteriori estimations. To perform a measurement update, we need measurements of the spot position and spot intensity in the new frame.

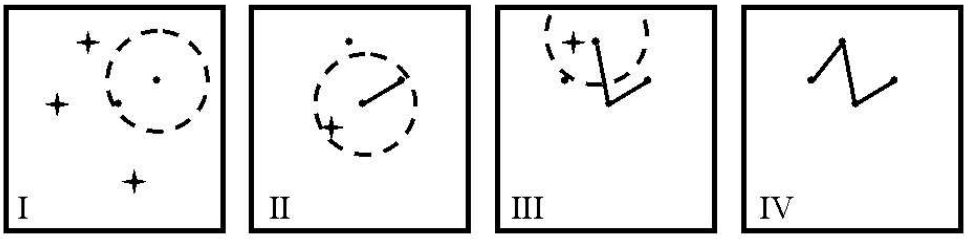

Figure 3.1.: Explanation of the tracking method. Four subsequent frames are shown. The four frames reveal one track of a spot indicated by the disc. Stars indicate other tracks. In frame I only the disc is candidate for continuation of the track because it is the only spot in the prediction window. When the spot measures a correct intensity, the spot is selected to prolong the track. In frame II, two candidates are available in the predicted displacement range. Using a smoothness constraint on the direction of motion would erroneously lead to the selection of the star. However, on the basis of the prediction of the *displacement and intensity* selection will lead to the detection of the disc as the next spot on the track. In frame III again two candidates are given but now the intensity is equal for both spots. From these spots the disc is selected as the star is not within the predicted displacement range. Frame IV shows the complete track of the disc.

We will now discuss each of the modules one by one. In figure 3.2 the proposed Kalman filter pair is drawn schematically.

Since the intensity of the spot and the position of the spot are independent, the parameters can be estimated independently, that is by two separate Kalman filters. From the linearity assumptions on intensity and directed displacement we can use two linear Kalman filters.

Consider the displacement Kalman filter. We use two successive moments in time, $t-1$ and t. The model for the state prediction consists of the displacement $d(t)$ of which the directed component is assumed to be predictable amidst (severe) Brownian motion considered as displacement noise here. The displacement noise may be larger than the actual directed displacement itself, but as long as the operational conditions are valid such would not hamper the method.

$$d(t) = d(t-1) + \epsilon_v(t-1) \tag{3.3}$$

where $\epsilon_v(t)$ is the noise of the displacement state $d(t)$. The noise is assumed to be

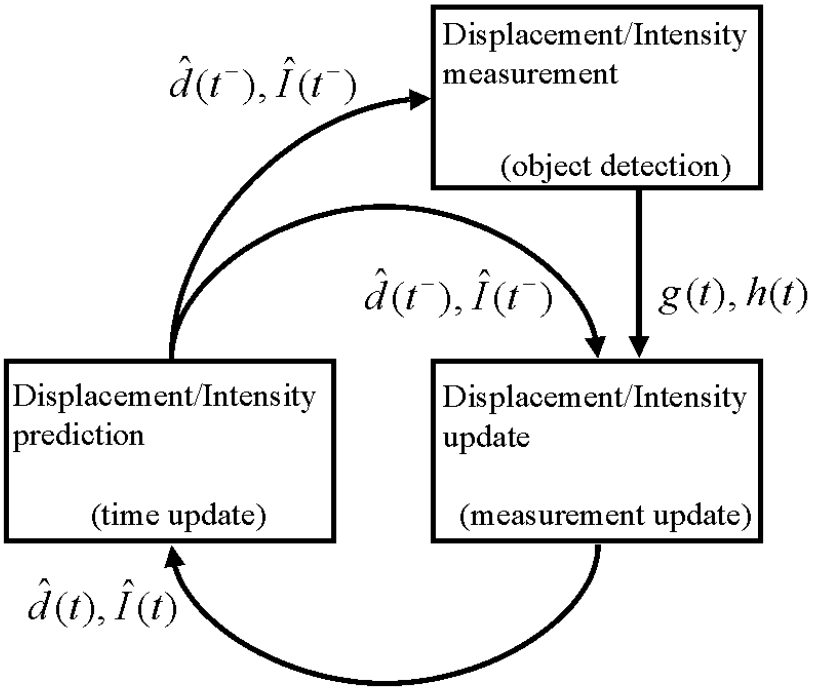

Figure 3.2.: Flow diagram of the proposed Kalman filter pair. Internal state displacement variables are denoted by *d* and intensity state variables are denoted by *I*. Following the prediction $\hat{d}(t)$ for displacement and the prediction $\hat{I}(t)$ for intensity we evaluate a *time update*. The new predictions ($\hat{d}(t^-)$ and $\hat{I}(t^-)$) are used as input for the measurement of the displacement and intensity on the *object detection*. The results of the measurements $g(t)$ for displacement and $h(t)$ for intensity are combined with the predictions to update the state of the model in *measurement update*.

Gaussian with variance σ_v^2.

The measurement $g(t)$ of displacement is given by

$$g(t) = d(t) + \epsilon_m(t) \tag{3.4}$$

with the results of the spot detection and characterization of the selected spot as pa-

rameter for the measurement of displacement. The Gaussian noise in the measurement is given by $\epsilon_m(t)$ with assumed variance σ_m^2.

We use the notation $\hat{d}(t)$ for the estimation of $d(t)$ and $\hat{d}(t^-)$ for the a priori estimation of $d(t)$. The time update equations for the displacement are

$$\hat{d}(t^-) = \hat{d}(t-1), \tag{3.5}$$

with variance

$$\sigma_P^2(t^-) = \sigma_P^2(t-1) + \sigma_v^2, \tag{3.6}$$

The time update gives the a priori estimation of the displacement $\hat{d}(t^-)$. To improve the a priori estimation of the displacement state, the state is updated with the use of the object detection results. The state update is provided by the Kalman gain

$$K(t) = \frac{\sigma_P^2(t)}{\sigma_P^2(t) + \sigma_m^2} \tag{3.7}$$

The actual estimation $\hat{d}(t)$ is related to the a priori estimation $\hat{d}(t^-)$ by:

$$\hat{d}(t) = \hat{d}(t^-) + K(t)(g(t) - \hat{d}(t^-)) \tag{3.8}$$

Note that $g(t) - \hat{d}(t^-)$is the difference between the measurement and the prediction at time t. This difference is added to the a priori estimation $\hat{d}(t^-)$ weighted with the Kalman gain $K(t)$, resulting in the a posteriori estimate $\hat{d}(t)$. The update of the variance estimate is:

$$\sigma_P^2(t) = (1 - K(t))\sigma_P^2(t^-) \tag{3.9}$$

Following this scheme repeatedly, for each new time t the estimation $\hat{d}(t)$ is updated.

Likewise for the intensity signal, a second Kalman filter is used to estimate the intensity as follows

$$I(t) = I(t-1) + \delta + \epsilon_w(t-1) \tag{3.10}$$

where $\epsilon_w(t)$ is the noise of the intensity state $I(t)$. Here δ is the change in intensity in one time step. Again the noise is assumed to be Gaussian white noise with variance σ_w^2.

The measurement $h(t)$ of the intensity is given by

$$h(t) = I(t) + \epsilon_n(t) \tag{3.11}$$

with the intensity of the selected spot as the actual measurement. Again the noise $\epsilon_n(t)$ is assumed to be Gaussian with a variance σ_n^2. We use a similar notation for the

intensity estimations as with the displacement estimations. The estimation of $I(t)$ is given by $\hat{I}(t)$, the a priori estimation is given by $\hat{I}(t^-)$. Then, in the same manner as for the displacement, the time update equations for the intensity state are given by

$$\hat{I}(t^-) = \hat{I}(t-1), \tag{3.12}$$

with variance

$$\sigma_Q^2(t^-) = \sigma_Q^2(t-1) + \sigma_w^2 \tag{3.13}$$

Again a Kalman gain needs to be defined to be able to derive the estimation from $\hat{I}(t^-)$ and the actual measurement. The Kalman gain $L(t)$ is given by

$$L(t) = \frac{\sigma_Q^2(t)}{\sigma_Q^2(t) + \sigma_n^2} \tag{3.14}$$

This results in the intensity estimation $\hat{I}(t)$

$$\hat{I}(t) = \hat{I}(t^-) + L(t)(h(t) - \hat{I}(t^-)) \tag{3.15}$$

Note again the typical relation between the a priori estimation $\hat{I}(t^-)$ and the intensity measurement $h(t)$. Again also the variances in the Kalman filter are updated. For the intensity Kalman filter this update is given by

$$\sigma_Q^2(t) = (1 - L(t))\sigma_Q^2(t^-) \tag{3.16}$$

3.3.3. Spot selection

The spot selection is based on the predicted values of the displacement $\hat{d}(t^-)$ and the intensity $\hat{I}(t^-)$ of the spot. Spots near the predicted displacement are selected (see fig. 3.1). This first selection excludes the nearest neighbour marked by the star and leaves a set of possible track spots. From these remaining spots the spot with closest intensity to the predicted intensity $\hat{I}(t^-)$ is the spot to select. The selected spot determines the new values of displacement measurement $g(t)$ and intensity measurement $h(t)$.

In case no spot fusion and spot splitting occurs, above mentioned method is capable of tracking randomly moving spots. However, spot fusion and splitting introduces abrupt changes in spot parameters. Where the track is continued, either two tracks combine or one track splits into two tracks. We propose a multiple hypothesis solution to track fusing and splitting spots.

If we allow spot splitting and spot fusion, the situation of spot selection changes because three different models are applied:

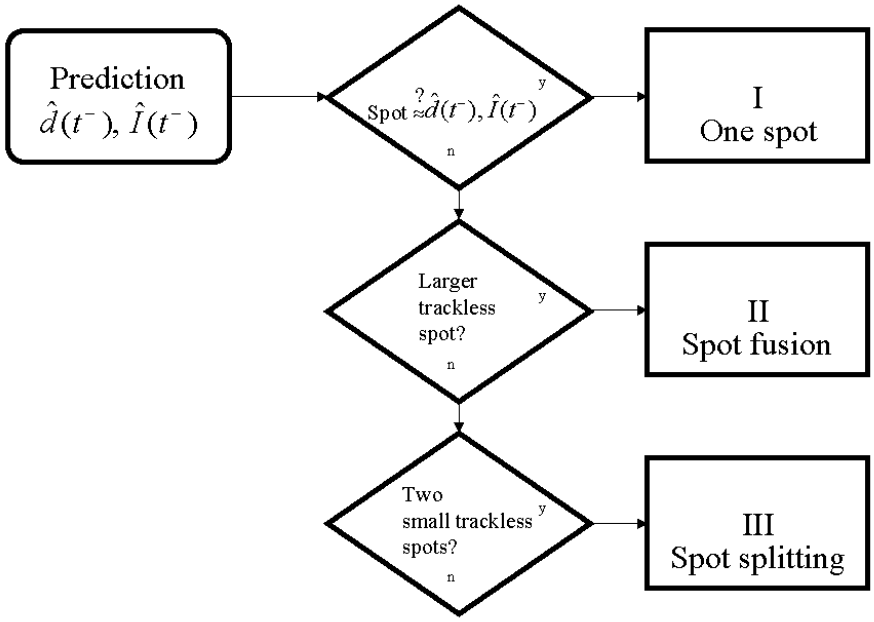

Figure 3.3.: Diagram of the model check method. With the prediction of step size ($\hat{d}(t^-)$) and intensity ($\hat{I}(t^-)$), three possible models have to be checked. The first model, normal correspondence of one spot, is the default model (model I). If model I is not applicable model II is checked. Model II describes the spot fusion by searching for a brighter spot that is not connected to any existing track. If model II is not valid also, model III is checked, by searching for two less bright spots which are not connected to any existing track.

I: Each spot has only one next spot, as described in the previous section.

II: Two single spots fuse into one spot.

III: One single spot splits into two separate spots.

In figure 3.3 the model check is given in a flow diagram. The current prediction of

displacement $\hat{d}(t^-)$ is used to select the best possible hypothesis. The default model is I. The distance between different spots makes sure that II is checked. In case no normal correspondence or a fusion is detected the method checks for possibility of III, spot splitting. Thus detection of spot splitting and spot fusing is needed to steer the spot tracking process.

Fusion detection is a two-step procedure. In the first step a potential fusion event is detected by the relative position between two spots. The second step checks for the two spots in the area where the spots are expected to be in the next frame. The decision of spot fusion is made when 1) no spots with the original parameters are found and 2) a brighter spot exists that does not belong to another track.

For split detection also a two-step approach is used. First all possible spot candidates are examined for best fitting parameters. When no similar spot is found multiple candidates are selected fitting the predicted position. These spots are only selected when 1) the spots are trackless and 2) the sum of intensities is similar to the expected intensity.

Before tracking, the spot tracker has to be initialized. This initialization is done by creating spot associations by hand. For each pair, one spot at the starting frame is associated with a spot in the second frame. This initialization gives starting values for displacement and intensity of the specific spot. Note that we implicitly assume that no splitting or fusing will occur between the first two frames.

3.3.4. Statistical motion description

To examine whether the Brownian motion assumption is correct, we consider statistics of the detected tracks. Statistical trajectory analysis has often been studied in biological processes [51], [136], [38], [144]. Organelle trajectories are examined in [51] by means of the mean-square displacement. We also adopt a mean-square strategy by using $\langle \Delta d^2(\tau) \rangle$.

$$\langle \Delta d^2(\tau) \rangle = \langle [d(t+\tau) - d(t)]^2 \rangle \tag{3.17}$$

The mean-square displacement is given for various conditions [144]. A combination of a pure diffusional movement and directed movement is given by:

$$\langle \Delta d^2(\tau) \rangle = 4D\tau + (v\tau)^2 \tag{3.18}$$

where D is the diffusion coefficient and v the velocity of the active component. A dimensionless parameter Q is derived [82] as the ratio between the mean-square displacement during time τ and the mean-square displacement during time 2τ, the double time interval.

$$Q = \frac{\langle \Delta d^2(2\tau) \rangle}{\langle \Delta d^2(\tau) \rangle} \tag{3.19}$$

From equation 3.19 we can see that, given equation 3.18, for pure diffusional motion $Q = 2$, while for pure linear motion $Q = 4$.

Saxton [144] also describes anomalous diffusion and confined motion.

$$\langle \Delta d^2(\tau) \rangle = 4D\tau^{\alpha} \qquad \text{anomalous diffusion} \qquad (3.20)$$

$$\langle \Delta d^2(\tau) \rangle = C[1 - A_1 exp(-4A_2 D\tau/C)] \qquad \text{confined motion} \qquad (3.21)$$

with $\alpha < 1$ and C the corral size, A_1 and A_2 constants determined by the corral geometry. The three pure modes are given in figure 3.4, active movement, pure diffusional movement and confined movement, each showing a monotonously increasing curve for mean-square displacement.

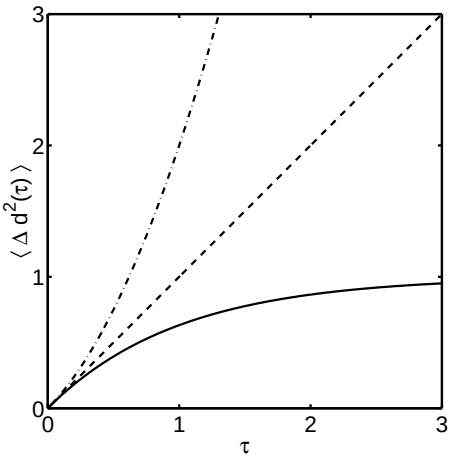

Figure 3.4.: Examples of three modes of movement. The upper line (dash-dot) gives active movement and diffusional movement. The line in the middle (dashed) gives mean-square displacement for pure diffusional motion. Lower line gives the mean-square displacement for confined movement.

3.4. Results

3.4.1. Sample Preparation

For life cell observation, U2OS cells (derived from a human osteosarcoma) were cultured on coverslips in $3.5cm$ petridishes (Mattek, Ashland, Ma.) in RPMI 1640 culture

medium, without phenol red, supplemented with 5% fetal calf serum and buffered with $25mM$ Hepes buffer to pH 7.2 (Life Technologies, Breda, The Netherlands). The Cy3 labelled (C3TA2) PNA probe was kindly provided by DAKO, Glostrup, Denmark. The probe was dissolved to a final concentration of $1mM$ in a buffer containing $80mM$ KCl, $10mM$ K_2PO_4, $4mM$ $NaCl$, (pH 7.2) to a final concentration of $1mM$, and was added to the cells. To label the cells glass bead loading was performed as described by McNeil et al [112] using alkali washed glass beads. The PNA probe hybridize specifically to telomeric DNA repeats in living U2OS cells, resulting in similar fluorescence signals as on fixed chromosomes and nuclei [95], [49]. Images were acquired using a Zeiss CLSM 510, with a Zeiss Plan-Neofluar 100x/ N.A. 1.3 oil objective. Cy3 was excited using the $543nm$ laser line. The image series consists of 70 stacks of 16 Z-slices, size 128x128 pixels taken with 1-minute time intervals. The total sequence thus comprises 70 minutes.

3.4.2. Illustration

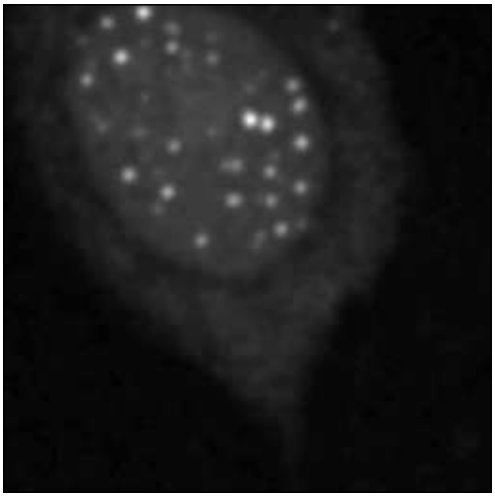

Figure 3.5.: A single frame from the image sequence of a 3D recording of a living U2OS cell. The image shown is a maximum intensity projection of a single 3D frame. The bright spots in the image are fluorescently labelled telomeric DNA repeats. The diffuse staining around the spots represents unhybridized probe present in the cell.

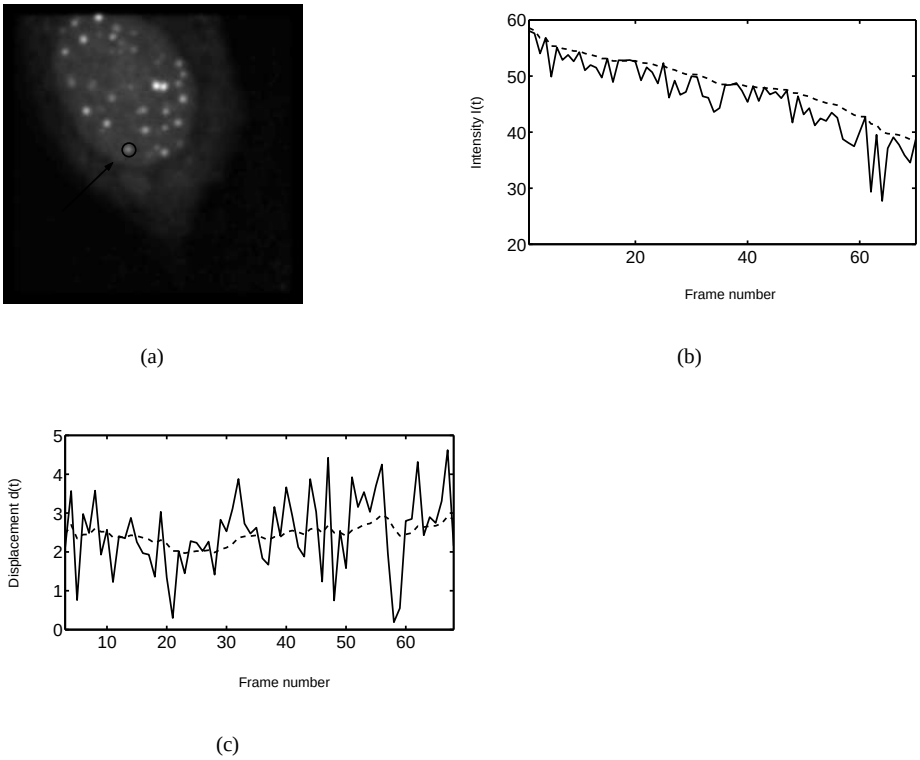

Figure 3.6.: Results for tracking an isolated spot in the image sequence. a) Maximum intensity projection of a frame from the sequence. The circle indicates the selected spot. b) Intensity values of selected spot. The dashed curve is the estimated intensity. The continuous curve is the measured intensity. c) Displacement values of the selected spot.The dashed curve is the estimated displacement. The continuous curve is the measured displacement.

Figures 3.5 and 3.6 show the nucleus and cytoplasm of a living U2OS cell. Here the dots representing the fluorescence signal from the Cy3-labelled PNA probes hybridized to telomeric DNA repeats are clearly seen. Each spot has its own intensity due to differences in repeat number on the different chromosomes. Around the spots a diffuse staining is seen. This diffuse staining is due to unhybridized probe present in the living

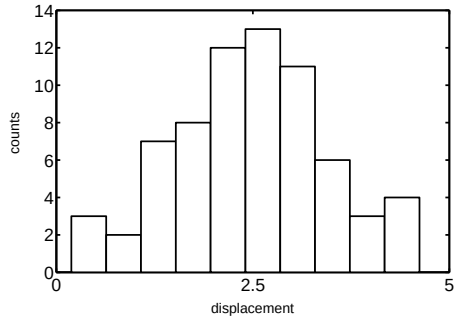

Figure 3.7.: Histogram of spot displacements of the track of the selected spot in figure 3.6 a).

cell.

To verify the bleaching of the spots a single spot is monitored. The intensity development of this spot is given in figure 3.6 b). Note that the intensity decreases with each next frame. This intensity decrease is typical for bleaching of fluorescence in the spot.

The application of the Kalman filter is shown in figure 3.6 b) and c). In figure 3.6 b) the intensity estimation is given by a dashed line. The displacement estimation is given in figure 3.6 c) again by a dashed line. Note that the dashed lines follow the measurements gradually. The individual measurements are only used to update the Kalman states. Therefore the Kalman tracking method is unaffected by the noise in the individual measurements.

Looking closer to the displacement of the spot we note that the average displacement is rather constant during the recording. The average value of approximately $d = 2.5$ can also be appreciated when the displacement is presented in a histogram (figure 3.7). In the displacement histogram a Gaussian distribution can be identified with a mean displacement value of $d = 2.5$ voxels and a standard deviation σ of $\sigma = 1$ voxel for each frame. Reminding the subvoxel accuracy of the spot detection method we can conclude that this spread on the displacement is due to spot motion only.

In total $N = 11$ tracks of single spots are detected. The tracks of these spots are shown in figure 3.8. From these tracks we can see that the motion of the individual spots has a common part and an individual part. The living cell is moving during the recording of the image sequence. Evidently, this common motion component does not influence the quality of the tracking method.

Note also the sharp directional change in the middle part of the tracks. This sharp change is found in all tracks at the same time. Thus, this change in direction is due to a

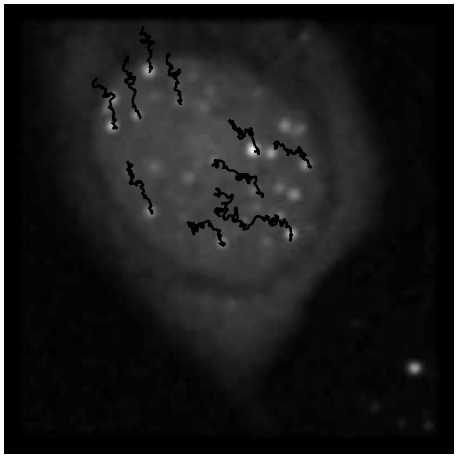

Figure 3.8.: Example tracks of $N = 11$ isolated spots, no spot fusion or spot splitting occurs in these tracks.

global motion. This motion can either be caused by abrupt cell motion or a mechanical impact on the microscope table. In conclusion the spot tracking method is robust to moderate changes in motion properties. However, if displacements due to outside effects are much larger than the expected displacements tracks can be lost. For example if abrupt changes in displacement are much larger than expected displacements, the tracking method cannot find the correct spots and terminates the tracks.

In the presented sequence a few spots fuse. For testing spot fusion, tracks of these spots are selected and visually verified. Figure 3.9 shows an example of two fusion tracks.

In figure 3.10 the mean-square displacement for one track is given. In this figure a quadratic model is fitted to the datapoints according to a least squares fit. This fitted model corresponds to diffusional movement of the spot with an active motion component as is described by equation 3.18. In conclusion we can state that our assumption of Brownian movement of individual spots is a valid assumption. Furthermore the global motion of the cell is small compared to the displacement of spots at each frame. This is seen in the model fitted to the estimated mean-square displacement. For figure 3.10 a Q value of $Q \approx 2.3$ is found at time intervals of $\tau = 5$ frames and $\tau = 10$ frames. Note that for pure diffusional motion a Q value of 2 will be found, while for pure linear motion $Q = 4$ will be found. This indicates that the motion tends to be diffusional combined with a (small) linear displacement component.

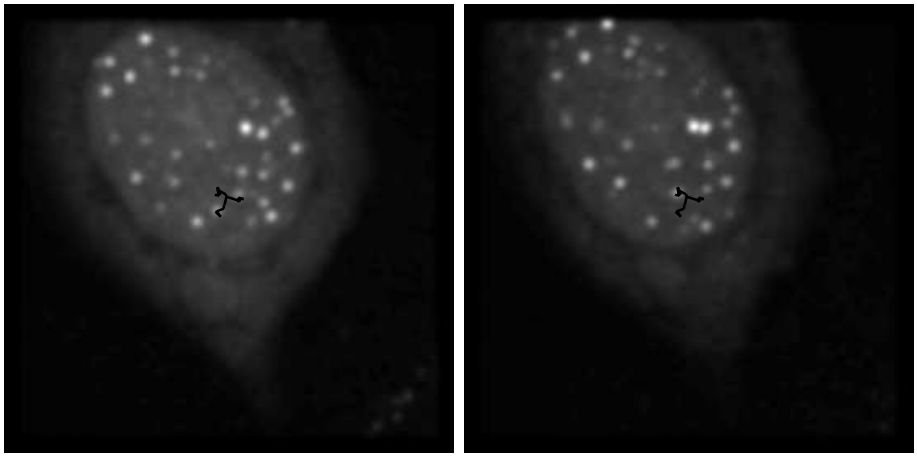

(a) (b)

Figure 3.9.: Example track of fusing spots, a) Start of the spot fusion tracks, b) end of the fused tracks.

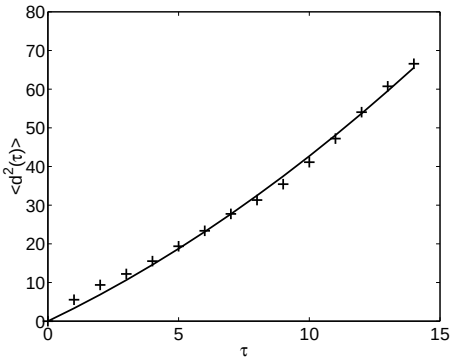

Figure 3.10.: Mean-square displacement as function of duration τ for one estimated track without fusion.

3.5. Discussion

We have derived a tracking method that is robust to noise in image sequences and is capable of tracking spots with Brownian motion, while occasionally fusion or splitting occurs. We have demonstrated the possibility of tracking small spots in a nucleus of a living cell (U2OS cell derived from a human osteosarcoma). The spots in this image sequence are small and the motion is thought to be Brownian. Fusing spots are seen in this sequence.

The measurements of displacement and intensity are corrupted by Gaussian noise. That is, the noise in the measurement is not due to the spot detection method but due to the recording situations for living cells. Under these circumstances the recordings are noisy and have a low temporal sampling. Furthermore the motion is assumed to be Brownian. Thus a stochastical component is present in at least the displacement of the spots. This requires a robust method to track the spots reliably. Kalman filtering gives a robust mechanism to handle the variance in the measurements of displacement and intensity. With Kalman filtering this variance is an explicit parameter that is updated during the creation of the track. At each new frame the Kalman states are updated with the new measurement of the intensity and displacement. Another advantage of this approach is the capability of resolving problems like sudden jumps in position. This is the case when the cell is shifted due to forces from outside the biological system. However very large jumps will eventually result in broken tracks when the displacement is much larger than the expected displacement.

The location and intensity of spots are used as measurements in the tracking method. Therefore we have a spot detection method applied that solely uses the characteristics of spots recorded by a confocal microscope [120]. The method uses a spot model that is fitted to the spots. The results have a subvoxel accuracy. And the method has the ability to detect partially overlapping spots. Therefore, no segmentation or sensitive thresholds are needed in the spot detection method. Since all spots have similar shape and size only the position and intensity identify individual spots.

From the results we can see that the predicted spot is never in conflict with neighboring spots. The fusion detection is capable of selecting possible fusion by means of the distance between two spot predictions. The displacement found in the isolated track demonstrates an average displacement of $d = 2.5$ voxels with a standard deviation σ of 1 voxel. Considering the subvoxel accuracy of the spot detection method, we can conclude that the large variance in the displacement is due to the stochastical component in the displacement itself. Thus the Brownian motion of spots does not hamper the tracking of these spots.

The result of the tracking is found in $N = 11$ tracks of isolated spots. From these tracks several observations can be made. The first observation is that the random dis-

placement component is combined with the directional displacement component. The directional component originates from a motion of the whole cell, while the random component is due to Brownian motion of the spots inside the cell nucleus. The whole image sequence comprises seventy minutes. Thus the time between two frames is one minute. In one minute the cell can drift or the microscope table shows a mechanical drift. Either way, a global motion component does not hamper the tracking method. Another observation is the presence of an abrupt change in the global motion in the second half of the tracks. Since this abrupt change is seen in all the tracks it is likely that the motion is due to an external force. If this force is from outside the cell or even from a sudden motion of the microscope is not clear. It is hard to reconstruct from the tracks what actually happened.

From the statistical analysis applied to the tracks we can conclude that the motion is a diffusional motion of the individual spots. In the experiment a quadratic model is fitted to the data. However, the bias increases with increasing τ because all data points are taken from the same amount of estimated positions. Thus for larger τ the time average is over a smaller amount of data points than in case of small τ. The quadratic model describes diffusional motion combined with directional motion. This is the most probable model considering the global movement of all spots. The dominant movement is still the diffusional movement at small time scale.

4. 2D+t Microscopy Motion Pattern Classification by Expansion and Rotation

4.1. Abstract

Motion patterns like expansion and rotation can provide meaningful descriptions of the processes in living cells and other microscopy image sequences. Expansion and rotation in velocity vector fields can be described by the invariants divergence and curl. Thus estimation of divergence and curl can provide information on interesting motion patterns. This paper describes the local estimation of divergence and curl in image sequences. An indirect approach is used, where from an image sequence the motion field is derived. From this motion field the local divergence and curl are computed. This indirect approach facilitates the computation of the variance of the motion field. This motion field variance is propagated through to the divergence and curl estimation, giving a reliability measure even before the quantities are computed. It is shown in experiments that local divergence and curl can be estimated with a predictable accuracy. Besides stochastic errors also systematic errors like motion field discontinuities due to working conditions which deviate from the model assumptions are examined. Application of local divergence and curl estimation is given using an image sequence of a crawling human T-cell.

4.2. Introduction

In image processing, vector field images are found in numerous applications. These vector field images are derived from single images or from image sequences. In single images the local orientation of the intensity gradient gives a vector field image [68], [138]. In an image sequence the velocity of objects can be estimated from the intensity derivatives resulting in a vector field image representing displacement, the optical flow [79], [93], [118], [11], [14].

Motion patterns like expansion and rotation can provide meaningful descriptions of the processes in living cells and other microscopy image sequences. Expansion and rotation in velocity vector fields can be described by the invariants divergence and curl. Thus estimation of divergence and curl can provide information on interesting motion patterns.

We are interested in the estimation of *local* properties of flow fields derived from image sequences and we aim to derive measures for the noise in these local estimates. Non rigid objects in image sequences show local deformations that cannot be described by global estimations.

Estimation of divergence and curl in these flow fields is mostly used to determine the motion of the observer. This means that the total optical flow field on the retina of the observer has a global divergence or curl component due to the ego motion. The motion related to these patterns originates from the motion of a rigid environment relative to the observer [80], [46], [152]. This results in estimation of global flow properties, such as focus of expansion and time to collision or rotation relative to a rigid surrounding. Therefore these methods are not suited for describing local flow field properties.

Divergence and curl can be estimated in several ways, such as making use of oriented line segments, or by tracking closed contours [87], [41]. These estimates of divergence and curl provide global properties of flow fields and are therefore inappropriate for estimating local flow field properties.

A flow field can be decomposed in a divergence term, a curl term and a deformation term [92] and [98]. In these cases flow fields on the retina of the observer in a rigid environment are decomposed to describe the motion of the observer and the three dimensional structure of the scene. Local differential operators on flow fields are proposed, however no evaluation of the estimation of the divergence and curl are given. Furthermore applications are towards global description of flow field properties.

Since we are interested in the robust estimation of the local divergence and curl of vector field images, we aim to describe the expected variance of filter responses given the variance in the flow fields. Besides the noise in the estimation also evaluation of bias of the estimation and the behaviour of the estimations in case of abrupt changes in the vector field is described as they frequently occur at the transition of objects to the

background.

4.3. Divergence and curl in 2D vector fields

A vector function $\tilde{\mathbf{F}}(\tilde{\mathbf{x}})$ is a function that is defined on some point set D in space and associates with each point $\tilde{\mathbf{x}}$ in D a vector $\tilde{\mathbf{F}}(\tilde{\mathbf{x}})$.

Let $\tilde{\mathbf{F}}(\tilde{\mathbf{x}})$ be a differentiable vector function, and let $F_1(\tilde{\mathbf{x}})$ and $F_2(\tilde{\mathbf{x}})$ be the components of $\tilde{\mathbf{F}}(\tilde{\mathbf{x}})$. Then the function

$$\nabla \cdot \tilde{\mathbf{F}}(\tilde{\mathbf{x}}) \equiv \frac{\partial F_1(\tilde{\mathbf{x}})}{\partial x} + \frac{\partial F_2(\tilde{\mathbf{x}})}{\partial y} \tag{4.1}$$

is called the *divergence* of $\tilde{\mathbf{F}}(\tilde{\mathbf{x}})$.
For the same vector function $\tilde{\mathbf{F}}(\tilde{\mathbf{x}})$ we can define the *curl* of the vector function in 2D as

$$\nabla \times \tilde{\mathbf{F}}(\tilde{\mathbf{x}}) \equiv [0, 0, \frac{\partial F_2(\tilde{\mathbf{x}})}{\partial x} - \frac{\partial F_1(\tilde{\mathbf{x}})}{\partial y}]. \tag{4.2}$$

Note that the curl is oriented out of the image plane. The sign gives the direction of rotation.

4.3.1. Estimation of Div and Curl, an indirect method

For computing motion in image sequences a few solutions are available. Among these solutions are correlation based methods, using simple block correlation to find new positions of these parts of images in following frames [10]. Alternatively phase based methods are applied for recovering image motion. They exploit the idea that a shift in spatial domain corresponds to a phase in the Fourier domain [66]. For reviews of different flow estimation methods see [11], [14].

A third class of methods is based on the gradient. They originate from the observation that for motion in an image where the intensity of moving parts in the image remains constant, the total derivative of the moving intensity is zero. This is also known as the *optical flow constraint* [63], [79]

$$\nabla I(\tilde{\mathbf{x}}, t) \cdot \tilde{\mathbf{F}}(\tilde{\mathbf{x}}) + I_t(\tilde{\mathbf{x}}, t) = 0, \tag{4.3}$$

with $I(\tilde{\mathbf{x}}, t)$ the image intensity, $\tilde{\mathbf{F}}(\tilde{\mathbf{x}})$ the optical flow field, and $I_t(\tilde{\mathbf{x}}, t)$ the time derivative of image intensity $I(\tilde{\mathbf{x}}, t)$. Note that the optical flow constraint is an underdetermined system for solving for the two-dimensional flow field $\tilde{\mathbf{F}}(\tilde{\mathbf{x}})$. To be able

to recover the flow field, additional constraints are needed. We will only describe a solution from the local constant flow methods. The assumption is made that image points within a small local region R will not show significantly different motion. This allows for combining multiple local constraints in a weighted least squares sense [100]. An error function $E(\tilde{\mathbf{F}}(\tilde{\mathbf{x}}))$ can be defined from local optical flow constraints, weighted with Gaussian weight function $W(\tilde{\mathbf{x}}; w)$ with width w.

$$E(\tilde{\mathbf{F}}(\tilde{\mathbf{x}})) = W(\tilde{\mathbf{x}}; w) * [\nabla I(\tilde{\mathbf{x}}, t) \cdot \tilde{\mathbf{F}}(\tilde{\mathbf{x}}) + I_t(\tilde{\mathbf{x}}, t)]^2 \tag{4.4}$$

The unknown flow field is found by minimizing $E(\tilde{\mathbf{F}}(\tilde{\mathbf{x}}))$ by setting the derivatives towards the two components of the flow field to zero

$$\nabla_{\tilde{\mathbf{F}}(\tilde{\mathbf{x}})} E(\tilde{\mathbf{F}}(\tilde{\mathbf{x}})) = \tilde{\mathbf{0}} \tag{4.5}$$

This results in

$$W(\tilde{\mathbf{x}}; w) * [\nabla I(\tilde{\mathbf{x}}, t) \nabla I(\tilde{\mathbf{x}}, t)^T] \tilde{\mathbf{F}}(\tilde{\mathbf{x}}) = -W(\tilde{\mathbf{x}}; w) * [\nabla I(\tilde{\mathbf{x}}, t) I_t(\tilde{\mathbf{x}}, t)]. \tag{4.6}$$

Which can be rewritten to

$$\tilde{\mathbf{F}} = (\mathbf{C}^T \mathbf{C})^{-1} \mathbf{C}^T \tilde{\mathbf{b}} \tag{4.7}$$

, with

$$[\mathbf{C}^T \mathbf{C}]_{\mathbf{x}} = \begin{bmatrix} W * I_x^2 & W * I_x I_y \\ W * I_x I_y & W * I_y^2 \end{bmatrix}_{\mathbf{x}}, \qquad [\mathbf{C}^T \tilde{\mathbf{b}}]_{\mathbf{x}} = - \begin{bmatrix} W * I_x I_t \\ W * I_y I_t \end{bmatrix}_{\mathbf{x}}$$

From Eq. (4.7) the flow field $\tilde{\mathbf{F}}(\tilde{\mathbf{x}})$ can be solved. For all derivatives Gaussian derivatives are used with width f.

From the flow field estimated by Eq. (4.7) the divergence and the curl can be estimated using Gaussian derivative filters, of width d, on the flow field components

$$\nabla \cdot \tilde{\mathbf{F}}(\tilde{\mathbf{x}}) = G_x(\tilde{\mathbf{x}}; d) * F_1(\tilde{\mathbf{x}}) + G_y(\tilde{\mathbf{x}}; d) * F_2(\tilde{\mathbf{x}}) \tag{4.8}$$

$$\nabla \times \tilde{\mathbf{F}}(\tilde{\mathbf{x}}) = [0, 0, G_x(\tilde{\mathbf{x}}; d) * F_2(\tilde{\mathbf{x}}) - G_y(\tilde{\mathbf{x}}; d) * F_1(\tilde{\mathbf{x}})]. \tag{4.9}$$

In this way an estimation of divergence and curl are given using derivatives of flow field components.

4.3.2. Estimation of Div and Curl, a direct Method

From the flow relation Eq. (4.7), which expresses the flow field $\tilde{\mathbf{F}}(\tilde{\mathbf{x}})$ at any given position $\tilde{\mathbf{x}}$, we can derive a direct estimate for the divergence and curl of the local

vector field by taking the derivatives with respect to x and y of the two vector field components of flow field $\tilde{\mathbf{F}}(\tilde{\mathbf{x}})$ (the derivation is not shown).

These relations give an expression for the divergence and curl in terms of first and second order image derivatives combined in a local area with a Gaussian weight function $W(\tilde{\mathbf{x}}; w)$, the combinations give filters of order eight. The number of components for direct estimation is high. This results in an addition of the noise present in each component, resulting in noisy estimates. Therefore direct estimation as presented is not used further in this paper.

4.4. Measurement Noise

4.4.1. Flow Fields

We are interested in the robust estimation of the divergence and curl of vector field images. Therefore we want an expression of the variance of the estimation. For an indirect estimation method the variance of the final result depends on the variance of the first step.

Usually error measures and confidence measures are expressed in single value estimates for convenience. To give the accuracy of flow fields Barron [11] defines a unit space-time vector to measure the angle between estimated and correct flow vectors. The same is done when deriving confidence measures for optic flow. In Barron's study [11] the smallest eigenvalue of a least-squares matrix is used. This eigenvalue gives only an indication for the sensitivity of the model, which is useful in the case one needs to decide if a given flow field is reliably estimated. However, we are interested in the variance of the estimated flow field. Hence we need an absolute value for the variance of flow instead of a relative ranking of flow vectors.

A study on the variance of optic flow is found in [56]. This study presents an expression for the maximum variance value of the estimated optic flow field. Assume that the measurements of the image time derivatives are corrupted with additional and independent Gaussian noise with diagonal covariance matrix $\Sigma_{\mathbf{b}} = \sigma_b^2 \mathbf{I}$. The covariance matrix of the estimated flow vectors is then [134], [9]

$$\Sigma_F = \sigma_b^2 (\nabla_b \tilde{\mathbf{F}})(\nabla_b \tilde{\mathbf{F}})^T, \tag{4.10}$$

where ∇_b is the gradient of $\tilde{\mathbf{F}}$ in the direction of $\mathbf{b}$. Using (4.7) this gradient equals:

$$\nabla_b \tilde{\mathbf{F}} = (\mathbf{C}^T \mathbf{C})^{-1} \mathbf{C}^T,$$

Taking the outer product of both sides and using equation (4.10) leads to

$$\Sigma_F = \sigma_b^2 (\mathbf{C}^T \mathbf{C})^{-1} \tag{4.11}$$

The diagonal entries in Σ_F equal the variances in the estimated flow field in the spatial directions of coordinate axis. However it is possible that the variance in one direction is much larger than the variance in the other direction, meaning that only one component of the flow field can be estimated accurately. This is the well known aperture problem [173]. Hence, we are not that interested in the variance in the directions of the axis but in the maximum variance in *a* direction.

The easiest way to quantify Σ_F for this maximum variance is a decomposition of $(\mathbf{C}^T\mathbf{C})^{-1}$ into $(\mathbf{C}^T\mathbf{C})^{-1} = \mathbf{S}\mathbf{\Lambda}\mathbf{S}^{-1}$. Here $\mathbf{S}$ is the orthonormal matrix which contains the eigenvectors and $\mathbf{\Lambda}$ is the diagonal matrix containing the eigenvalues of $(\mathbf{C}^T\mathbf{C})^{-1}$. Since $\mathbf{S}$ is orthonormal, the noise is most amplified in the direction of largest eigenvalue λ'_L. The eigenvector decomposition of its inverse $\mathbf{C}^T\mathbf{C}$ equals: $\mathbf{C}^T\mathbf{C} = \mathbf{S}\mathbf{\Lambda}^{-1}\mathbf{S}^{-1}$ and likewise the noise is most amplified in the direction with minimum eigenvalue of $\mathbf{C}^T\mathbf{C}$; we denote this as λ_m. We can now relate the maximum variance σ_L^2 in the estimated flow field vector $\tilde{\mathbf{F}}$ to our measurement matrix $\mathbf{C}$ and conclude that the maximum variance σ_L^2 in the estimated flow field thus equals:

$$\sigma_L^2 = \frac{\sigma_b^2}{\lambda_m}. \tag{4.12}$$

The maximum variance σ_L^2 is defined as the sensitivity measure of the flow estimation method. Thus if we know the covariance in the measurements Σ_b, then the sensitivity measure would provide us with a value for the maximum variance in the flow field. However we do not know Σ_b a priori and hence need an extra step to provide a variance measure derived from the estimations.

Let us assume that the estimated flow equals the real flow $\mathbf{CF} = \mathbf{b}$. The residual $\mathbf{e}$ then just equals the noise in the measurements. The noisy measurement $\underline{\mathbf{b}}$ is given by $\underline{\mathbf{b}} = \mathbf{b} + \mathbf{n}$, the real value $\mathbf{b}$ with additive noise $\mathbf{n}$

$$\begin{aligned} \mathbf{e} &= \mathbf{b} - \mathbf{CF} && (4.13)\\ &= \mathbf{b} + \mathbf{n} - \mathbf{CF} && (4.14)\\ &= \mathbf{n}. && (4.15) \end{aligned}$$

Thus the variance of the measurements σ_b^2 equals the expectance of $\mathbf{e}^T\mathbf{e}$

$$\sigma_b^2 = \varepsilon(\mathbf{e}^T\mathbf{e}). \tag{4.16}$$

Since we now have an estimate of the measurement variance, incorporating the sensitivity equation (4.12), gives the variance of the estimated optic flow

$$\sigma_L^2 = \frac{1}{\lambda_m}\varepsilon(\mathbf{e}^T\mathbf{e}) \tag{4.17}$$

If the number of measurements per region M is large we can simplify this equation using

$$\varepsilon(\mathbf{e}^T\mathbf{e}) \approx \frac{\mathbf{e}^T\mathbf{e}}{M}, \tag{4.18}$$

resulting in the following approximation of the estimated variance σ_L^2 of the flow field

$$\sigma_L^2 \approx \frac{\mathbf{e}^T\mathbf{e}}{M\lambda_m} \tag{4.19}$$

This measure gives an absolute statement about the estimation of the flow field. Knowing this value of the variance in flow field estimation, variances in derived measures can be derived by propagation of noise. In the following section we derive the variances in divergence and curl estimations assuming we have this estimation of the variances in the flow field.

4.4.2. Error Propagation in Div and Curl estimation

We are using Gaussian derivatives to estimate derivatives in images and vector fields. Since Gaussian derivatives are discrete convolutions we can write a Gaussian derivative in terms of its discrete weights a_i. Assuming all variables are independent and using the fact that weights a_i are noiseless, we find for the variance in derivative estimations, [9], [166]

$$\sigma_{G*I} = \sigma_I \sum_i a_i \tag{4.20}$$

From this relation we can derive the variance in the estimation of curl and divergence. The variance of the divergence (σ_D^2) and the curl (σ_C^2) can be derived from the variances in the x- and y-component of the vector field.

$$\sigma_D^2 = \sigma_{1x}^2 + \sigma_{2y}^2 + 2\sigma_{1x2y} \tag{4.21}$$

$$\sigma_C^2 = \sigma_{2x}^2 + \sigma_{1y}^2 - 2\sigma_{2x1y} \tag{4.22}$$

Where the variances σ_{ip}^2 are the variances of the derivatives of the component i in the direction p of the flow field. We consider it more useful to describe the variance of the vector field in terms of direction and length of the vectors. To this purpose we define the angle θ as the angle of the vector with the positive x axis. We describe the length of the vector by l

$$\tilde{\mathbf{F}} = \begin{pmatrix} l\cos\theta \\ l\sin\theta \end{pmatrix}. \tag{4.23}$$

The variance in $\tilde{\mathbf{F}}$ expressed in variances in the angle θ and length l, for independent noise in θ and l, becomes

$$\sigma^2_{\tilde{\mathbf{F}}} = l^2 \begin{pmatrix} \frac{\sigma_l^2}{l^2}\cos^2\theta + \sigma_\theta^2 \sin^2\theta \\ \frac{\sigma_l^2}{l^2}\sin^2\theta + \sigma_\theta^2 \cos^2\theta \end{pmatrix}, \tag{4.24}$$

assuming independent noise in the direction and length. Using this in the variances of the divergence and curl magnitude in case of independent noise we get

$$\sigma_D^2 = A_d l^2 \{\sigma_\theta^2 + \frac{\sigma_l^2}{l^2}\}, \tag{4.25}$$

$$\sigma_C^2 = A_d l^2 \{\sigma_\theta^2 + \frac{\sigma_l^2}{l^2}\}, \tag{4.26}$$

where $A_d = \sum_i a_i^2$ and d is the width of the filter related to A. So for a given noisy flow field the variance in the divergence and curl are equal for independent noise in the data of the flow field derivatives. The variance is linearly dependent on the variances in length and linearly dependent on the direction of the vector field. In addition the variance in direction is weighted with the length of the vectors in the vector field. For increasing filter width d the value of A_d decreases, lowering the variance in the estimation.

If the noise in the data of the flow field derivatives is correlated an extra term arises which is positive in case of divergence Eq. (4.21) and negative in case of curl estimation Eq. (4.22). In this case we can give an upper limit of the variance. The covariance σ_{1x2y} and σ_{2x1y} satisfy the Schwartz inequality [166],

$$|\sigma_{ipjq}| \leq \sigma_{ip}\sigma_{jq}. \tag{4.27}$$

If we substitute Eq. (4.27) into Eq. (4.21) and Eq. (4.22) for the variances σ_D^2 and σ_C^2 we find that [166]

$$\begin{aligned} \sigma_D^2 &\leq \sigma_{1x}^2 + \sigma_{2y}^2 + 2\sigma_{1x}\sigma_{2y} \\ &= [\sigma_{1x} + \sigma_{2y}]^2 \end{aligned} \tag{4.28}$$

$$\begin{aligned} \sigma_C^2 &\leq \sigma_{2x}^2 + \sigma_{1y}^2 + 2\sigma_{2x}\sigma_{1y} \\ &= [\sigma_{2x} + \sigma_{1y}]^2 \end{aligned} \tag{4.29}$$

The values of the variances will never exceed the values derived in Eq. (4.28) and Eq. (4.29). Thus if one knows the variances in the derivative estimations one can give a worst case estimation of the variances to be expected in the estimation of divergence and curl. In practice the correlation is expected to be small resulting in lower variance values than predicted by Eq. (4.28) and Eq. (4.29).

4.5. Experiments

4.5.1. Discontinuities in Vector Fields

The localization of divergence and curl estimation is influenced by discontinuities in flow fields. To get an impression of the behaviour at discontinuities, a one dimensional model of a discontinuity is examined. Let us consider a first order 1D signal $f(x)$ with a discontinuity at $x = 0$.

$$f(x) = \begin{cases} px + q & \text{if } x < 0, \\ rx + s & \text{if } x \geq 0. \end{cases} \tag{4.30}$$

Then filtering function $f(x)$ with a Gaussian with width d and taking the derivative to x yields:

$$\frac{\partial}{\partial x}(g(x;d) * f(x)) = \frac{1}{2}(p+r) + \frac{1}{2}(p-r)\mathrm{erf}(\frac{x}{\sqrt{2}d}) + (q-s)\frac{1}{\sqrt{2\pi}d}e^{-\frac{x^2}{2d^2}} \tag{4.31}$$

Thus the response at a discontinuity in the flow field is a function of the parameters of the discontinuity and the width d of the used derivative filter. The localization error is only depending on the width d of the derivative filter. The height of the response depends on the strength of the discontinuity.

4.5.2. Synthetic flow fields

The description of error propagation in indirect curl and divergence estimation (eq. (4.25) and (4.26)) predicts linear dependency on variance in vector length and linear dependency on relative variance in length. These relations are verified using a uniform flow field in the direction $\theta = \pi/4$, with no divergence nor curl. The vector length is set to unity. To this flow field Gaussian noise is added to the length and direction of individual vectors. To simulate realistic noise levels we choose the variances σ_θ^2 between $\sigma_\theta^2 = 0$ and $\sigma_\theta^2 = 0.1$ and the relative variance in length σ_l^2/l^2 between $\sigma_l^2/l^2 = 0$ and $\sigma_l^2/l^2 = 0.1$.

Two simulation experiments are conducted, one with only noise in orientation and one with only noise in length of the flow field vectors. The results of these two simulations are given in figures 4.1 a) and 4.1 b) respectively. From equations (4.25) and (4.26) we expect the variances to be linearly dependent on the variance in orientation

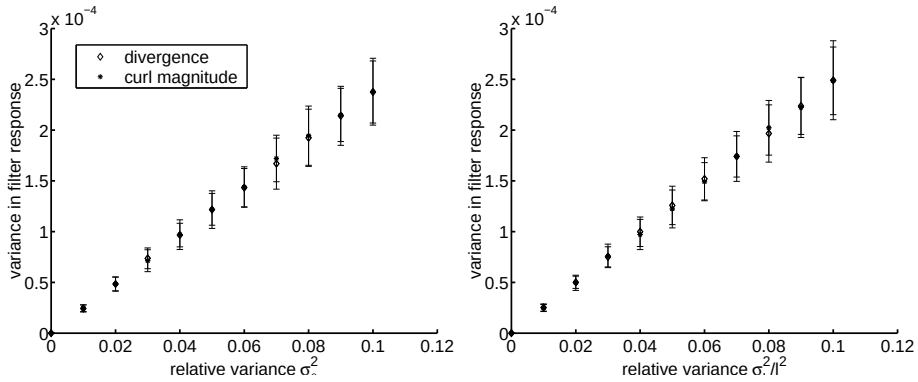

(a) Variance in curl magnitude and divergence as function of variance in vector orientation.

(b) Variance in curl magnitude and divergence as function of variance in vector length.

Figure 4.1.: Variance as function of variance in vector orientation and vector length for estimation of curl magnitude and divergence in case of uniform synthetic flow fields with no curl nor divergence ($l = 1$ and $\theta = \pi/4$).

and relative variance in length. Figures 4.1 a) and b) demonstrate this linear dependency. The observed slope is equal to the expected slope ($A_d l^2 = 2.5 \cdot 10^{-3}$, for filter width $\sigma_d = 2$). The variance in divergence and the variance in curl magnitude are equal as expected. Thus relations (4.25) and (4.26) apply for independent noise in variables vector length and vector orientation.

A second observation from equations (4.25) and (4.26) is the dependency of the variance on the length of individual vectors. Therefore flow fields with uniform curl magnitude or with uniform divergence are created. Again Gaussian noise is added to the orientation and length of the vectors. These vector fields have a position dependent orientation and length. Figure 4.2 a) shows the variance along a horizontal line. Figure 4.2 b) shows the relative variance σ^2/l^2. The relative variance is linear and horizontal with a spread of $1 \cdot 10^{-4}$. This demonstrates that the variance is depending on the length of the vectors as expected from theory, eq. (4.25) and (4.26). The noise added to the flow field has a variance of $\sigma_\theta^2 = 0.1$ in the orientation. The expected variance in the estimated divergence and estimated curl magnitude then is $\sigma^2/l^2 = 2.5 \cdot 10^{-4}$, for filter width $\sigma_d = 2$. If we compare this expected value with the estimated values of σ^2/l^2 in figure 4.2 b) we can see that the estimated values correspond with the expected

value. Thus the variance is vector length dependent.

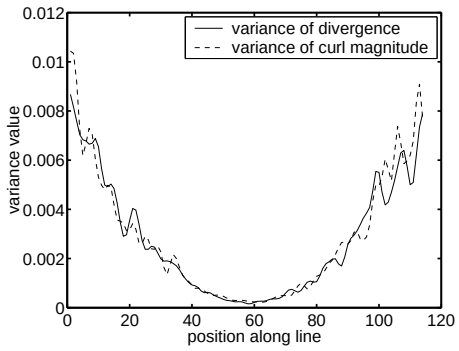

(a) Variance in estimation of curl magnitude along a horizontal line through the center of figure 4.2 a).

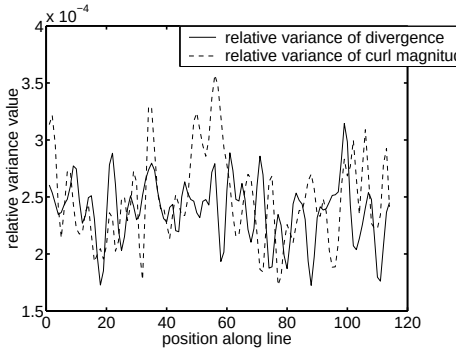

(b) Relative variance along a horizontal line through the center of figure 4.2 a).

Figure 4.2.: Variance as function of the position in the image for a synthetic flow field with uniform curl magnitude, with only noise in vector orientation ($\sigma_\theta^2 = 0.1$). The vector length is position dependent. In the figures the variance along a line at height $y = 60$ is shown. Figure a) shows the absolute value of variances $\sigma^2_{\nabla \cdot F}$ and $\sigma^2_{|\nabla \times F|}$. Figure b) shows the relative variance $\sigma^2_{\nabla \cdot F}/l^2$ and $\sigma^2_{|\nabla \times F|}/l^2$ along the line at height $y = 60$.

In this paper we take special interest in the behaviour of flow field estimators around discontinuities in the flow field. To this purpose we create noiseless flow fields with specific discontinuities highlighting the influence of vector length and orientation around these discontinuities. The discontinuous flow fields are given in figure 4.3 a) and b). Each figure gives a specific situation for a boundary. Figure 4.3 a) a flow field with discontinuity in direction is given. The upper part is a flow field with constant divergence and zero curl, while the lower part is a flow field with zero divergence and constant curl. In figure 4.3 c), d) e) and f) the resulting estimations for the divergence and curl magnitude are given. In case of figures 4.3 c) and d) the step strength increases with

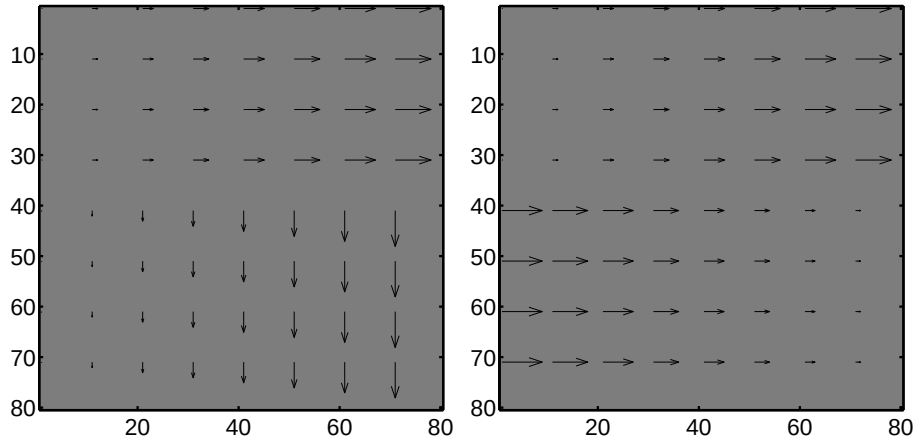

(a) Discontinuity in direction, the upper part is curl free and the lower part is divergence free.

(b) Discontinuity in length, the upper part and lower have divergence of opposite signs and are both curlfree.

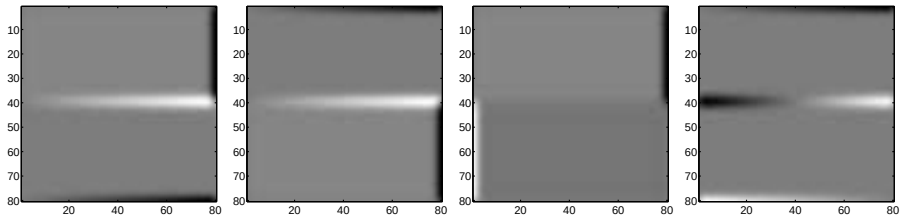

(c) Estimated divergence for flow field from figure a)

(d) Estimated curl for flow field from figure a)

(e) Estimated divergence for flow field from figure b)

(f) Estimated curl for flow field from figure b)

Figure 4.3.: Example flow fields with discontinuities and resulting estimations of divergence and curl.

increasing vector length. This results in an increasing response of the curl and divergence estimation with increasing step strength, while the width of the disturbed region remains the same. One can make a similar observation in figures 4.3 e) and f), here the orientation at both sides of the discontinuity is equal, but the length change is opposite at both sides of the discontinuity. Both sides are curl free flow fields with an opposite value of the divergence. We see that at the discontinuity a smoothed transition arises from one value of the divergence in the upper part to another constant value of the divergence in the lower part. Furthermore, although both parts of the flow field are curl free, we see a clear response of the curl estimation at the discontinuity. This response is depending on the step strength across the discontinuity, ranging from negative response to positive response. The width of the discontinuity response is constant over the discontinuity.

We see that the responses at discontinuities are depending on the step strength. Furthermore the width of the responses are constant for a given filterwidth d. From equation (4.31) we see that the width of the response is controlled by the filter width d and the strength of the response is depending on the step strength across the discontinuity.

The experiments on synthetic flow fields show the relation between the variance in flow fields and the variance in the estimated divergence and estimated curl, together with the influence of flow field discontinuities. For a given variance in flow fields the variance in the results is influenced by the width of the estimation filter d. Choosing a larger filter width results in lower variances provided that the area under the filter contains a flow field with constant divergence or curl. Smaller filters result in better localization The choice of filter width depends on the specific task at hand. For largely changing flow field properties within small areas and at discontinuities small filters are preferable. While for flow fields with smooth properties larger filter widths can be used.

4.5.3. Flow fields derived from synthetic image sequences

Sequences of known image motion are created with a publicly available ray tracing package [133]. In the experiment two sequences are created, leading ideally to a flow field with uniform curl by rotating the camera, $\nabla \times \tilde{\mathbf{F}}(\tilde{\mathbf{x}}) = -0.035$, and a flow field with uniform divergence by translating the camera towards the texture image, $\nabla \cdot \tilde{\mathbf{F}}(\tilde{\mathbf{x}}) = 0.05$ at the selected frame. The variance in the estimation of divergence and curl is length dependent. Thus to find the variance at each point, estimations are repeated for N=100 times. Furthermore to find the variance of the combination of flow estimation and divergence or curl estimation, each image sequence is constructed

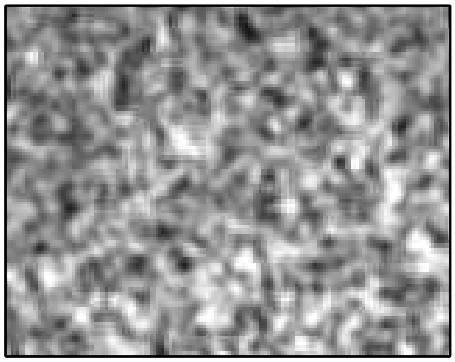

Figure 4.4.: Example image for random texture images.

from a new texture image. Where each new texture image is independent of the other texture images. The texture images are created from images with random intensity at each pixel. These images are low pass filtered with a Gaussian filter with a width of 1 pixel. An example of these texture images is given in figure 4.4.

The results of divergence and curl for a rotating camera are given in figures 4.5 and 4.6. In figure 4.5 the mean value and variance in curl magnitude are given for each pixel along a view line through the center of rotation. The mean value is a constant value, as expected for a flow field with uniform curl magnitude. For divergent motion, results are similar (see figure 4.6). In conclusion, the estimation of the divergence and curl corresponds with the divergence and curl as expected in the image sequences. Furthermore the noise levels in the divergence and curl are of such an order that a clear discrimination can be made between curl free flow fields and flow fields with curl, the same holds for the estimation of divergence. It is also concluded that there is a difference between the variances in the estimation of divergence and estimation of curl. This difference indicates that noise in the vector field derivatives is correlated. However, the correlation is small compared to the worst case derived in eq. (4.28) and eq. (4.29).

The correlation is further examined by taking an image sequence consisting of only uncorrelated noise. Thus in the sequence no object is created and thus no motion is

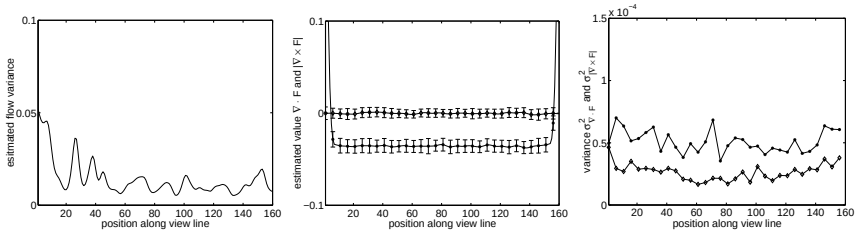

(a) Flow variance σ_L^2 along view line, estimated for a single measurement.

(b) Curl magnitude (lower curve) and divergence (upper curve) along view line, after $N = 100$ different random texture images with rotational motion around the centre.

(c) Variance value of the curl magnitude (upper curve) and divergence (lower curve) along view line, after $N = 100$ different random texture images with rotational motion around the centre.

Figure 4.5.: Estimation of curl magnitude and divergence for a rotating camera imaging a random texture image. Rotation with angular speed $\omega = 2\pi/360$. The experiment is repeated for $N = 100$ different random texture images, to exclude the influence of a single texture image.

present. The estimated flow field is expected to be a zero field, with noise. From this zero field divergence and curl are estimated. Figure 4.7 demonstrates the difference in variance for divergence and curl. This implies that noise in the flow field is correlated.

Another observation from figures 4.5 and 4.6 is that the relative variance in flow (relative to the length of flow field vectors) is large for small flow field vector length. The resulting variance is a multiplication of the squared vector length and the variance in flow field. This results in larger relative variances at the center of the rotation and divergence.

The combination of flow estimation and divergence or curl estimation gives the resulting variance in the estimations. For different values of the three filter widths, involved in indirect estimation experiments are repeated on a smaller scale. From the three filter widths involved two are used in the flow estimation, the width of derivative filters f and the width of local smoothness w. The third width is the width of the divergence

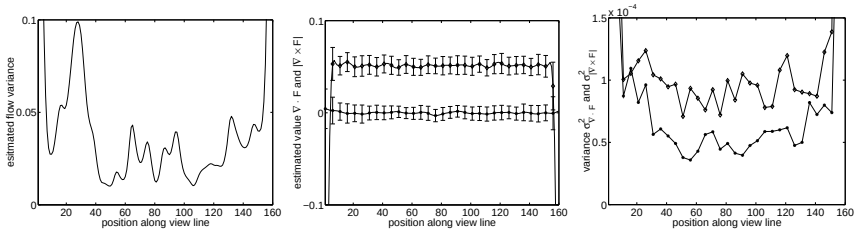

(a) Flow variance σ_L^2 along view line, estimated for a single measurement.

(b) Curl magnitude (lower curve) and divergence (upper curve) along view line, after $N = 100$ different random texture images with translational motion towards the centre.

(c) Variance value of the curl magnitude (lower curve) and divergence (upper curve) along view line, after $N = 100$ different random texture images with translational motion towards the centre.

Figure 4.6.: Estimation of curl magnitude and divergence for a translating camera imaging a random texture image. The real divergence is $\nabla \cdot F = 0.5$. The experiment is repeated for $N = 100$ different random texture images.

and curl derivative filters d. The variances are computed after $N = 10$ measurements. In figure 4.8 the variance along a view line through the center of the image are given corresponing to the different filter settings. This figure demonstrates the role of different filterwidths. Using larger filters for divergence and curl estimation results in lower variances and thus in better estimations for constant flow fields. The influence of flow filter widths is different. The resulting variance is a combination of texture in the image and the motion in the image. Thus the filter settings for the flow estimation need to be adjusted at the motion present in the sequence, while the filter width for divergence and curl estimation need to be adjusted according to the size of the area with constant divergence or curl.

Texture is important when estimating correct flow properties. Since texture is a property of objects in the scene in image sequences, texture can be a problem. To demonstrate the importance of image texture a few textures from the Brodatz texture image database are used and two extreme cases 'star' and 'circular' texture. The images from the Brodatz database are manually selected based on the randomness and density of

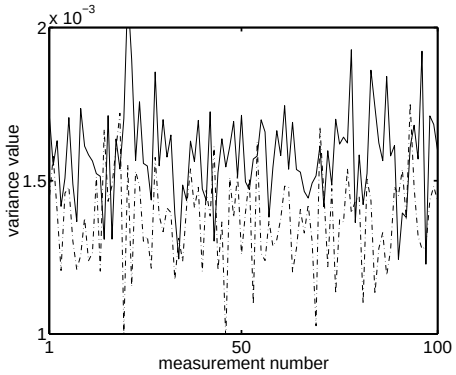

Figure 4.7.: Variance in curl and divergence for N=100 measurements, the solid line is divergence variance and the dashed line is curl variance.

the texture. (selection D5, D100 see figure 4.9, other textures not shown). The 'star' and 'circular' textures are good examples for showing the importance of visual motion cues in image sequences. The star shaped texture 'star' results in a poor estimate of the divergence for a divergent motion, while for rotational motion results are appropriate (data not shown). The circular texture 'circular' shows the opposite behaviour. In comparison, the Brodatz textures offer reliable estimated of both divergence and curl in rotational as well as diverging motion (data not shown). It is concluded that, as long as objects show enough random structure, flow estimation and thus divergence and curl estimation will perform well. However in the case of extreme textures, such as the 'star' texture or the 'circular' texture, flow estimation and finally divergence and curl estimation will show large errors compared to the actual motion of the objects. In these cases no reliable divergence and curl estimations are possible.

Discontinuities in flow fields cause a response in the estimation of divergence and curl. This response depends on the strength of the discontinuity and the width of the filter as is seen in other experiments. This experiment uses a non-moving foreground object in front of a rotating background. The rotation of the background ideally gives a flow field with constant curl. The divergence is ideally zero. The resulting estimation of curl and divergence are given in figure 4.10. The flow field (fig. 4.10 b)) shows the estimated motion in the sequence. At the boundary of the circular object flow vectors are estimated incorrectly due to the discontinuity in the image data. The estimated curl (fig. 4.10 c)) and the estimated divergence (fig. 4.10 d)) show values zero at the object

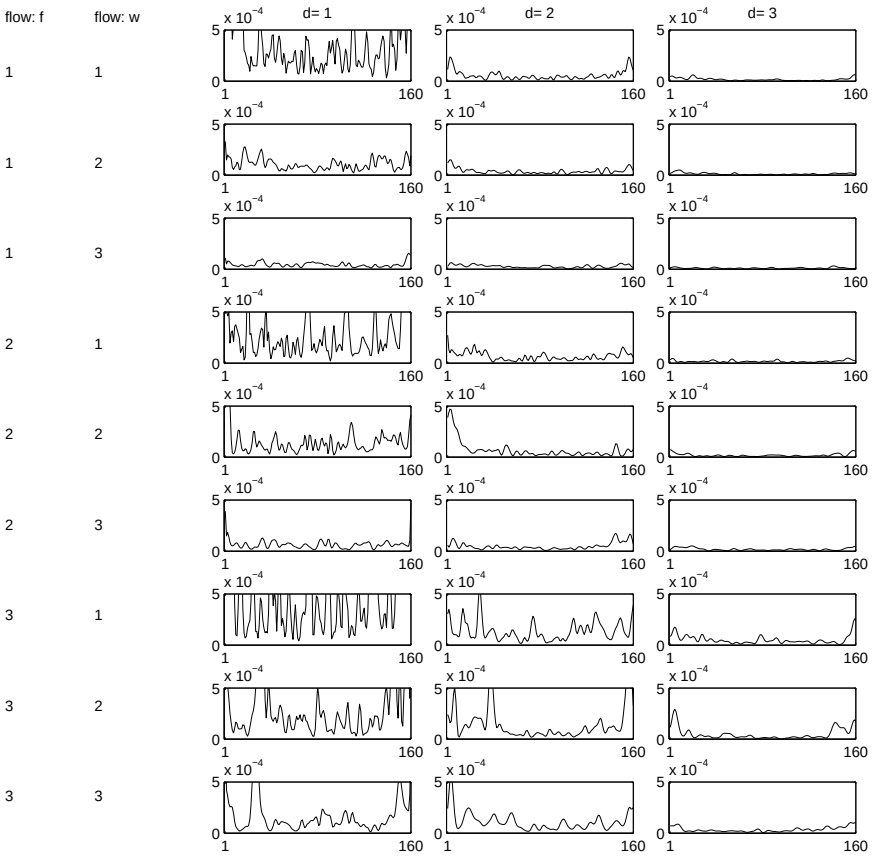

Figure 4.8.: Variance values along view line for divergence estimation in case of a rotating texture. The first column are variance plots with divergence filter width $d = 1$. The second column are variance plots with divergence filter width $d = 2$. And the third column are variance plots with divergence filter width $d = 3$.

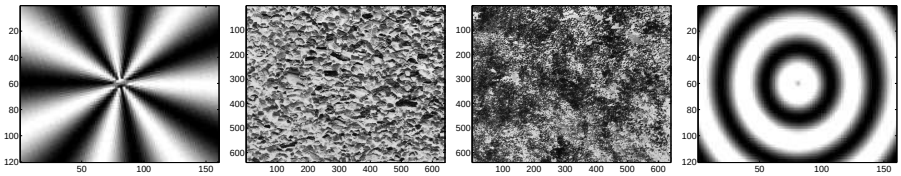

(a) Image of star shaped texture 'star'

(b) Brodatz D5

(c) Brodatz D100

(d) Image of circular shaped texture 'circular'

Figure 4.9.: To try out the method two example images of good textures b) and c) [32], and two examples of bad textures a) and d).

position (gray intensity value). The curl at the boundary show strong negative values (dark intensity values) due to the change from long vectors to vectors with length zero. The response is largest at the positions along the boundary with largest distance to the centre of the image, the vector length increases with increasing distance from the centre.

The divergence at the boundary shows a positive response at the lower right part of the object (light intensity values) while a negative response is shown at the upper left part of the object (dark intensity values). On the object boundary at the centre of the image and at the opposite position the response in divergence is zero as expected. At these positions the velocity vectors are tangential to the object boundary, resulting in low divergence response.

4.5.4. Crawling human T-cell, flow, divergence and curl results

On an image sequence of a crawling human T cell [1] flow estimation and derivation of divergence and curl is demonstrated. The sequence consists of 150 frames of 288 by 244 pixels gray value. In the following figures the image frame with corresponding estimated velocity field and the divergence and curl are given. For visualization purposes, the velocity field is drawn on a grid with grid distance 5 pixels. The individual velocity vectors are enlarged by a factor 5. For the divergence and curl only areas with a value larger than a certain threshold (t=$\pm$0.15 in this case) are shown. Thus only

[1] obtained from http:\\keck.biology.uiowa.edu

areas with a high response are depicted.

The figure demonstrate the following important results

I: At the boundary of the object a high response of both the divergence and curl can be noticed. The object boundary is a boundary between the object with a high intensity structure and a low intensity structure background.

II: Divergence response is high at areas where material contracts. In figure 4.11 a part of the sequence is shown where an extending part is retracted to the cell. The retraction corresponds with a collapse of the area of the extending part.

III: A high response of curl estimation can be appreciated at frames where the inner material of the cell is ”squeezed” through a narrow stretched part of the cell. In figure 4.12 this process is shown with the corresponding estimation of the divergence and curl.

4.6. Discussion

A theoretical and experimental evaluation is carried out for estimating local divergence and local curl in dense vector field images. Equations predicting the variance in estimated divergence and curl have been derived. It was shown that they correspond well with experimentally determined variances in divergence and curl.

Synthetic flow fields show that for independent noise in the flow field data, variance in the estimation of divergence and curl is predictable (Eq. (4.25), (4.26)) once the noise in the flow field is given. However the noise in the real flow field is not independent, but correlated. Still the examination of independent noise is of interest because this gives a lower bound for the variances of the estimations, one cannot do better than these figures predict. On the other hand one can give an upper bound for dependent noise (eq. (4.28), (4.29)). The resulting variance in the estimation will be between these two bounds.

Estimation of divergence and curl from synthetic image sequences show that the accurate estimation is crucial to the estimation of divergence and curl.

For divergence and curl estimation a sequence of a crawling human T cell is shown. Reasonable divergence and curl estimations are possible. The estimations of the divergence and curl are clear at object boundaries. These boundaries correspond with discontinuities in the velocity vector field. These discontinuities give rise to a significant

response in divergence and curl estimation. Also significant response is clear at motion field properties corresponding to object contraction (divergence response) and material repositioning through a narrow duct when the cell is ”crawling” (curl response). The shown responses of the divergence and curl are a result of the used filter widths of the different filters used. That means that for estimating divergence and curl a specific area is incorporated around a given position of estimation. The filterwidth chosen in the divergence and curl estimation (3 pixels) enables the estimation over small areas inside the cell.

In appendix A a similar result is shown on a complete different type of image sequence. A blooming flower

Divergence and curl estimation depends on the estimation of the flow field. Errors occurring in the flow field estimation propagate through to the divergence and curl estimations. Errors in flow fields divide into two categories: systematic and stochastic. Systematic errors are due to working conditions which deviate from the model assumptions, such as occlusion or insufficient structure in the image. Systematic errors are more difficult to handle. Discontinuities in the flow field due to occlusion, will always result in a false response of divergence and curl. In a proper estimation scheme object boundary detection should overrule the curl and divergence discontinuities, as the interest at object boundaries shall be in their presence. This means that improvement of a flow estimation method for occlusions (e.g. [21]) will not change the high responses of the divergence and curl significantly. Stochastic errors are given by the flow variance σ_L^2 as derived in Eq. (4.19) [56]. The flow field variance leads to an estimate of the error in the divergence and curl without actually computing them. The flow field variance is preferred over other confidence measures [11] on flow estimation, because the variance provides an absolute measure. In this way a reliability measure is available even before the quantity itself is computed.

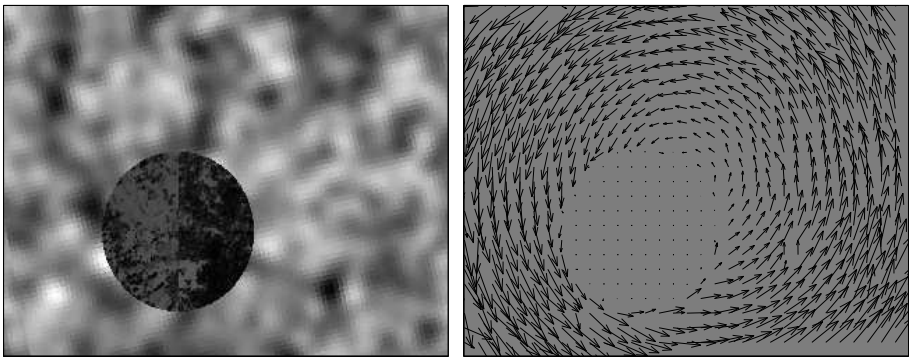

(a) Image sequence with non-moving foreground object and background rotating around the centre.

(b) Flow field as estimated by optical flow method.

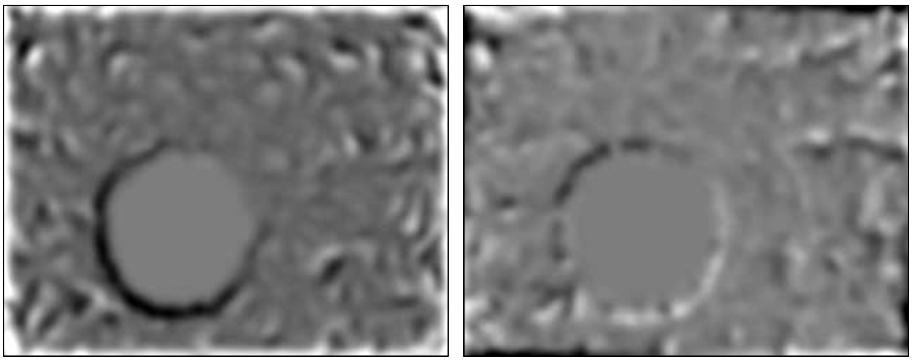

(c) Curl magnitude of flow field from figure b).

(d) Divergence of flow field from figure b).

Figure 4.10.: Simulated occlusion of a rotating camera. The objects are fixed relative to the camera in this way occlusion of the scene is created. The curl magnitude and divergence show responses at the boundaries of occluding objects.

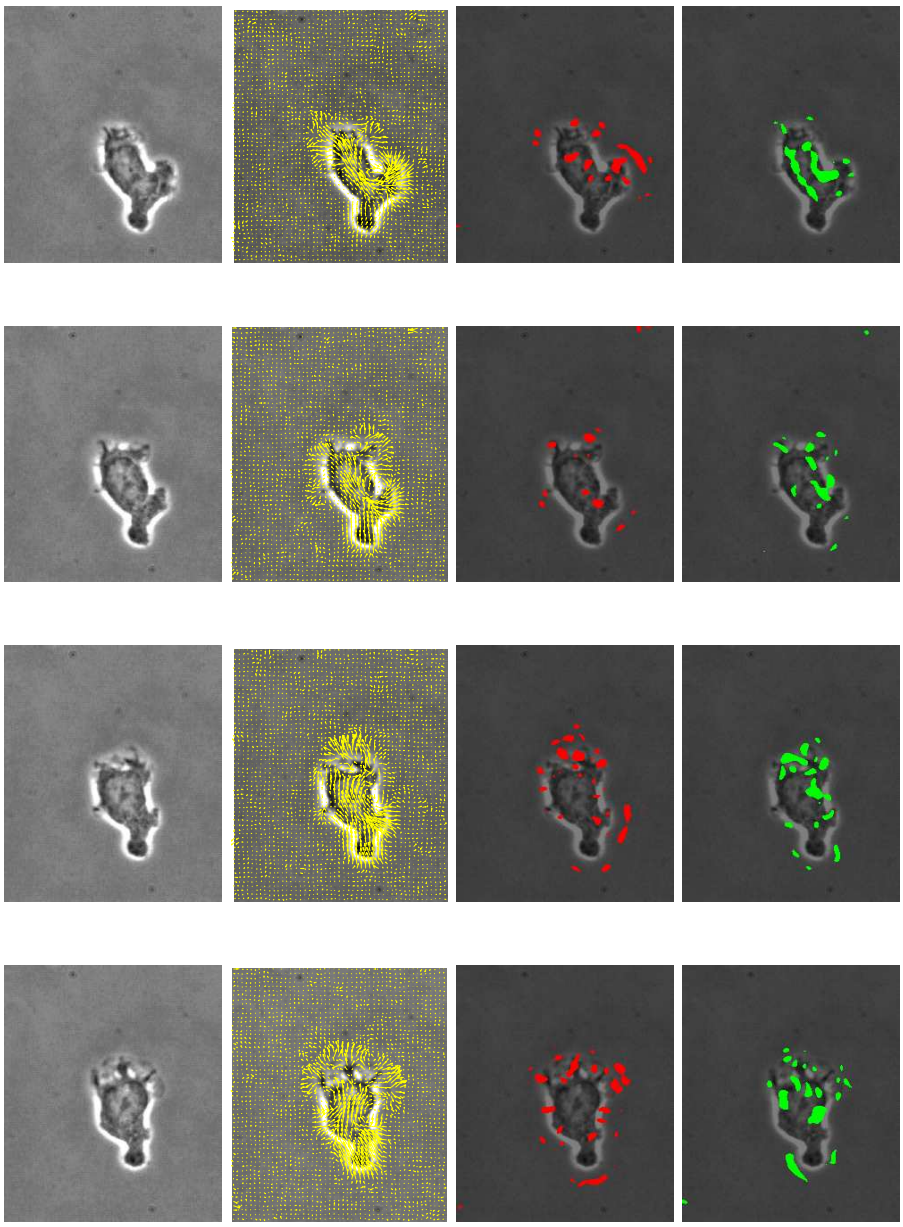

Figure 4.11.:

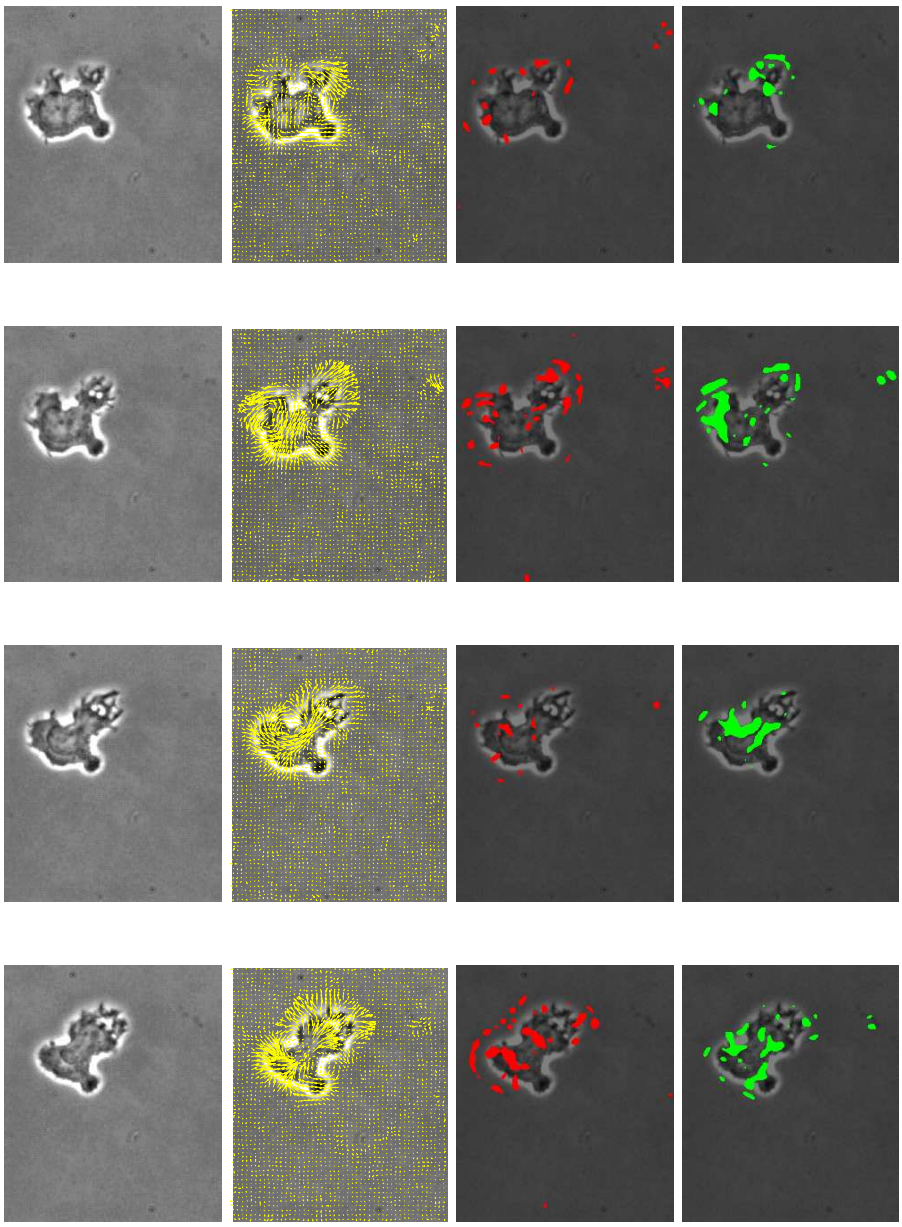

Figure 4.12.:

5. Motion Characterization of Shapeless Objects and Blob Patterns

5.1. Abstract

Motion properties of groups of markers can be estimated using the geometrical arrangement of these markers. These markers can represent single cells, small objects inside cells or boundary points of shapeless objects.

The divergence and curl of an arbitrary closed polygon can be estimated using basic theorems, assuming constant divergence and constant curl within this closed polygon. To construct such a polygon the geometrical arrangement of the markers is used. In case of shapeless objects the positions of the markers are updated according to the motion of the objects, together with an update in the amount of markers to provide an optimal geometrical arrangement.

The estimation of divergence and curl is demonstrated on two image sequences. The first image sequence shows an arrangement of telomeres inside a cell nucleus. The small expansion and the cell rotation are estimated using the presented method. In the second image sequence the mitoses of a living cell is recorded. The expansion is estimated using the presented method.

The presented method gives an estimation of the deformation of the geometrical arrangement of markers. The estimation of the divergence and curl shows the estimation of, in principle, differential properties of a dense motion vector field. This with a method that only uses a sparse geometrical arrangement of markers. Thus coarse time sampling, inherent to imaging of living cells, is of small influence on the estimation of divergence and curl. However undersampling will result in erroneous results.

5.2. Introduction

Walking though the grasslands one occasionally encounters flocks of birds with, by the eye, an uncountable number of individual birds. The flight of such a flock of birds is an entity by itself. The description of the flock does not stop at the description of all individual flight patterns. The dynamic geometric arrangement reveals complex motion patterns. Describing the motion properties of a flock of birds requires a computational method that keeps track of individual birds *and* of the geometrical arrangement of the group as a whole.

Much like motion patterns in a flock of birds, the motion pattern of cellular bodies in living cells or entities in living tissue also is a dynamic geometrical arrangement. The motion pattern is specific in the sense that one may characterize tissues [37], [123], [48], [72] from it. Similarly, in this paper we argue that the motion pattern of particles studied as a whole can be used to characterize tissues and cells. In this chapter, we propose a method for group motion description based on the dynamics of the geometrical arrangement of particles.

In the absence of other descriptions, the geometrical arrangement of cells can be captured best from the distances between particles or other conspicuous entities. From mathematics we adopt the best way to describe a pattern of dots by a neighbor graph known as the Voronoï graph.

In microscopy, the objects we are interested in are in the majority of cases in size equal to or smaller than the point-spread function of the microscope. Then, the appearance of these blobs will have no visible internal structure. This we take as our definition of a blob, namely: any particle which show no internal structure. Any such blob can be represented in good approximation by a Gaussian-shaped intensity profile as described in chapter 3. Having defined the blob as a structure-less entity, we are permitted to reduce the shape of the particles to a point at the centre of the blob. We follow a description of the dynamic pattern by reducing the cell or tissue first to a set of points, one to each centre of a particle.

Local changes in dynamic point sets are conveniently described by geometrical invariants. The most prominent ones are divergence and curl [93, 41]. These measures are independent of the choice of coordinate system. The divergence and curl are related to the change in the shape of the pattern of connected lines spanned between the points in the set. Deformations to the graph caused by (local) object expansion or (local) torsion are described in terms of divergence and curl.

The common way to estimate curl and divergence is to measure them from the complete (dense) motion field. Numerous solutions exist for estimating motion in image sequences. Horn and Schunk [79] describe the most basic method to derive a dense motion vector field from image sequences based on spatial and time derivatives of im-

age intensities in the sequence. However, for image patches with no intensity structure, as we have to deal with, their solution is ill-posed. The field between the blobs shows little or no internal texture. Hence, estimates for the motion field are unstable almost everywhere and can not be used [41]. The goal of this chapter is to find an alternative method to estimate these invariants from image sequences.

Our work on the estimation of the dynamics of the geometrical architecture of tissue is motivated by [74]. A Delaunay triangulation is the basis of a simple algorithm for image segmentation. We use a similar method, now applied to motion analysis of a pattern of points. From this architecture one easily derives the geometrical invariants for each of the triangles spanned between the points in the set.

5.3. Related Work

We give an overview of related work using a classification of image sequence segmentation as given by Zhang and Lu [192]. They conclude that motion-based approaches start from optical flow estimation, change detection, or motion parameter estimation. Segmentation based on motion estimation alone unlikely generates an accurate result due to noise generated over-segmentation it results in. In addition, the methods commonly suffer from a difficult initialization. At the same time the computational complexity is considerable and hence the applicability is limited. Therefore, many segmentation schemes use spatio-temporal filtering to start from as such an approach will produce more stable results. Zhang and Lu share this conclusion stating that spatio-temporal approaches are robust and applicable to non-rigid motion.

The most primitive method of segmentation in still images is matching a known template. Usually, some deviation is permitted to the template, to be able to fit the template to a variety of shapes of biological origin. Felzenszwalb [62] demonstrates fitting a triangular template, using non-rigid deformation, exploiting the fact that any simple polygon describing a boundary can be triangulated. In this triangulation it is then sufficient to find the boundary rather then the interior of the object. This requires a good definition of a boundary. The paper gives a good example of the flexibility as obtained with the triangulations of objects.

A connection between template matching and spatio-temporal segmentation approaches can be found in the work of Sclaroff [146]. Sclaroff describes template tracking by a well-defined initial template. Then, the non-rigid deformation of objects is taken into account. To that end, tracking is posed as a mesh registration over time. A minimum warping error defines the parameters of the optimal registration. The optimum registration is found by modal matching of the mesh to the frames in the image sequence. The proposed method of active blobs tracks some objects with success. However, the

implicit assumption is that the object is required to be highly textured. The method will perform poorly on low textured objects.

Celasun et. al. [36] propose a mesh-based object segmentation in video. A 2D-mesh by Delaunay triangulation is used on feature points. The mesh describes objects as they move in the sequence. The updates of the mesh-positions are computed with the method of Lucas & Kanade [100]. The proposed method relies on the computation of optical flow. Hence it relies on the presence of image structure for a reliable estimate. The method shows good tracking results without the necessity of user initialization. Drawbacks of the method are a need for motion vector computation, reliability on hard boundaries on the objects and the need of constraints to find good object boundaries.

5.4. Materials and Methods

5.4.1. Sample Preparation, telomeres sequence

For life cell observation, U2OS cells (derived from a human osteosarcoma) were cultured on coverslips in $3.5cm$ petridishes (Mattek, Ashland, Ma.) in RPMI 1640 culture medium, without phenol red, supplemented with 5% fetal calf serum and buffered with $25mM$ Hepes buffer to pH 7.2 (Life Technologies, Breda, The Netherlands). The Cy3 labelled (C3TA2) PNA probe was kindly provided by DAKO, Glostrup, Denmark. The probe was dissolved to a final concentration of $1mM$ in a buffer containing $80mM$ KCl, $10mM$ K_2PO_4, $4mM$ $NaCl$, (pH 7.2) to a final concentration of $1mM$, and was added to the cells. To label the cells glass bead loading was performed as described by McNeil et al [112] using alkali washed glass beads. The PNA probe hybridize specifically to telomeric DNA repeats in living U2OS cells, resulting in similar fluorescence signals as on fixed chromosomes and nuclei [95], [49]. Images were acquired using a Zeiss CLSM 510, with a Zeiss Plan-Neofluar 100x/ N.A. 1.3 oil objective. Cy3 was excited using the $543nm$ laser line. The image series consists of 70 stacks of 16 Z-slices, size 128x128 pixels taken with 1-minute time intervals. The total sequence thus comprises 70 minutes.

5.4.2. Sample Preparation, mitose sequence

The recordings of a HeLa cell line expressing histone H2B-GFP (cell line 2-12-HeLa; Kanda *et al.* [88]) were kindly provided by Dr. E.M.M. Manders (University of Amsterdam, Amsterdam, NL) [103]. Cells were grown in DMEM (Gibco, Life Technologies Ltd, Paisley, UK) supplemented with 10% FCS (Gibco), glutamine and penicillin/streptavidin at $37°C$ and 5% CO_2 in glass-bottom microdishes (MatTek, Ash-

land, MA). Two hours before imaging, the medium was replaced py prewarmed DMEM without phenol red (Gibco) supplemented with 10% FCS, glutamine, penicillin / streptavidin and free radical scavenger Trolox (0.1 mmol/L; Sigma-Aldrich Chemie BV, Zwijndrecht, The Netherlands). The glass-bottom plate was placed on a heated microscope stage ($37°C$, Zeiss, Jena, Germany). An objective heater (Bioptech, Butler, PA) was used to keep the microscope objective at $37°C$. To stabilize the temperature, cell cultures (60% confluent) were kept on the microscope stage for at least 2 h prior to imaging.

5.4.3. Image Acquisition and Software

Images were captured with a Zeiss LSM510 using a Plan-Neofluar 100x / 1.3-oil objective (Zeiss, Jena, Germany) and an Ar-ion laser tuned at $488nm$ and less than $500nW$ laser power at the position of the cells, to prevent cell death [105]. 10 3D images each containing 31 optical sections (256x256 pixels) were scanned with a voxel size of $18nm$ lateral and $70nm$ axial.

For image processing Matlab R14 (The MathWorks, Inc., Natrick MA, USA) was used. Additionally, the Signal Processing toolbox and the Image Processing toolbox (The Mathworks, Inc., Natrick MA, USA) are used. This high-level language scientific software suite is expanded by user written source code for adaptive triangulation.

5.4.4. Deformable Mesh Motion Estimation

Delaunay Graph

Consider an image sequence of a living cell or a tissue containing living cells. Detection of objects of interest will result in a marker set M. Let V be the set of m markers, $V = \{v_1, v_2, \ldots, v_m\}$, a subset of M ($V \subset M$). A graph $G(V)$ defines how elements of V are connected in a Delaunay graph. A Delaunay-graph gives the triangulation of the convex hull of the set of markers V. The triangulation is such that every circumcircle of a triangle contains no other points. It is empty apart from the points which make up the circle. It is guaranteed that such a solution does exist, as can be seen from defining its dual graph. In $\mathbb{R}^2$, the Delaunay-graph is the dual of a Voronoï graph. A Voronoï graph is defined by polygons $Z(p)$, where each polygon defines the area for which all points are closer to marker p than to any other marker [182].

Deformable Mesh

Consider a Delaunay-graph $G(V)$ at time t of markers V. The Delaunay-graph $G(W)$ at time $t + dt$ will be identical to $G(V)$, under the assumption that the geometrical arrangement is constant within time intervals dt. Implying that the set of markers W at time $t + dt$ is the same as the set of markers V at time t.

Let the positions of the m markers be defined by m positions $\mathbf{p(t)}$, $P(t) = \{\mathbf{p(t)_1}, \mathbf{p(t)_2}, \ldots, \mathbf{p(t)_m}\}$. Then, the geometrical arrangement is defined by $G(V)$ with positions $P(t)$ of markers V.

The above construction is referred to as a deformable mesh. The mesh is allowed to deform over time, as is described by the displacement of the markers. Usually the deformation of the mesh is written as a minimization problem of the image warping error for each triangle. Rather than minimizing a matching process (e.g. [184]), the image segmentation error here is minimized by introducing new markers to the set V from the marker set M, to fulfill the minimization criterion for the image segmentation, see section 5.4.5.

Mesh Deformation Measurements

One can measure the deformation by calculating the displacement of each individual marker. However, the geometrical layout provides more information.

Consider, in $\mathbb{R}^2$, an arbitrary area A with boundary ∂A. Let $\vec{v}$ be a vector field defined on area A. Then, Gauss's theorem (or divergence theorem) states that:

$$\oint_{\partial A} \vec{v} \cdot \vec{N} dl = \iint_A \nabla \cdot \vec{v} da \tag{5.1}$$

Stokes's theorem states that:

$$\oint_{\partial A} \vec{v} \cdot \vec{T} dl = \iint_A \nabla \times \vec{v} da \tag{5.2}$$

with $\vec{T}$ the tangential vector at l and $\vec{N}$ the normal vector at l to boundary ∂A.

Suppose we have a boundary of an area defined by a polygon. Then, motion of the vertices of the polygon can be seen as only a few sample vectors from a dense vector field. Under the assumption of constant divergence and constant curl inside the closed polygon, Gauss's theorem and Stokes' theorem can be rewritten into:

$$\nabla \cdot \vec{v} = \frac{1}{A} \oint_{\partial A} \vec{v} \cdot \vec{N} dl \tag{5.3}$$

$$\nabla \times \vec{v} = \frac{1}{A} \oint_{\partial A} \vec{v} \cdot \vec{T} dl \tag{5.4}$$

The right hand sides of equations (5.3) and (5.4) are estimated from the displacements of the markers $V \subset M$ that define polygon of the boundary ∂A. A linear interpolation of the displacement vector over the boundary is applied (see figure 5.1).

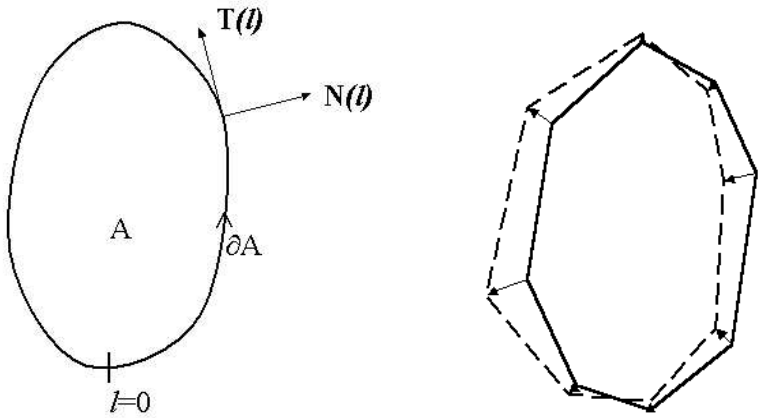

(a) (b)

Figure 5.1.: a) Definition of a contour with tangential vector $\vec{T}$ and normal vector $\vec{N}$ b) Example of a closed polygon with displacement vectors

5.4.5. The Process of Mesh Deformation

In figure 5.2 the motion segmentation and mesh deformation is given schematically. For each frame a point-set is extracted as shown schematically in figure 5.3. The frame is thresholded and segmented. Then, object contours are defined. The contours define the order of the points along the contour. From local curvature maxima and minima

are extracted. The curvature maxima and minima form point set V. Figure 5.4 depicts

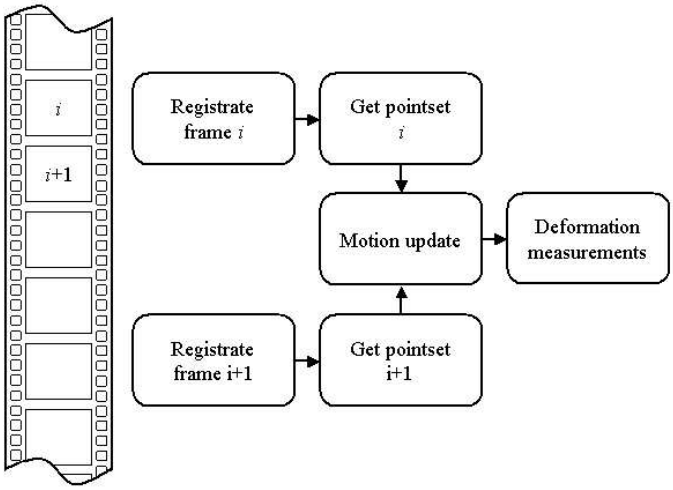

Figure 5.2.: Motion segmentation and mesh deformation method.

the motion update. From the point set at frame i all points are connected to their corresponding point in the point set of frame $i + 1$. The correspondence is derived from the curvature value of the points, the order of the points along the contour and the Euclidean distance between a point at frame i and a point at frame $i + 1$.

Motion estimation approach; segmentation

Marker definition The image is thresholded at an experimentally defined intensity level. positions with high isophote curvature and high intensity gradient are best find by $K = L_{vv}{L_w}^2$ is computed as described in [168]. The set of markers M^k consists of the local maxima and minima of K at frame k.

Segmentation The segmentation method starts at the first image of the sequence with the initial triangulation D^0. Markers in D^0 are set at the corners of the frame and the one position of highest curvature in the image. When the analysis has progressed to the

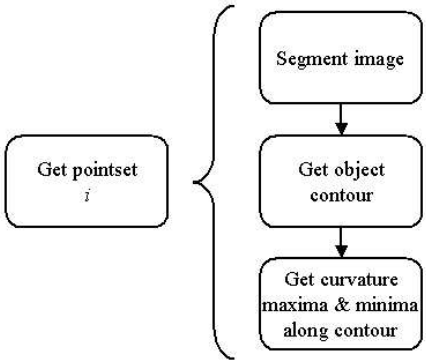

Figure 5.3.: detailed schematic of extracting pointsets

next image, the segmentation of the image is initialized by the previous segmentation after a motion update; $D_{i+1}^0 = D_i^N$.

Let D_k denote the incremental Delaunay-triangulation after k insertions of points in $\mathbb{R}^2$ and let d_l^k form the l^{th} triangle of the k^{th} triangulation. For $k = 0$ the triangulation is $D^0 = D^N$. The function $f : \mathbb{R}^2 \rightarrow \mathbb{R}$ defines an image surface $f(x, y)$, that is the still image from the sequence at $t = t_i$. $f_l^k(x, y)$ is a compact area of f bounded by the vertices of triangle d_l^k. S_l^k is a subset of M^k containing point x inside triangle d_l^k.

All triangles d_l^k are examined by computing a similarity predicate $H()$. When the similarity predicate is false, a new point is added inside the area of triangle d_l^k. For each point $\overline{x} \in S_l^k$ a transition error $E()$ is calculated. The point $x_{min} = min(E())$ with lowest transition error is added to D^k resulting in the next triangulation D^{k+1}, thus adapting the grid to the underlying image structure. This splitting phase continues until all triangles d_l^k satisfy $H()$ and yielding D^N.

Let us now define the similarity predicate $H()$. Assume that within a region T the values $f(x, y)$ are approximately constant. They are represented by their mean $\overline{f}$. We

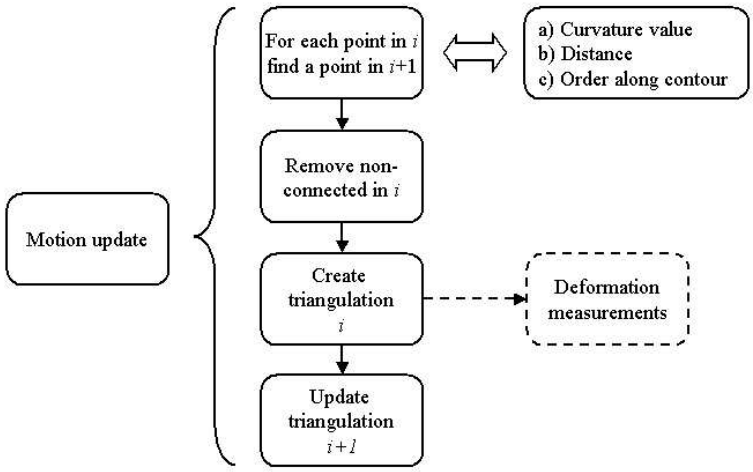

Figure 5.4.: detailed schematic of estimating motion correspondence from frame *i* to frame *i*+1

consider the similarity predicate of T to be true if the square error of the *image surface* f within T is small. The square error

$$H^{'}(T) = \sum_{x,y \in T} (f(x,y) - \overline{f})^2. \tag{5.5}$$

is used in the predicate function

$$H(T) = \begin{cases} \text{true} & \text{if } H^{'}(T) \leq t \\ \text{false} & \text{otherwise} \end{cases} \tag{5.6}$$

with threshold t, to be defined experimentally.

Motion update

Motion update initialization The motion update changes the triangulation D^N of the current frame into the initial triangulation of the subsequent frame. The displacement

of each of the vertices is determined as follows.

A marker set M_{t+1} is defined. The displacement of each vertex corresponds to the best match between the current markers m and the markers from the marker set M_{t+1}, based on three features of the markers. They are: the Euclidean distance d between the markers, the difference of curvature values, and the order along the boundary. The last is assumed to be constant. The difference in the curvature of each marker is an indication of the similarity between two markers. A curvature distance $\tilde{d}$ is defined by $\tilde{d} = |\kappa_j - \kappa_i|$, with i and j indices of markers from the frame and its successor.

Once the motion update is completed, some of the points will remain unconnected points in frame $i + 1$. These points will be removed motivated as curvature points can vanish within one step of the time resolution when the contour changes shape. At the same time, curvature points may also appear at frame $i + 1$. The segmentation is updated at frame $i + 1$ by inserting high-curvature points in frame $i + 1$ which are left out as there is no corresponding points in the previous yet still have a high predicate value H.

5.5. Results

5.5.1. Mesh Deformation Measurements on a Dynamic Blob Pattern

The first sequence demonstrates the motion of the telomere set. We have observed eleven prominent telomeres, see chapter 3. The tracks and the geometrical pattern are displayed in figure 5.5. The deformation of the triangulation is shown in figure 5.6 as a 3D image. The blue tracks are connected by red and opaque surfaces. It can be appreciated from figure 5.6 that the internal geometrical order is maintained throughout the sequence.

Figure 5.7 gives the numbers of reference to the triangles and the vertices corresponding to the positions of the eleven most prominent telomeres.

The convex hull of the group of telomeres represents the outline of the group of markers. It can be appreciated in the figures 5.6a, 5.6b, and 5.6c that the convex hull is composed from the same set of vertices (or telomeres for that matter) and in the same order throughout the sequence. In figure 5.8 the divergence and the curl are given of the convex hull.

The average divergence $\overline{d}$ of the convex hull is $\overline{d} = 2.5 \cdot 10^{-4}$, equivalent to a steadily growing area. The peak value of the divergence is $-4.5 \cdot 10^{-2}$ at frame 49. This corresponds with a shrinking of the area by 4.5%. The average curl $\overline{c}$ of the convex hull is $\overline{c} = 3.8 \cdot 10^{-2}$. This corresponds with an average rotational speed of

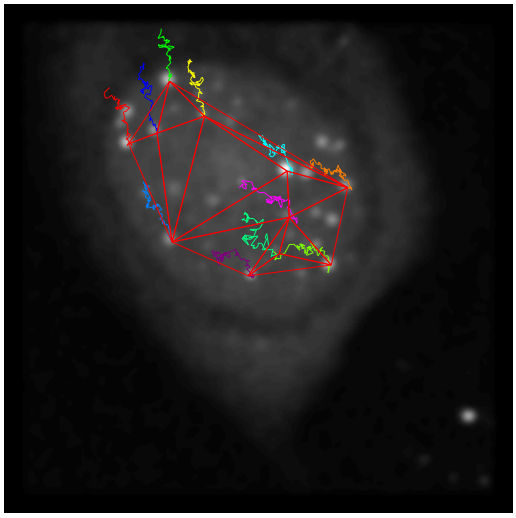

Figure 5.5.: Tracks of 11 prominent telomeres. The geometrical pattern at the start of the sequence is drawn with straight red lines.

$\omega = 1.9 \cdot 10^{-3}$, and a clockwise rotation of the convex hull of $\phi = 1.2 \cdot 10^{-1}$. The divergence and curl are fluctuating, changing between positive and negative values. This corresponds to the findings of chapter 3. The motion resembles a diffuse motion pattern combined with a steady linear displacement. To these findings one can add that the group shows a small rotation throughout the sequence.

The divergence and curl of all individual triangles is given in figure 5.9(a). All values are relatively small compared to the values of triangle 8 (see figure 5.7). The peak in divergence is a factor 100 higher than the scale of the figure. Closely examination of triangle 8 yields that the triangle becomes very small at the moment of the peak value. Under such circumstances, even a small change in area will result in a high response in divergence and curl. One may conclude that telomere 3 moves with a higher motility than the surrounding telomeres.

All other triangles show a sequence of alternating positive and negative divergence values indicating the expansion and shrinking of all individual triangles. This would suggest a random and uncoordinated motion of individual markers.

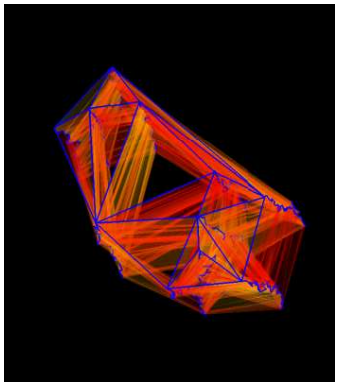

(a) top view

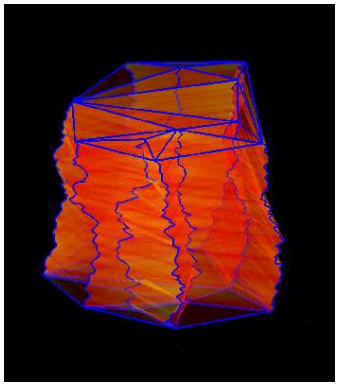

(b) side view

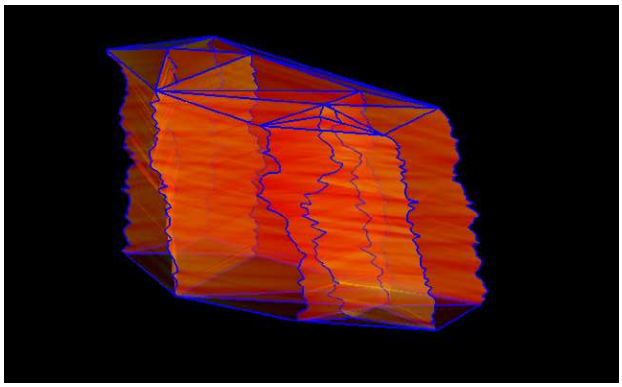

(c) front view

Figure 5.6.: 3D representation of the dynamic geometrical pattern corresponding to the pattern between the eleven most prominent telomeres.

In figure 5.10(a) the divergence of two groups of telomeres is shown. The lefties are composed of telomeres numbered 2, 8, 10 and 11. Together they span a convex hull. The rightwing group is composed of the numbers 1, 4, 5, 6 and 7. They also form a convex hull. Effectively, the two groups show a very similar pattern of movement.

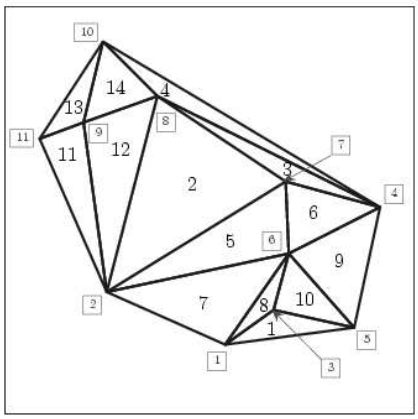

Figure 5.7.: Numbers of the triangles and the vertices corresponding to telomeres (boxed numbers).

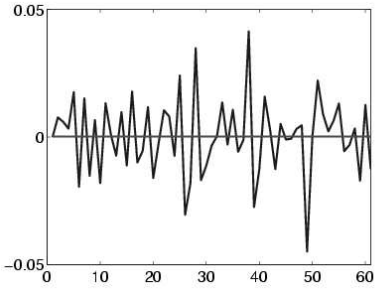

(a) Divergence of the convex hull of the group of telomeres of figure 5.5

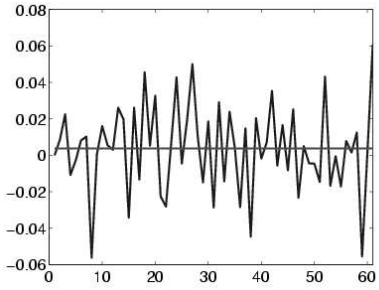

(b) Curl of the convex hull of the group of telomeres of figure 5.5

Figure 5.8.: Divergence and curl of the convex hull of the group of telomeres of figure 5.5

It might be the case that the divergence of the right group shows a slightly positive divergence near the end of the sequence possibly indicating a small expansion.

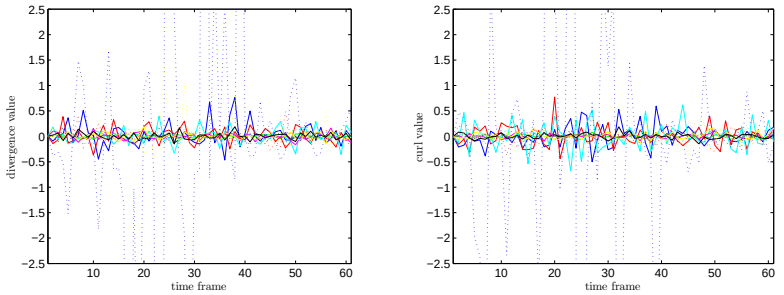

(a) Divergence of the individual triangles of figure 5.5

(b) Curl of the individual triangles of figure 5.5

Figure 5.9.: Divergence and curl of individual triangles of figure 5.5

5.5.2. Shapeless Objects

In this section we study shape deformation just after the division of a nucleus. In figures 5.11 and 5.12 the divergence of both daughter nuclei is given. The curl is given in figures 5.13 and 5.14. The survival length of high curvature points in this particular sequence is relatively short for most of them, at least short in comparison to the sampling of the sequence. Nonetheless, it is still possible to give an estimation of the divergence and curl of triangles between high curvature points. The fact that the regions are defined by markers based on curvature extrema and the order along the contour ensures that markers are connected reliably between two frames.

The sequence shows that many of the points appear and disappear. The geometrical pattern is constantly innovated and adapted to the current shape of the nucleus. Innovation and removal of high-curvature points imply that no region can be followed throughout the entire sequence.

The curl values of the one daughter at the first frame indicate a clockwise rotation in the middle a counterclockwise rotation at the right end of the object. In fact, the object expands between the two regions. This expansion and the two rotating tails indicate that the nucleus grows at that moment. More specifically the middle region moves upward.

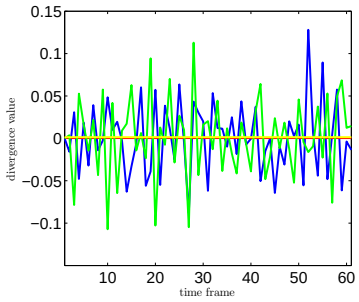

(a) Divergence of right and left triangles of figure 5.5. The blue line represents the divergence of the right group of triangles and the green line represents the divergence values of the left group. The average values of the two groups are indicated by a red line for the right group and a yellow line for the left one.

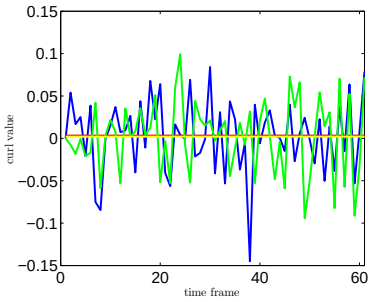

(b) Curl of right and left triangles of figure 5.5. The blue line represents the curl of the right group and the green line for the left group. Average values of the right group are indicated as before.

Figure 5.10.: Divergence and curl of groups of triangles. The two groups are the left (numbers 2, 8, 10 and 11) and the right triangles (numbers 1, 4, 5, 6 and 7)

5.6. Discussion

In this paper a method is described for estimating motion properties like divergence and curl from particles in a geometrical arrangement. They are usually small objects or even points resulting from computation as for example curvature extremes.

We have analyzed two cases. The example of the telomeres demonstrates that the method works for point sets. The estimated divergence shows that the expansion is very small $\overline{d} = 2.5 \cdot 10^{-4}$ if not negligible. The estimated curl of the telomeres set shows an average curl of $\overline{c} = 3.8 \cdot 10^{-2}$. This corresponds an overall rotation of $\phi = 1.2 \cdot 10^{-1}$.

Earlier work on the telomeres image sequence (chapter 3) showed that the individual tracks were mainly formed by random motion with just a small directional component. Based on the findings here it can be concluded in addition to the findings of chapter 3 that the telomere set is expanding. The expansion is subject to random motion throughout the nucleus where each fluctuation is much larger than any structural component.

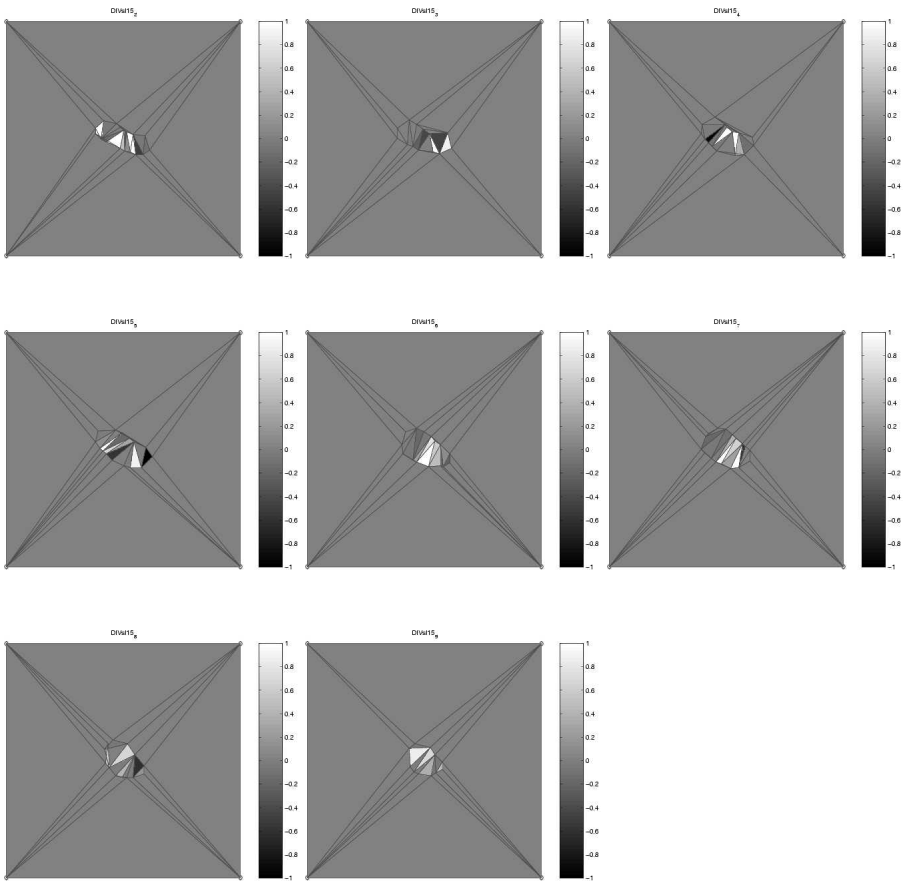

Figure 5.11.: The estimated divergence of the top daughter nucleus in slice 15 of the sequence. The top daughter nucleus, showing the divergence from frames 2 through 9. The colors of the triangles correspond to the color scale on the side of the figure.

The complete geometrical structure followed a curved motion with an estimated rotation speed of $\omega = 1.9 \cdot 10^{-3}$. The work presented here provides a useful addition to the single track estimation methods presented earlier. In this work the individual tracks

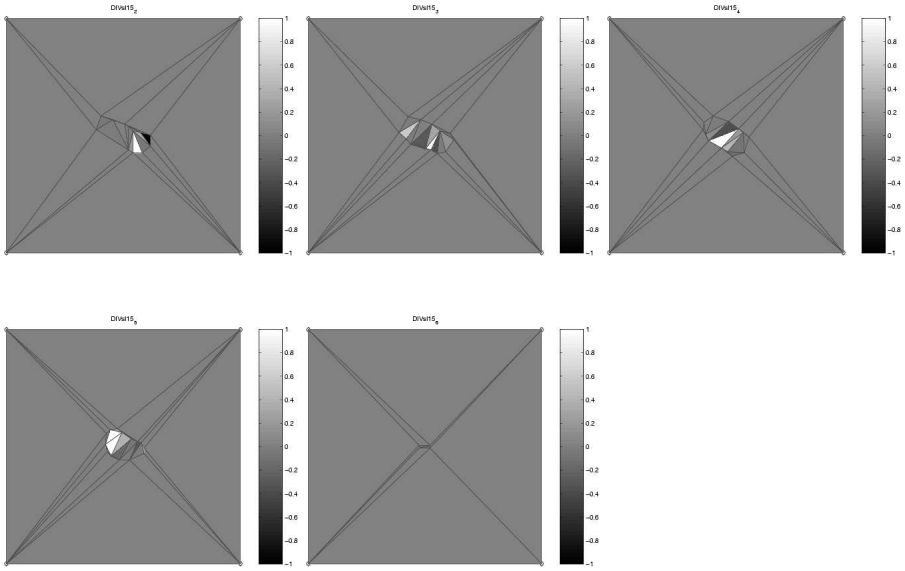

Figure 5.12.: The estimated divergence of the top daughter nucleus in slice 15 of the sequence. The lower daughter, showing the divergence from frames 2 through 6. After frame 6 the lower object disappears out of the focal plane. The colors of the triangles correspond to the color scale on the side of the figure.

are combined in a description of the dynamic geometrical arrangement.

The second part of this chapter describes a diving nucleus. The image sequence shows expanding pools of DNA during the process of mitosis inside a living cell. The expansion and rotation is captured by the estimation of the divergence and curl. The time steps are relatively long to prevent excessive damage during scanning induced by the intense laser spot used for scanning confocal microscopy. The coarseness of the time sampling poses a problem for fast processes as the splitting of a nucleus (in reality occuring between the first and the second frame, not shown). The current sequence provides insufficient information to reliably estimate shape changes. The large change in the nucleus leads to erroneous motion updates. The analysis of the two daughter nuclei shows that the length of the survival of the high-curvature points on the boundary is short, too short relative to the temporal sampling rate. This indicates large scale

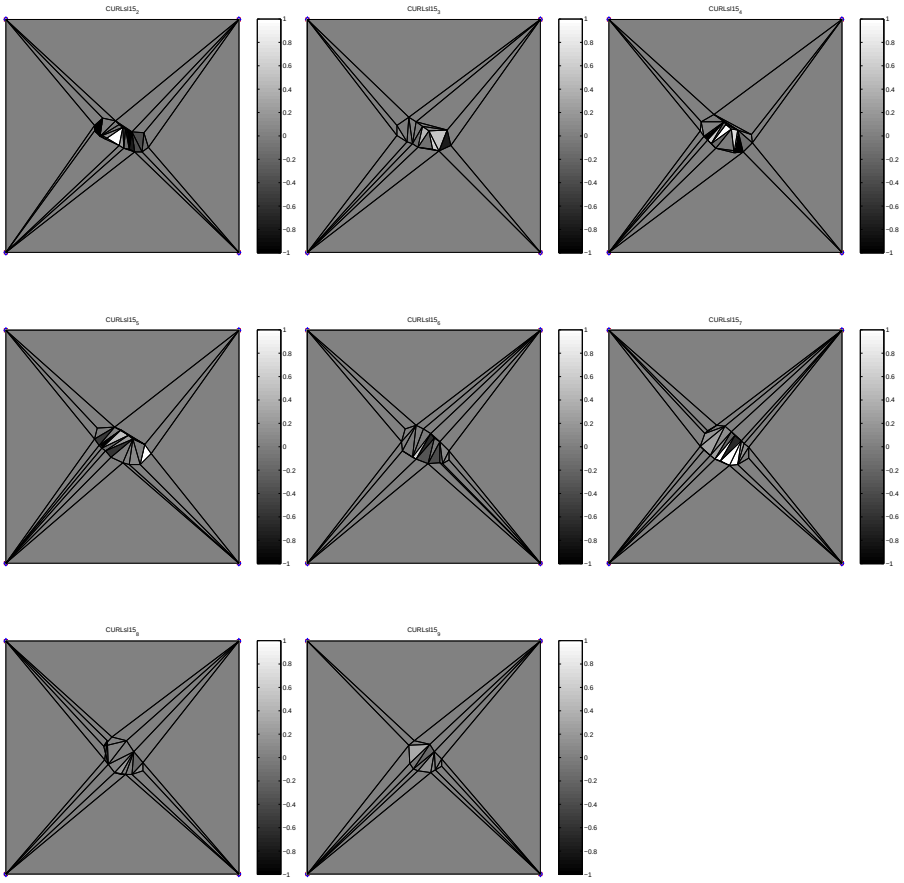

Figure 5.13.: The estimated curl of the top daughter nucleus in slice 15 of the sequence. The top daughter nucleus, showing the curl from frames 2 through 9. The colors of the triangles correspond to the color scale on the side of the figure.

internal motion in the nucleus much faster than the time between successive samples.

The presented method is successful in computing a rough estimate of motion parameters, much better than spatio-temporal methods would do. This is because the

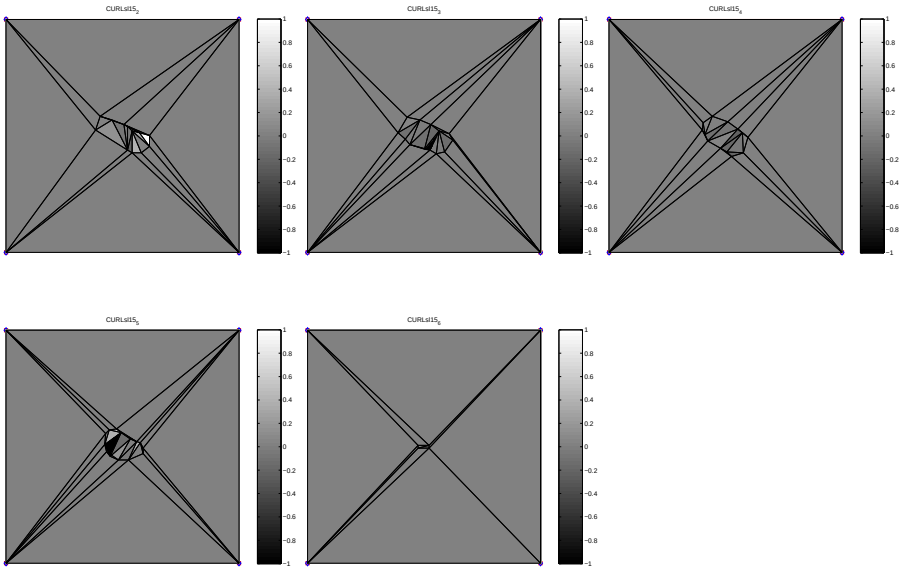

Figure 5.14.: The estimated curl of the top daughter nucleus in slice 15 of the sequence. The lower daughter, showing the curl from frames 2 through 6. After frame 6 the lower object disappears out of the focal plane. The colors of the triangles correspond to the color scale on the side of the figure.

presented method does not rely on the estimation of image derivatives in time.

6. Conclusion

With the availability of a truly three dimensional imaging device having a look at the interior of cells became possible. Imaging of living cells is demanding as it requires taking into account the dynamic processes inside living tissue, cells or cell nuclei.

Visualization of living cells is dictated by the health of the cell. As a consequence, illumination is kept as low as possible. This implies two major characteristics for the subsequent signal processing. Moderate illumination levels dictate low signal-to-noise ratios in the sequences and also low temporal sampling rates.

The low signal-to-noise ratios and the low sampling rates lead to specific methods of motion estimation. In this thesis we investigate the possibilities of several motion estimation techniques in various microscopic sequences. Under these circumstances applying a motion estimation method should always be accompanied by measures for their reliability and accuracy.

We have evaluated a velocity estimation method based on intensity derivatives in spatial and temporal domain from 3D confocal images of living cells (chapter 2). Here a reliability measure for the estimated velocity is introduced. The influence of the point-spread function on the velocity estimation can be compensated for by introducing anisotropic derivative kernels. The insight gained in the simulations is confirmed by the results of the method applied on an image sequence of a living cell with fluorescently labeled chromatin.

Sub-nuclear structures or domains represent morphological or functional entities consisting of DNA, RNA, and proteins. Analysis of the visual blobs in living cells renders information about the cellular dynamics and the cellular function. In chapter 3 we derive a computational model for tracking of spots in living cells. With this method moving spots are tracked successfully. Statistical analysis shows that the motion of the spots is a combination of diffusional, Brownian, and directed motion. Directional motion is detected in all tracks in spite of the severe Brownian component demonstrating that the method is accurate enough even for vital stain conditions.

Expansion and rotation in velocity vector fields are described by divergence and curl in chapter 4. From a dense velocity field the variance is calculated. This motion field variance is propagated through to the divergence and curl estimation, giving a reliability measure. Experiments show stochastic and systematic errors in the divergence curl values due to motion field discontinuities. Application of local divergence and curl

estimation is given using an image sequence of a crawling human T-cell.

Motion properties of groups of markers are estimated using their geometrical arrangement in chapter 5. The particles may represent single cells, small objects inside cells or boundary points of shapeless objects. With the use of Gauss' theorem and Stokes' theorem the estimation of divergence and curl is derived from a triangular graph spanned between the point set. An image sequence of 11 most prominent telomeres shows a small expansion and rotation. The second image sequence of a cell in mitosis is analyzed on high curvature points showing local uneven expansion and rotation of the nucleus.

Combining the motion estimation at a single point or a single object is only one aspect of motion estimation in living cells. Numerous parts in a cell interact. Therefore the geometrical arrangement is as important. A single track identifies the objects motility whereas the geometrical arrangement identifies the dynamical process of a group of objects. In this thesis we have analyzed both aspects of intra cellular motion to the limits of what current microscopy and estimation permit.

A. Flow fields derived from image sequences

The flow estimation and divergence and curl estimation are applied on a sequence of a flower with unfolding petals. This motion includes expansion rotation and translation of the petals see figure A.1. The motion of petals is different than the motion of the background. Therefore at the boundaries of the petals a discontinuity arises in the flow field. These boundaries will give a response for curl and divergence estimation as is expected.

Frame 11 from the image sequence demonstrates only the motion of the petals, clearly the moving parts in the frame show larger response than the background. The boundaries show large responses as expected.

Frame 23 shows positive curl in the right part of the upper petal, this is also demonstrated in the estimated curl at those positions. At the heart of the flower clear divergence is present in the flow field. This divergence is also estimated, giving rise to a bright spot in the divergence image. At the same position of large divergence less curl is estimated, demonstrating dominant divergent motion. Thus the complete flower is expanding from the heart. Note the clear response at the outer boundary of the flower. This response is due to the discontinuity in the flow field at the boundary of the flower.

Frame 40 shows also interesting flow field properties related to the growth of the petals. The petals mostly stretch, resulting in flow fields with only translational motion. The divergence estimation shows clear positive responses at the two discontinuities at the boundaries between the upper petal and the left petal and the upper petal and the right petal. Furthermore the divergence and curl at the translational flow field parts are in the order of estimations of divergence and curl of the background. Thus no significant divergence and curl are present in these parts.

In frame 46 of the sequence the flower is near its final pose, therefore motion is very small. That the motion is small can also be seen from the estimated curl and divergence, especially the lower right petal shows no significant curl nor divergence, including at positions along the boundary between the object and the background. This

implies that no discontinuity in the flow field is present. The absence of a discontinuity can have one cause, the background and the flower have the same motion. Since the background is non moving, the petal is not moving. The upper petal shows small curl, the left part of the petal expands to the left while the right part expands to the right resulting in negative and positive curl respectively.

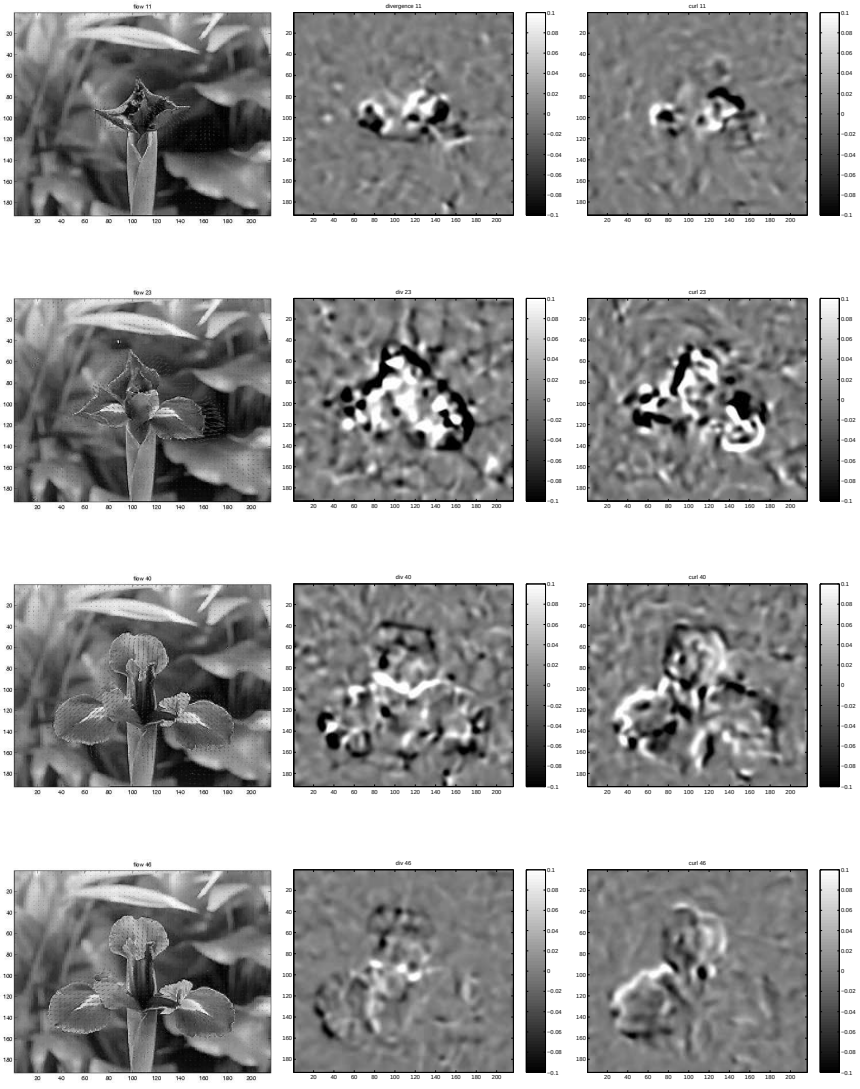

Figure A.1.: Example frames (frames 11, 23, 40 and 46) of the blooming flower image sequence, with the corresponding divergence (middle column) and curl (right column) estimations.

Bibliography

[1] Adelson, E. H., and Bergen, J. R. The extraction of spatiotemporal energy in human and machine vision. In Proceedings IEEE Workshop on Visual Motion1986 p. 151–156.

[2] Agard, D., Hiraoka, Y., Shaw, P., and Sedat, J. Fluorescence microscopy in three dimensions. Methods in cell biology 1989;30: 353–377.

[3] Aggarwal, J. K., Cai, Q., Liao, W., and Sabata, B. Nonrigid motion analysis: Articulated and elastic motion. Computer Vision and Image Understanding 1998;70:2 142–156.

[4] Allmen, M., and Dyer, C. R. Computing spatiotemporal relations for dynamic perceptual organization. Computer Vision, Graphics and Image Processing: Image Understanding 1993;85: 338–351.

[5] Alvarez, L., Weickert, J., and Sánchez, J. Reliable estimation of dense optical flow fields with large displacements. International Journal of Computer Vision 2000;39:1 41–56.

[6] Arnold, V. I. Catastrophe Theory. Springer-Verlag 1986. Translation of: Teoriia katastrof.

[7] Badenas, J., Sanchiz, J. M., and Pla, F. Motion-based segmentation and region tracking in image sequences. Pattern Recognition 2001;34:3 661–670.

[8] Bakker, P., Vliet, L. J. v., and Verbeek, P. W. Edge preserving orientation adaptive filtering. In Proceedings of the Fifth Annual Conference of the Advanced School for Computing and Imaging1999 p. 207–213.

[9] Barlow, R. J. Statistics: A guide to the Use of Statistical Methods in the Physical Sciences. John Wiley 1989.

[10] Barnard, S. T., and Thompson, W. B. Disparity analysis in images. IEEE Transactions on Pattern Analysis and Machine Intelligence 1980;2:4 333–340.

[11] Barron, J. L., Fleet, D. J., and Beauchemin, S. S. Performance of optical flow techniques. International Journal of Computer Vision 1994;12:1 43–77.

[12] Battiti, R., Amaldi, E., and Koch, C. Computing optical flow across multiple scales: an adaptive coarse-to-fine strategy. International Journal of Computer Vision 1991;6:2 133–145.

[13] Baumberg, A. M., and Hogg, D. C. An efficient method for contour tracking using active shape models. Tech. Rep. 94.11 Artificial Intelligence, University of Leeds 1994.

[14] Beauchemin, S. S., and Barron, J. L. The computation of optical flow. ACM computer surveys 1995;27:3 433–467.

[15] Bergen, J. R., Anandan, P., Hanna, K. J., and Hingorani, R. Hierarchical model-based motion estimation. In Proceedings of the European Conference on Computer Vision1992 p. 237–252.

[16] Bergsma, C. B. J., Streekstra, G. J., and Smeulders, A. W. M. Performance evaluation of motion estimation in image sequences containing gaussian objects. M. Boasson, J. A. Kaandorp, J. F. M. Tonino, and M. G. Vosselman, Eds. In ASCI'99, Proceedings of the Fifth Annual Conference of the Advanced School for Computing and Imaging1999 ASCI p. 214–220.

[17] Bergsma, C. B. J., Streekstra, G. J., and Smeulders, A. W. M. Single spot motion estimation. ISIS technical report, University of Amsterdam 2000;.

[18] Bergsma, C. B. J., Streekstra, G. J., Smeulders, A. W. M., and Manders, E. M. M. Velocity estimation of spots in 3d confocal image sequences of living cells. Cytometry 2001;43:4 261–272.

[19] Beyer, H. A. An introduction to photogrammetric camera calibration. Invited paper, seminaire Orasis, St. Malo sept. 24-27, 1991.

[20] Bimbo, A. D., and Tanganelli, P. P. L. Retrieval by content of commercials based on dynamics of color flows. In Proceedings of 15th International Conference on Pattern Recognition2000 vol. 1 p. 851–854.

[21] Black, M. J., and Anandan, P. The robust estimation of multiple motions: Parametric and piecewise-smooth flow fields. Computer Vision and Image Understanding 1996;63:1 75–104.

[22] Black, M. J., and Fleet, D. J. Probabilistic detection and tracking of motion boundaries. International Journal of Computer Vision 2000;38:3 231–245.

[23] Black, M. J., and Yacoob, Y. Recognizing facial expressions in image sequences using local parameterized models of image motion. International Journal of Computer Vision 1997;25:1 23–48.

[24] Black, M. J., Yacoob, Y., and Ju, S. X. Recognizing Human Motion Using Parameterized Models of Optical Flow vol. 9 of Computational Imaging and Vision. Kluwer Academic Publishers 1997 pp. 245–269.

[25] Bobick, A. F. Movement, activity, and action: The role of knowledge in the perception of motion. Philosophical Transactions of the Royal Society London B 1997;352: 1257–1265.

[26] Bornfleth, H., Edelmann, P., Zink, D., Cremer, T., and Cremer, C. Quantative motion analysis of subchromosomal foci in living cells using four-dimensional microscopy. Biophysical Journal 1999;77: 2871–2886.

[27] Boyer, K. L., and Kak, A. C. Structural stereopsis for 3-d vision. IEEE Transactions on Pattern Analysis and Machine Intelligence 1988;10:2 144–166.

[28] Bradshaw, D. B. Motion Estimation and Compensation of Video Sequences using Affine Transforms. PhD thesis University of Cambridge 1999.

[29] Brakenhoff, G., Blom, P., and Barends, P. Confocal scanning light microscopy with high aperture immersion lenses. Journal of Microscopy 1979;117:2 219–232.

[30] Brakenhoff, G. J., vd Voort, H. T. M., v Spronsen, E. A., and Nanninga, N. Three-dimensional imaging in fluorescence by confocal scanning microscopy. Journal of Microscopy 1989;153: 151–159.

[31] Bribiesca, E. A measure of compactness for 3d shapes. Computers & mathematics with Applications 2000;40:10 1275–1284.

[32] Brodatz, P. Textures: A Photographic Album for Artists & Designers. Dover 1966.

[33] Brown, R. G., and Hwang, P. Y. C. Introduction to Random Signals and Applied Kalman Filtering. John Wiley 1992.

[34] Canny. A computational approach te edge detection. IEEE Transactions on Pattern Analysis and Machine Intelligence 1986;8:6 679–698.

[35] Cédras, C., and Shah, M. Motion-based recognition: A survey. In IEEE Proceedings, Image and Vision Computing1995 vol. 13 p. 129–155.

[36] Celasun, I., Tekalp, A. M., Gketekin, M. H., and Harmanci, D. M. 2-d mesh-based video object segmentation and tracking with occlusion resolution. Signal Processing: Image Communication 2001;16:10 949–962.

[37] Chandebois, R. Cell sociology: a way of reconsidering the current concepts of morphogenesis. Acta Biotheor (Leiden) 1976;25: 71–102.

[38] Chang, R. Physical Chemistry with Applications to Biological Systems. MacMillan Publishing Company 1981.

[39] Chang, S. H., Cheng, F. H., Hsu, W. H., and Wu, G. Z. Fast algorithm for point pattern matching invariant to translations, rotations and scale changes. Pattern Recognition 1997;30:2 311–320.

[40] Chen, W., and Chang, S. Generating semantic visual templates for video databases. In IEEE International Conference on Multimedia and Expo2000 vol. 3 p. 1337–1340.

[41] Cipolla, R., and Blake, A. Image divergence and deformation from closed curves. International Journal of Robotics Research 1997;16:1 77–96.

[42] Cohen, I., and Herlin, I. Non uniform multiresolution method for optical flow and phase portrait models: Environmental applications. International Journal of Computer Vision 1999;33:1 29–49.

[43] Costeira, J. P., and Kanade, T. A multibody factorization method for independently moving objects. International Journal of Computer Vision 1998;29:3 159–179.

[44] Coughlan, J., Yuille, A. L., English, C., and Snow, D. Efficient optimization of a deformable template using dynamic programming. In In Proceedings the IEEE Conference on Computer Vision and Pattern Recognition1998 p. 747.

[45] Cox, I. J., and Hingorani, S. L. An efficient implementation and evaluation of reid's multiple hypothesis tracking algorithm for visual tracking. In International Conference on Pattern Recognition1994.

[46] da Vitoria Lobo, N., and Tsotsos, J. K. Computing egomotion and detecting independent motion from image motion using colinear points. Computer Vision and Image Understanding 1996;64: 21–52.

[47] Daniel, B. T., West, G. A. W., and CardewHall, M. Geometric variations: Analysis, optimization and control. Internation Journal of Pattern Recognition and Artificial Intelligence 1997;11:1 79–113.

[48] Darro, F., Kruczynski, A., Etievant, C., Martinez, J., Pasteels, J. L., and Kiss, R. Characterization of the differentiation of human colorectal cancer cell lines by means of voronoï diagrams. Cytometry 1993;14: 783–792.

[49] de Pauw, E. S., Verwoerd, N. P., Duinkerken, N., Willemze, R., Raap, A. K., Fibbe, W. E., and et al. Assessment of telomere length in hematopoietic interphase cells using in situ hybridization and digital fluorescence microscopy. Cytometry 1998;32:3 163–169.

[50] de Win, A. H. N. Quantitative analysis of organelle movements in pollen tubes. PhD thesis Katholieke Universiteit Nijmegen 1997.

[51] de Win, A. H. N., Pierson, E. S., and Derksen, J. Rational analyses of organelle trajectories in tobacco pollen tubes reveal characterics of the actomyosin cytoskeleton. Biophysical Journal 1999;76: 1648–1658.

[52] Deriche, R., and Faugeras, O. Tracking line segments. In Proceedings of the European Conference on Computer Vision1990 p. 259–268.

[53] Deriche, R., and Giraudon, G. A computational approach for corner and vertex detection. International Journal of Computer Vision 1993;10:2 101–124.

[54] Dev, A. Image sequences in the horus project. a conversation. Tech. rep. University of Amsterdam 1998.

[55] Dev, A. Visual Navigation on Optical Flow. PhD thesis University of Amsterdam 1998.

[56] Dev, A., Kröse, B. J. A., and Groen, F. C. A. Confidence measures for image motion estimation. Tech. Rep. 96001 Real World Computing 1997.

[57] Duann, J. R., Chiang, S. H., Lin, S. B., Lin, C. C., Chen, J. H., and Su, J. L. Assessment of left ventricular cardiac shape by the use of volumetric curvature analysis from 3d echocardiography. Computerized Medical Imaging and Graphics 1999;23:2 89–101.

[58] Duann, J. R., Lin, S. B., Hu, W. C., and Su, J. L. Computer system for four-dimensional transesophageal echocardiographic image reconstruction. Computerized Medical Imaging and Graphics 1999;23:4 173–179.

[59] Duncan, J., and Ayache, N. Medical image analysis: Progress over two decades and the challenges ahead. IEEE Transactions on Pattern Analysis and Machine Intelligence 2000;22:1 85–106.

[60] Essa, I., and Pentland, A. Facial Expression Recognition Using Image Motion vol. 9 of Computational Imaging and Vision. Kluwer Academic Publishers 1997 pp. 271–298.

[61] Faugeras, O. Three-Dimensional Computer Vision, A Geometric Viewpoint. The MIT Press 1993.

[62] Felzenszwalb, P. Representation and detection of deformable shapes. In In Proceedings the IEEE Conference on Computer Vision and Pattern Recognition2003 vol. 1 p. 102.

[63] Fennema, C., and Thompson, W. Velocity determination in scenes with several moving objects. Computer Graphics and Image Processing 1979;9: 301–315.

[64] Fitzpatrick, J. M. The existence of geometrical density-image transformations corresponding to object motion. Computer Vision, Graphics and Image Processing: Image Understanding 1988;44: 155–174.

[65] Fleet, D. J., Black, M. J., Yacoob, Y., and Jepson, A. D. Design and use of linear models for image motion analysis. International Journal of Computer Vision 2000;36:3 171–193.

[66] Fleet, D. J., and Jepson, A. D. Computation of component image velocity from local phase information. International Journal of Computer Vision 1990;5:1 77–104.

[67] Florack, L., Niessen, W., and Nielsen, M. The intrinsic structure of optic flow incorporating measurement duality. International Journal of Computer Vision 1998;27:3 263–286.

[68] Ford, R. M. Critical point detection in fluid flow images using dynamical system properties. Pattern Recognition 1997;30:12 1991–2001.

[69] Fox, R. W., and McDonald, A. T. Introduction to Fluid Dynamics. John Wiley & Sons 1985.

[70] Freeman, W. T., and Adelson, E. H. The design and use of steerable filters. IEEE Transactions on Pattern Analysis and Machine Intelligence 1991;13:9 891–906.

[71] Gavrila, D. The visual analysis of human movement: A survey. Computer Vision and Image Understanding 1999;73:1 82–98.

[72] Geusebroek, J. M., Smeulders, A. W. M., Cornelissen, F., and Geerts, H. Segmentation of tissue architecture by distance graph matching. Cytometry 1999;35: 11–22.

[73] Geusebroek, J. M., Smeulders, A. W. M., and van de Weijer, J. Fast anisotropic gauss filtering. In 7th European Conference on Computer Vision2002 Lecture Notes in Computer Science p. 99.

[74] Gevers, T., and Smeulders, A. Combining region splitting and edge detection through guided delaunay image subdivision. In Proceedings of IEEE Computer Vision and Pattern Recognition 19971997 p. 1021–1026.

[75] Gomes, J., and Faugeras, O. Shape representation as the intersection of $n - k$ hypersurfaces. Tech. rep. Institut National de Recherche en Informatique et en Automatique 2000.

[76] Ha, J. E., and Kweon, I. S. Robust direct motion estimation considering discontinuity. Pattern Recognition Letters 2000;21:11 999–1011.

[77] Hagedoorn, M., and Veltkamp, R. A general method for partial point set matching. In Proceeding of the Thirteenth Annual Symposium on Computational Geometry1997 ACM p. 405–408.

[78] Hoffman, R. The multiple uses of fluorescent proteins to visualize cancer in vivo. Nature Reviews Cancer 2005;5:10 796–806.

[79] Horn, B. K. P., and Schunk, B. G. Determining optical flow. Artificial Intelligence 1981;17: 185–204.

[80] Hummel, R., and Sundareswaran, V. Motion parameter estimation from global flow field data. IEEE Transactions on Pattern Analysis and Machine Intelligence 1993;15: 459–475.

[81] j Shi, and Tomasi, C. Good features to track. In 1994 IEEE Conference on Computer Vision and Pattern Recognition (CVPR94)1994 p. 593–600.

[82] Jarosch, R. Die impulsrichtungsänderungen bei der induktion der protoplasma strömung. Protoplasma 1956;67: 478–486.

[83] Johansson, G. Visual perception of biological motion and a model for its analysis. Perception and Psychphysics 1973;14:2 201–211.

[84] Joliffe, I. T. Principal component analysis. New York: Springer-Verlag 1986.

[85] Jonas, A., and Kiryati, N. Digital representation schemes for 3d curves. Pattern Recognition 1997;30:11 1803–1816.

[86] Jones, G. A. Reviewing correspondence processes for motion. Tech. Rep. KUCSES-96-03 School of Computer Science & Electronic Systems, Kingston University 1996.

[87] Kanatani, K. Detecting the motion of a planar surface by line and surface integrals. Computer Vision, Graphics and Image Processing 1985;29: 13–22.

[88] Kanda, T., Sullivan, K., and Wahl, G. Histone-gfp fusion protein enables sensitive analysis of chromosome dynamics in living mammalian cells. Current Biology 1998;8: 377–385.

[89] Kappers, A. M. L., te Pas, S. F., Koenderink, J. J., and van Doorn, A. J. Simulating the detection of first-order optical flow components. Vision Research 1996;36: 3539–3547.

[90] Kelemen, A., Szekely, G., Reist, H. W., and Gerig, G. Automatic segmentation of cell nuclei from confocal laser scanning microscopy images. Lecture Notes in Computer Science 1996;1131: 193–202.

[91] Knoll, C., Alcaniz, M., Grau, V., Monserrat, C., and Juan, M. C. Outlining of the prostate using snakes with shape restrictions based on the wavelet transform (doctoral thesis: Dissertation). Pattern Recognition 1998;32:10 1767–1781.

[92] Koenderink, J. J. Optic flow. Vision Research 1986;26: 161–180.

[93] Koenderink, J. J. Solid Shape. The MIT press 1990.

[94] Kreyszig, E. Advanced Engineering Mathematics. John Wiley & Sons 1988.

[95] Lansdorp, P. M., Verwoerd, N. P., van de Rijke, F. M., Dragowska, V., Little, M. T., Dirks, R. W., and et al. Heterogeneity in telomere length of human chromosomes. Hum Mol Genet 1996;5:5 685–691.

[96] Larsen, R. Estimation of Visual Motion in Image Sequences. PhD thesis Technical University of Denmark 1994.

[97] Lindeberg, T. Scale-space theory in computer vision. Kluwer Academic Publishers 1993.

[98] Longuet-Higgins, H. C., and Prazdny, K. The interpretation of a moving retinal image. Proceedings of the royal society of london, series B 1980;208: 385–397.

[99] Lorenz, C., and Krahnstover, N. Generation of point-based 3d statistical shape models for anatomical objects. Computer Vision and Image Understanding 2000;77:2 175–191.

[100] Lucas, B. D., and Kanade, T. An iterative image registration technique with an application to stereo vision. In Proceedings of Imaging Understanding Workshop1981 p. 121–130.

[101] M B van Leeuwen, and Groen, F. C. A. Requirements for motion estimation in image sequences for traffic applications. Tech. Rep. CS-99-01 University of Amsterdam 1999.

[102] Malladi, R., Sethian, J. A., and Vemuri, B. C. Shape modeling with front propagation: A level set approach. IEEE Transactions on Pattern Analysis and Machine Intelligence 1995;17:2 158–175.

[103] Manders, E., Visser, A., Koppen, A., de Leeuw, W., van Liere, R., Brakenhoff, G., and van Driel, R. Four-dimensional imaging of chromatin dynamics during the assembly of the interphase nucleus. Chromosome Research 2003;11: 537–547.

[104] Manders, E. M. M., and et. al. manuscript in preparation 2000;.

[105] Manders, E. M. M., Kimura, H., and Cook, P. R. Direct imaging of DNA in living cells reveals the dynamics of chromosome formation. Journal of Cell Biol 1999;144:5 813–821.

[106] Manders, E. M. M., Stap, J., Strackee, J., van Driel, R., and Aten, J. A. Dynamic behavior of dna replication domains. Experimental Cell Research 1996;226: 328–335.

[107] Manuelidis, L. Individual interphase chromosome domains revealed by in situ hybridization. Hum. Gent 1985;71: 288–293.

[108] Maurizot, M., Bouthemy, P., Delyon, B., Iouditski, A., and Odobez, J. Locating singular points and characterizing deformable flow fields in an image sequence. Tech. rep. Institut de Recherche en Informatique et Systèmes Aléatoires 1994.

[109] Maybeck, and S., P. Stochastic models, estimation, and control vol. 141 of Mathematics in Science and Engineering. Academic Press 1979.

[110] McInerney, T., and Kikinis, R. An object-based volumetric deformable atlas for the improved localization of neuroanatomy in mr images. Medical Image Computing and Computer-assisted Intevention - MICCAI'98 1998;1496: 861–869.

[111] McInerney, T., and Terzopoulos, D. A finite element model for 3d shape reconstruction and nonrigid motion tracking. In ICCV'931993 p. 518–523.

[112] McNeil, P. L., and Warder, E. Glass beads load macromolecules into living cells. J Cell Sci 1987;88:Pt 5 669–678.

[113] Minsky, M. Memoir on inventing the confocal scanning microscope. Scanning 1988;10: 128–138.

[114] Misteli, T. Protein dynamics: Implications for nuclear architecture and gene expression. Science 2001;291: 843–847.

[115] Misteli, T., Cáceres, J. F., and Spector, D. L. The dynamics of a pre-mrna splicing factor in living cells. Nature 1997;387: 523–527.

[116] Mitiche, A., Wang, Y. F., and Aggarwal, J. K. Experiments in computing optical flow with the gradient based, multiconstraint method. Pattern Recognition 1987;20:2 173–179.

[117] Nguyen, H. T., Worring, M., and van den Boomgaard, R. Occlusion robust adaptive template tracking. In Proceedings of the IEEE International Conference on Computer Vision, ICCV'012001 p. 678.

[118] Niessen, W. Multiscale medical image analysis. PhD thesis University Utrecht 1997.

[119] Noordmans, H. J. Interactive analysis of 3D microscope images. PhD thesis University of Amsterdam 1997.

[120] Noordmans, H. J., and Smeulders, A. W. M. Detection and characterization of isolated and overlapping spots. Computer Vision and Image Understanding 1998;70:1 23–35.

[121] Noordmans, H. J., van der Kraan, K., van Driel, R., and Smeulders, A. W. M. Randomness of spatial distributions of two proteins in the cell nucleus involved in mrna synthesis and their relationship. Cytometry 1998;33:3 297–309.

[122] Oomes, S., Snoeren, P., and Dijkstra, T. 3d shape representation: Transforming polygons into voxels. Scale-space Theory in Computer Vision; Lecture Notes in Computer Science 1997;1252: 349–352.

[123] Palmari, J., Dussert, C., Berthois, Y., Penel, C., and Martin, P. M. Distribution of estrogen receptor heterogeneity in growing mcf-7 cells measured by quantitative microscopy. Cytometry 1997;27: 26–35.

[124] Papadopoulo, T., and Faugeras, O. Applications of motion field of curves. In Applications of invariance in Computer Vision1993 no. 825 in Lecture Notes in Computer Science.

[125] Paragois, N., and Faugeras, O. Geodesic active regions for motion estimation and tracking. Tech. rep. Institut National de Recherche en Informatique et en Automatique 1999.

[126] Park, S. K., and Kweon, I. S. Robust and direct estimation of 3-d motion and scene depth from stereo image sequences. Pattern Recognition 2001;34:9 1713–1728.

[127] Patterson, G., Knobel, S., Sharif, W., Kain, S., and Piston, D. Use of the green fluorescent protein and its mutants in quantitative fluorescence microscopy. Biophys. J. 1997;73:5 2782–2790.

[128] P.K. Hepler, B. G. Confocal fluorescence microscopy of plant cells. Protoplasma 1998;201:3-4 121–157.

[129] Pla, F., and Marchant, J. A. Matching feature points in image sequences through a region-based method. Computer Vision and Image Understanding 1997;66:3 271–285.

[130] Platani, M., Goldberg, I., Swedlow, J. R., and Lamond, A. I. In vivo analysis of cajal body movement, separation, and joining in live human cells. The Journal of Cell Biology 2000;151:7 1561–1574.

[131] Polana, R., and Nelson, R. Temporal Texture and Activity Recognition vol. 9 of Computational Imaging and Vision. Kluwer Academic Publishers 1997 pp. 86–124.

[132] Polthier, K., and Preuß, E. Variational approach to vector field decomposition. In Scientific Visualization2000 Proceedings of Eurographics Workshop on Scientific Visualization Springer Verlag p. 518–523.

[133] POV-team. www.povray.org.

[134] Press, W. H., Teukolsky, S. A., Vetterling, W. T., and Flannery, B. P. Numerical Recipes in C. Cambridge University Press 1992.

[135] Qian, H. Single-particle tracking: Brownian dynamics of viscoelastic materials. Biophysical Journal 2000;79: 137–143.

[136] Qian, H., and Elson, E. L. Quantitative study of polymer conformation and dynamics by single-particle tracking. Biophysical Journal 1999;76: 1598–1605.

[137] Ramussen, C., and Hager, G. D. Joint probabilistic techniques for tracking multi-part objects. In IEEE Computer Society Conference on Computer Vision and Pattern Recognition1998 p. 16–21.

[138] Rao, A. R., and Jain, R. C. Computerized flow field analysis: Oriented texture fields. IEEE Transactions on Pattern Analysis and Machine Intelligence 1992;14:7 693–709.

[139] Rasmussen, C., and Hager, G. D. Probabilistic data association methods for tracking multiple and compound visual objects. Transactions on PAMI (Submitted October 12, 1999) 1999; xx–xx.

[140] Ratanasopa, S., Bolson, E. L., Sheehan, F. H., McDonald, J. A., and Bashein, G. Performance of a fourier-based program for three-dimensional reconstruction of the mitral annulus on application to sparse, noisy data. INTERNATIONAL JOURNAL OF CARDIAC IMAGING 1999;15:4 301–307.

[141] Rieder, C., and Khodjakov, A. Mitosis through the microscope: Advances in seeing inside live dividing cells. Science 2003;300:5616 91–96.

[142] Rittscher, J., Kato, J., Jago, S., and Blake, A. A probabilistic background model for tracking. In *6th European Conference on Computer Vision (ECCV 2000)* vol. 1843 p. 336 – 350.

[143] Sato, Y., Moriyama, M., Hanayama, M., Naito, H., and Tamura, S. Acquiring 3d models of non-rigid moving objects from time and viewpoint varying image sequences: A step toward left ventricle recovery. IEEE Transactions on Pattern Analysis and Machine Intelligence 1997;19:3 253–259.

[144] Saxton, M. J., and Jacobson, K. Single-particle tracking: Applications to membrane dynamics. Annual Reviews Biophysics and Biomolecular Structure 1997;26: 373–399.

[145] Schnabel, J. A., and Arridge, S. R. Active shape focusing. IMAGE AND VISION COMPUTING 1999;17:5 419–428.

[146] Sclaroff, S., and Isidoro, J. Active blobs. In Proceedings of the International Conference on Computer Vision1998.

[147] Seitz, S. M., and Dyer, C. R. View-invariant analysis of cyclic motion. International Journal of Computer Vision 1997;25: 1–23.

[148] Sethi, I. K., and Jain, R. Finding trajectories of feature points in a monocular image sequence. IEEE Transactions on Pattern Analysis and Machine Intelligence 1987;9:1 56–73.

[149] Shah, M., and Jain, R. Motion Based recognition vol. 9 of Computational Imaging and Vision. Kluwer Academic Publishers 1997.

[150] Shah, M., Rangarajan, K., and Tsai, P. Motion trajectories. IEEE Transaction on Systems, Man and Cybernetics 1993;23:4 1138–1150.

[151] Sheppard, C., and Choudhury, A. Image formation in the scanning microscope. Optica Acta 1977;24:10 1051–1073.

[152] Silva, C., and Santos-Victor, J. Egomotion estimation on a topological space. In 14th International Conference on Pattern Recognition ICPR'981998.

[153] Simoncelli, E. P., Adelson, E. H., and Heeger, D. J. Probability distribution of optical flow. In Proceedings of the Conference on Computer Vision and Pattern Recognition1991 p. 310–315.

[154] Soll, D. R. Computer-assisted three-dimensional reconstruction and motion analysis of living, crawling cells. COMPUTERIZED MEDICAL IMAGING AND GRAPHICS 1999;23:1 3–14.

[155] Spinéi, A., and Pellerin, D. Motion estimation of opaque or transparent objects using triads of gabor filters. Signal Processing 2001;81:4 845–853.

[156] Steger, C. An unbiased detector of curvilinear structures. IEEE Transactions on Pattern Analysis and Machine Intelligence 1998;20:2 113–125.

[157] Stephens DJ, A. V. Light microscopy techniques for live cell imaging. Science 2003;300:5616 82–86.

[158] Steven, G. P., Li, Q., and Xie, Y. M. Evolutionary topology and shape design for general physical field problems. Computational Mechanics 2000;26:2 129–139.

[159] Steven, G. P., Querin, O., and Xie, Y. M. Evolutionary structural optimisation (eso) for combined topology and size optimisation of discrete structures. COMPUTER METHODS IN APPLIED MECHANICS AND ENGINEERING 2000;188:4 743–754.

[160] Stokman, H. M. G., Gevers, T., and Koenderink, J. J. Color measurement by imaging spectrometry. Computer Vision and Image Understanding 2000;79: 236–249.

[161] Strasters, K. C. Quantitative analysis in confocal image cytometry. PhD thesis Technical University Delft 1994.

[162] Streekstra, G. J., Smeulders, A. W. M., and van den Boomgaard, R. Tracing of curvilinear structures in 3d images with single scale diameter measurement. In Proceedings of the International Conference on Scale-Space Theories in Computer Vision, Lecture Notes in Computer Science vol. 1682, Corfu1999 p. 500–506.

[163] Streekstra, G. J., van den Boomgaard, R., and Smeulders, A. W. M. Scale dependent differential geometry for the measurement of center line and diameter in 3d curvilinear structures. In Proceedings of the European Conference on Computer Vision2000 p. 856–870.

[164] Suri, J. S. Computer vision, pattern recognition and image processing in left ventricle segmentation: The last 50 years. PATTERN ANALYSIS AND APPLICATIONS 2000;3:3 209–242.

[165] Szelisky, R., and Kang, S. B. Shape ambiguities in structure from motion. Tech. Rep. CRL 96/1 Cambridge research laboratory 1996.

[166] Taylor, J. R. An introduction to Error Analysis: The study of Uncertainties in Physical Measurements. University Science Books 1989.

[167] te Pas, S. F., Kappers, A. M. L., and Koenderink, J. J. Detection of first-order structure in optic flow fields. Vision Research 1996;36:2 259–270.

[168] ter Haar Romeny, B., and Florack, L. M. Front end vision: A multiscale geometry engine - scale-space theory in computer vision versus front-end biological vision.

[169] ter Haar Romeny, B. M., Florack, L. M. J., Koenderink, J. J., and Viergever, M. A. Invariant third order properties of isophotes: T-junction detection. In Proceedings of 7th SCIA1991 p. 346–353.

[170] Tommasiniand, T., Fusielloand, A., Truccoand, E., and Roberto, V. Making good features track better. In IEEE Computer Society Conference on Computer Vision and Pattern Recognition1998 p. 178–183.

[171] Trask, B. J., Allen, S., Massa, H., Fertitta, A., Sachs, R., and van den Enghand M Wu, G. Studies of metaphase and interphase chromosomes using fluorescence in situ hybridization. Cold Spring Harb. Symp. Quant. Biol. 1993;58: 767–775.

[172] Tsien, R. Y. The green fluorescent protein. Annu. Rev. Biochem. 1998;67: 509–544.

[173] Ullman, S. The interpretation of Visual Motion. The MIT press 1979.

[174] van der Plas, G. A. J., and Bastiaans, R. J. M. Accuracy and resolution of a fast ptv-algorithm suitable for hires-pv. In 8th International Symposium on Flow Visualisation1998.

[175] van der Voort, H. T. M., Noordmans, H. J., Messerli, J. M., and Smeulders, A. W. M. Physically realistic volume visualization for interactive analysis. In Proceedings Eurographics1993 p. 295–306.

[176] van Kempen, G. M. P. Image restoration in fluorescence microscopy. PhD thesis Delft University 2000.

[177] van Leeuwen, M., and Groen, F. Motion interpretation for in-car vision systems. In Proceedings of the International Conference on Intelligent Robots and Systems2002 Omnipress p. 135–141.

[178] van Vliet, L. J. Grey-scale measurements in multi-dimensional digitized images. PhD thesis Delft University 1993.

[179] Vedula, S., Baker, S., Seitz, S., and Kanade, T. Shape and motion carving in 6d. In Computer Vision and Pattern Recognition (CVPR)June 2000.

[180] Veenman, C. J., Reinders, M. J. T., and Hendriks, E. A. A fast and robust point tracking algorithm. In Proceedings of the fifth annual conference of the Advanced School for Computing and Imaging1999 p. 457–461.

[181] Verestóy, J. Digital piv: a challenge for feature based tracking. In Proc. 23^{rd} Workshop of the Austrian Pattern Recognition Group1999.

[182] Vincent, L. Graphs and mathematical morphology. Signal Processing 1989;16: 365–388.

[183] Vliet, L. J., and Verbeek, P. W. Curvature and bending energy in digitized 2d and 3d images. In Proceedings of the 8th Scandinavian Conference on Image Analysis1993.

[184] Wang, Y., and Lee, O. Active mesh - A Feature Seeking and Tracking Image Sequence Representation Scheme. IEEE Transaction on Image Processing 1994;3:5 610–624.

[185] Weber, J., and Malik, J. Robust computation of optical flow in a multi-scale differential framework. International Journal of Computer Vision 1995;14: 67–81.

[186] Wolf, P. R. Elements of Photogrammetry. McGraw-Hill book company 1986.

[187] Worring, M. Shape Analysis of Digital Curves. PhD thesis University of Amsterdam 1993.

[188] Worring, M., and Smeulders, A. W. M. Digital curvature estimation. Computer Vision, Graphics and Image Processing: Image Understanding 1993;58:3 366–382.

[189] Yacoob, Y., and Davis, L. S. Estimating Image Motion Using Temporal Multi-Scale Models of Flow and Acceleration vol. 9 of Computational Imaging and Vision. Kluwer Academic Publishers 1997 pp. 17–37.

[190] Younsi, R., KnopfLenoir, C., and Selman, A. Multi-mesh and adaptivity in 3d shape optimization. COMPUTERS & STRUCTURES 1996;61:6 1125–1133.

[191] Zerroug, M., and Nevatia, R. Part-based 3d descriptions of complex objects from a single image. IEEE Transactions on Pattern Analysis and Machine Intelligence 1999;21:9 835–848.

[192] Zhang, D., and Lu, G. Segmentation of moving objects in image sequence: A review. Circuits, Systems and Signal Processing 2001;20:2 143–183.

[193] Zhang, J., and Huang, T. S. Extracting 3d vortices in turbulent fluid flow. IEEE Transactions on Pattern Analysis and Machine Intelligence 1998;20:2 193–199.

[194] Zheng, Q., and Chellappa, R. Automatic feature point extraction and tracking in image sequences for arbitrary camera motion. International Journal of Computer Vision 1995;15: 31–76.

Samenvatting

Dit proefschift behandelt bewegingschatting en classificatie in multidimensionale microscopie beelden. Schatting van beweging en meting van richting en snelheid wordt bepaald door middel van optical flow in drie dimensionale beeldreeksen van chromatine in de kern van een levende cel. Hierbij wordt de spreiding van de geschatte verplaatsingsvectoren benut om een schatting te maken van de nauwkeurigheid van de bewegingsschatting. Voor objecten met afmetingen vergelijkbaar met de afbeeldingslimiet van een confocale microscoop is de vorm niet uniek. Een tracking methode gebasseerd op een Kalman tracking methode gebruikt bekende eigenschappen van dergelijke objecten voor het vormen van de afgelegde weg. Telomeren in een levende cel zijn succesvol met deze methode te volgen.

Een geschatte beweging is met een bekende nauwkeurigheid te bepalen. De gemaakt fout in de bewegingsschatting werkt door in hiervan afgeleide grootheden. Deze doorrekening van meetfouten is beschreven, experimenten zijn ter verduidelijking uitgevoerd.

De vervorming en geometrische relatie tussen objecten in een celkern is meer dan alleen de opgetelde informatie van de enkele objecten op zich. De ontwikkelde methode is succesvol toegepast op microscopie beeldreeksen met ver-schillende ty-pen beelden. De verkregen bewegingsinformatie kan toegepast worden in onderzoek naar de structuur en dynamiek in levende cellen.

[1] summary in dutch

Dankwoord

Allereerst gaat mijn dank uit naar mijn promotor Arnold Smeulders, die ondanks de soms ietwat schokkerige voortgang toch een eindresultaat voor ogen heeft gehad. Arnold, het geduld dat je met mij hebt kunnen uitoefenen ben ik je zeer dankbaar voor.

Een tweede persoon die ik zeker wil bedanken is Willem Lenglet, met name in de staart van mijn promotie onderzoek heb jij een belangrijke rol gespeeld. Bij onze eerste kennismaking was er al sprake van een mogelijke afronding van dit manuscript. Echter de uitermate positieve, maar tegelijk ook zeer duidelijke en scherpe houding van jou heeft die laatste hobbel uiteindelijk neembaar gemaakt, daarvoor ben ik je zeer dankbaar.

Erik Manders, wat is een proefschift zonder data? Erik je hebt een enorme schat aan data in je ”schoenendoos”liggen. Mede dankzij jouw kennis en kunde met betrekking tot het levend houden van cellen in toch wel een vijandige omgeving is het mogelijk om beweging in deze cellen te bestuderen. Ik ben je zeer dankbaar voor de vrijwillige inzet die je hebt getoond voor het opdiepen en opnemen van meerdere data reeksen die in dit manuscript zijn gebruikt. Het bekijken van deze beeldreeksen maakt iedere keer weer indruk op mij.

Geert Streekstra, jij hebt het promotie onderzoek op gang gebracht. Jouw inbreng in de eerste fase wordt zeer gewaardeerd en heeft uiteindelijk het geheel mogelijk gemaakt.

Ook naaste collega’s en vrienden hebben een belangrijke bijdrage aan dit manuscript geleverd. Zij het niet direct inhoudelijk dan is het wel door de sfeer die onontkoombaar door jullie gevormd wordt. Zonder iemand te kort te willen doen wil ik twee in het bijzonder bedanken. Rien en Roland. We hebben onze tijd in Amsterdam in dezelfde ruimte doorgebracht. Dit was met jullie zeker geen straf. Ook naast het onderzoek hebben we Amsterdam van tijd tot tijd onveilig weten te maken. Dit zouden we wat mij betreft nog eens een keer moeten doen.

Afra bedankt voor het mooie ontwerp van de omslag.

Mijn schoonouders (en ja Grietje, daar hoor jij ook bij) bedankt voor de onvoorwaardleijke steun. En ma, ik heb te vroeg je ”duwen op de rolschaatsen”moeten missen.

Papa en mama, jullie onuitputtelijke interesse en betrokkenheid is geweldig. Ik zal het nog wel eens proberen om in andere termen een en ander uit te leggen.

Dankwoord

Sigrid, jij hebt nog het meeste last van mijn ambities en de grillen die daarbij horen. Ik heb enorme bewondering hoe jij Joris, Niels en mij in het gareel probeert te houden. Ik beloof je dat je vanaf morgen geen last meer hebt van mijn voortslepende ”promotie-verstrooidheid”.